Ionic Charge States of Solar Energetic Particles

Thesis by

Luke Sollitt

In Partial Fulfillment of the Requirements

for the Degree of

Doctor of Philosophy

California Institute of Technology

Pasadena, California

2004

(Defended September 2, 2003)

Claudit iter bellis, qui portam pandit in astris.

—Alcuin

Acknowledgements

I am a physics dropout. Yes, it's true. I started out as a physics major at the University of Maryland, and I could not handle it. I ended up getting a degree in German in the middle of a recession, and took a job with the IRS. In the spring of 1995, I was 23 years old, and I thought my life was basically over. I was in a job I hated, and I thought myself a failure, having failed at being what I most wanted to be in life: a physicist. It was around this time that my aunt, Pat Crane, entered the Cordon Bleu Academy for chefs at the age of sixty. I was inspired. If she could start a new career at age sixty, then I could certainly start again as well. With great encouragement from my mother, I made the fateful decision to go back to the University of Maryland and finish my physics degree.

Going back to Maryland was tough. I had not studied physics in over five and a half years by the time I started in the fall of 1995. One great bit of help I got along the way was a suggestion by Professor Joe Redish, a teacher of mine my first time through, to read the Feynman lectures. Even so, I found myself buried in special functions, wave equations, and so much unfamiliar math that I could not even breathe. If not for the study group that formed in those early days, I am not sure where my experiment in physics learning would have gone. Adeena Mignogna, Aaron Marks, Linda Harden, Mike Asbury, Aisha Miller, Steve Moeller, and others were all part of that wonderful group. Many were the nights when we would gather in big room next to the SEDS office in the Astronomy

building, spending hour upon hour on physics problems, first in quantum mechanics, then eventually in thermodynamics. I still remember basic quantum mechanics better than any other physics thanks to that group.

But Maryland was not all problem sets. There was other work to be done, such as in lab courses, and with lab work. My first semester back, I discovered the joys of studying cosmic rays in the advanced undergraduate lab course. It was while modifying the cosmic ray experiment in the advanced undergraduate lab course that I met Professor Jordan Goodman. I ended up spending the summer of 1996 working for Dr. Goodman in Los Alamos, New Mexico, on the Milagro detector. Later on, I spent a couple of weeks in January 1997 working for him on the Super-Kamiokande neutrino detector in Japan. It was these experiences that prompted me to go into space physics.

Getting into Caltech was for me, as I am sure it is for many people, a childhood dream come true. I had wanted to come to this quirky place in Pasadena since I was perhaps nine years old. I was not the only person from Maryland to come to Caltech that year. Kevin Scaldeferri and Aaron Eichelberger also came at the same time. I knew both of them particularly well, having shared several courses with Kevin, and having shared my experiences in New Mexico and Japan with Aaron, and a course besides. In fact, Aaron and I drove from Maryland to New Mexico and back again in my rickety old Land Rover – a journey I am sure lives clearly in both our memories even these years later.

There is no course at Caltech for the branch of physics I study. Instead, I learned the old-fashioned way: through informal discussion. Here at Space Radiation Laboratory, my teachers have been the various past and present group members and visitors through the years: Dick Mewaldt, who guided me through the candidacy process, Alan Cummings with his quick wit and Texas sensibility, Rick Leske who always astonishes me with his mastery of the data and can do crystallography from one million miles away, Christina Cohen who (along with Rick) is one of our Level 2 data gurus, Mark Wiedenbeck, Jeff George, Allan Labrador, Penny Slocum, Mike Thayer, Sven Geier, Jim Higdon and Nasser Barghouty. The folks at SRL are a great group of people to work with. They throw a good party, too. Particular thanks go to Rick and Christina for reading this thesis and pointing out the errors.

They say misery loves company. So do graduate students. A number of different office mates over the years have kept me company, offered guidance, and generally been there for me: Sarah Yost, Ryan Ogliore, Paul Price, Daniel Williams, Ah San Wong, and Aaron Eichelberger, who thought by that time that he'd never be rid of me. Particular thanks go to Aaron for keeping me just distracted enough with things like Carmageddon, EQ and Monday Night Raw to keep me sane.

In the end game of graduate school, the great problem is the writing of the thesis. A thesis is a large document, and putting it together can be somewhat daunting. Approaching the end of my time at graduate school, I found help and counsel from a great group that met for lunch every week. We would discuss our theses, or interviews, or talks, and set goals for the following week. We were all from the same year: Samantha Edgington, Shanti Rao, and Mike Hartl. Particular thanks go to Mike for teaching me how to find the zero of a Coulomb Wave Function, and to Sam who was a reader for this thesis.

Research scientists, office mates and thesis groups are only part of the large tapestry of people who have been part of my life here at Caltech. Others have had their impact on me and on the writing of this thesis. I met Rick Jenet just as he was finishing his thesis. We have had many misadventures involving mountains and stuck cars, among other things, and will continue to do so for quite some time to come. Wally Berg is a mountain guide.

He was my guide on a hike to the Base Camp of Mt. Everest, at an altitude of 17,500 feet. I'll never forget the beauty of the Himalayas in the morning, or the long walks on the sometimes precipitous trail, dodging yaks along the way. My mother, Karen Rak, has been a great source of strength for me in the years since deciding to go back and try physics again. Without her steadfast encouragement and support, I might not ever have made it this far.

It is no mistake that my name is Luke, and I study space physics. I was five years old when the very first Star Wars movie came out in the theaters. From then on, all I have really wanted was to lead a life devoted to space. I knew I wanted to be a physicist before I was even able to say the word. But just as my more famous namesake had Yoda to be his mentor and guide, so too have I had mine. Professor Edward C. Stone has been my Yoda, principally since his retirement from being Director of the Jet Propulsion Laboratory. Apart from being one of the most formidable science thinkers I have ever met, Dr. Stone has a gift for science management. He has been there to set me on the path, and to gently set me back on it when I have been led astray.

Abstract

A novel technique to infer average ionic charge states of high energy ($\geq$ 10 MeV/nuc) solar energetic particles (SEPs) in large solar events is presented. In some large SEP events, it is observed that higher energy SEPs decay in intensity more rapidly than at lower energies. Furthermore, this energy dependence varies with particle species, as would be expected if the decay timescale depended on a rigidity-dependent diffusive mean free path. Observations are done with the Solar Isotope Spectrometer (SIS) on board the Advanced Composition Explorer spacecraft. By comparing the decay timescales of nitrogen, oxygen, neon, magnesium, silicon, sulfur, and iron to a reference element, such as carbon, charge states are inferred for these elements in three SEP events between 1997 and 2002. In a fourth event, upper limits of charge states are inferred. For the solar event of November 6, 1997, charge states are also inferred for sodium, calcium, and nickel. These charge states are compared with other measurements at similar energies, and with measurements at lower energies.

Two interpretations of the data are discussed. First, if there is no stripping in the shock acceleration process, the charge states inferred for the events might be indicative of source plasma temperatures (Arnaud & Rothenflug, 1985; Arnaud & Raymond, 1992). It is found that two of the events examined have temperatures consistent with the acceleration of particles from the corona. The other two events have best fit temperatures that might indicate a mixture of sources, including the corona and a hot flare region. Second, iron charge states from this work and from other work (Mazur *et al.*, 1999; Möbius *et al.*, 1999; Cohen *et al.*, 1999) at various energies for the November 6, 1997, event are compared to the models of Barghouty & Mewaldt (2000) and Kovaltsov *et al.* (2001) for shock acceleration in a dense plasma, which include the effects of stripping and recombination due to interactions with protons and electrons. These models can describe the observed charge state spectra with acceleration from the corona without invoking mixture with a hot source.

Contents

List of Figures

List of Tables

Chapter 1

Introduction

In the early seventeenth century, a very famous natural philosoper by the name of Galileo Galilei challenged ideas about the Sun that had been considered true for almost two thousand years. Prior to his work, it was thought that the Sun was a smooth, perfect sphere of light, forever immutable, placid, quiet. This was part of the view first promulgated by Aristotle, and embraced by the Catholic Church, that the heavens were perfect and unchanging. Galileo was among the first people to observe sunspots. Figure 1.1 shows one of his drawings of the Sun, done on June 18, 1612. This drawing was done by projecting the light of the Sun through a telescope against a wall in his lab. The sketch was done on the image on the wall. Even today, Earth-bound solar observatories function in much the same manner, only with more sophisticated ways to collect the image. In the figure, one can see several black spots that Galileo has labeled. Other early researchers thought these might be intramercurial planets. In a series of letters to Marc Welser, a wealthy patron of science, Galileo showed that they were, in fact, blemishes on the Sun. He did not know what they were; he thought they might be clouds in the Solar atmosphere. Galileo became the first person to challenge the notion of the perfect immutability of the heavens and show that the Sun was a dynamic body. He later suffered censure and excommunication by the Church and lifelong house arrest for his work.

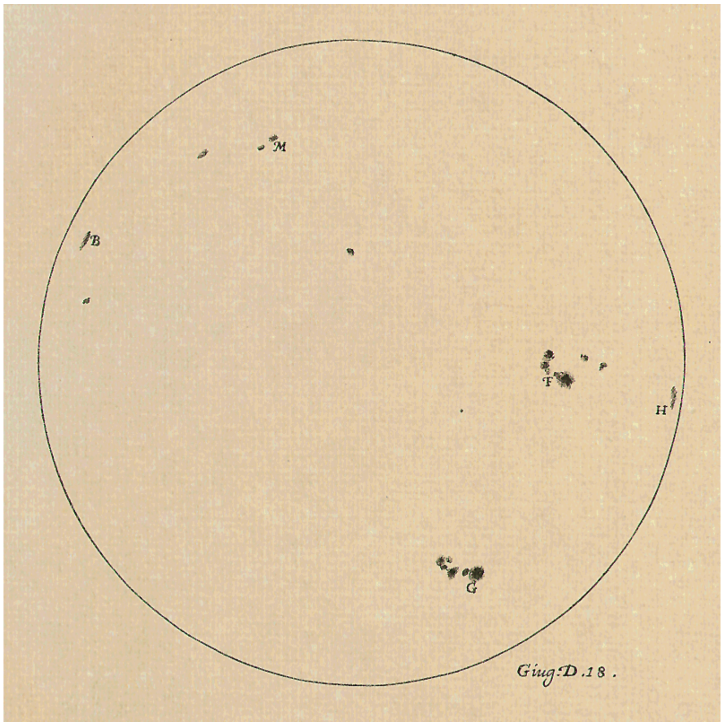

Figure 1.1: Early work on sunspots. This drawing by Galileo Galilei was done on June 18, 1612. Galileo was the first to show that the black spots observed over the solar disk were in fact on the Sun. From the Rice University Galileo project website.

Almost four hundred years of subsequent work has documented that the Sun is indeed a very dynamic body. Figure 1.2 shows observations of the Sun somewhat more recent than Galileo's. This photo was taken by the Extreme ultraviolet Imaging Telescope (EIT) on board the Solar and Heliospheric Observatory (SOHO) spacecraft at 304 Å (which would be the He II line). This figure is from the SOHO/EIT website; SOHO is a spacecraft dedicated to solar observations. One can see that the Sun is a dynamic place indeed. Far from being a smooth, perfect sphere of light, the Sun appears to have a mottled appearance from the granules and supergranules that make up its surface. Along with these, one can see many bright hot spots, as well as darker, cooler regions. On the western limb (the right side of the sun), a large loop of matter called a prominence can be seen. On the southern edge of the Sun, another bit of material called a filament can be seen leaving the surface.

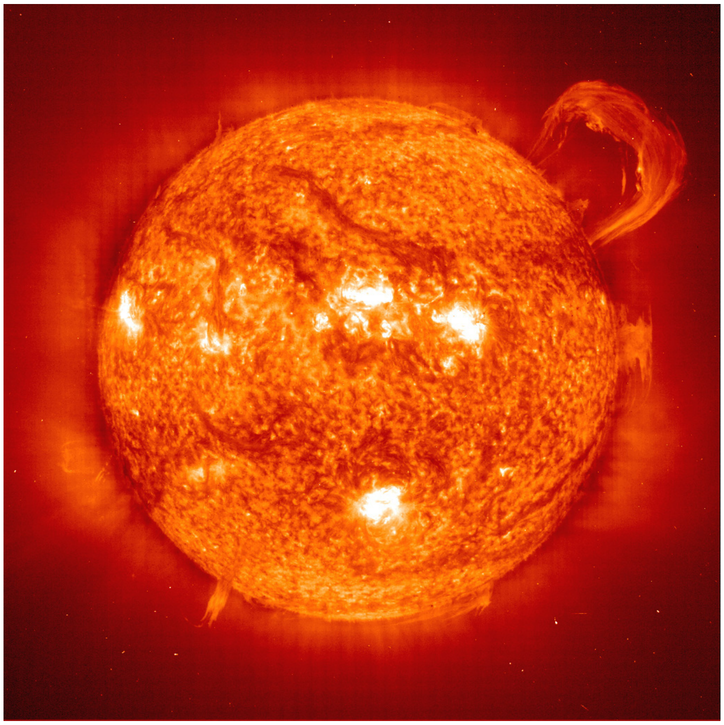

Figure 1.2: A normal day on the Sun. Note the large prominence on the western limb, and the filament on the southern edge. Photo from the EIT camera on board SOHO; from the SOHO/EIT webpage.

Work on the dynamic Sun has expanded greatly since Galileo's time. Different branches of astrophysics and space science examine different problems associated with the Sun. Solar astrophysicists seek to understand its radio and X-ray emissions. Helioseimologists try to understand bulk movements on and under the surface. Space physicists study the tenuous wind that boils off of the surface, and the energetic particles that are sometimes accelerated and ejected at or close to the Sun.

The objective of all of what is to follow is to explore in some small way one of the many ways in which the Sun is dynamic.

1.1 Solar energetic particles: The whys and wherefores

One of the ways in which the Sun shows its dynamic nature is in solar energetic particle events. Solar energetic particles, or SEPs (and the reader is well advised to get used to this acronym now), are ionized atoms that are accelerated at or close to the Sun to energies that might be found in a high energy cyclotron – from 10 up to about 100 MeV for each nucleon in the atom. In the notation commonly in use in space physics, this is 10-100 MeV/nuc (MeV/nucleon).

Even before the first spacecraft ever flew, SEPs were observed in solar events when particles from the Sun generated neutrons in the upper atmosphere. These neutrons created transient increases in counting rates in neutron monitors on the Earth's surface (see, for instance, Meyer, Parker & Simpson, 1956). In general, SEPs only occur in transient events, and are not part of the Sun's steady-state particle emission. Two of the open questions in space physics are where SEPs come from and how they are accelerated. A review of particle acceleration at the Sun and in the heliosphere can be found in Reames (1999). A brief discussion of some of what is presented there will be given here.

Solar particle events are roughly divided into two categories: gradual and impulsive. Impulsive events are typically very short (hours long), low in intensity, and have a small spatial extent. That is, the particle flux is constrained to remain in a narrow tube that extends from the Sun past the Earth. By contrast, gradual events last several days, have very high intensities (up to two or three orders of magnitude greater than in impulsive events) and can be seen across a much wider range of locations in the heliosphere (that is, the particles are no longer constrained to move on a narrow tube as in impulsive events). This phenomenology has led to different theories about where these kinds of events originate relative to the Sun, and how the particles in these events are accelerated.

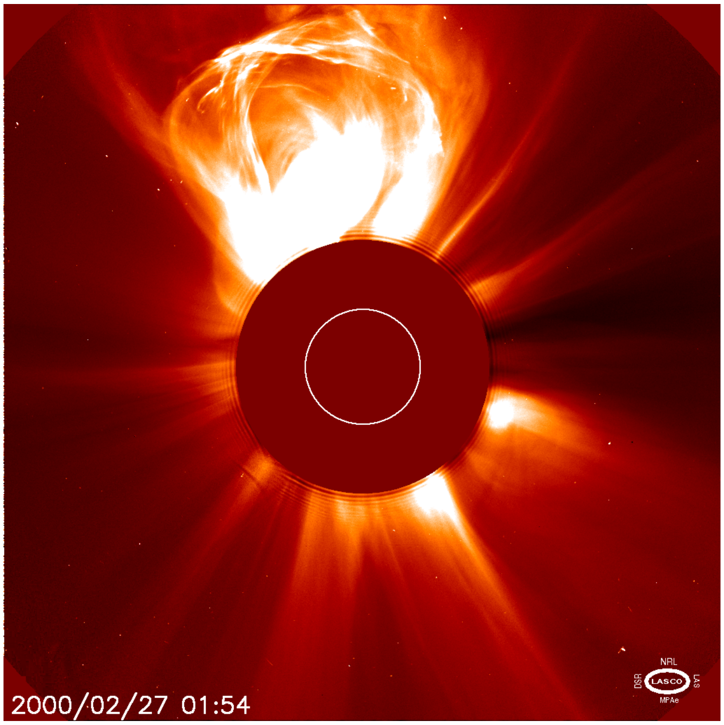

Figure 1.3: A coronal mass ejection (CME). This is what happens when a prominence has enough energy to escape the surface of the Sun. A CME like this one will drive a magnetohydrodynamic shock that will accelerate particles in the ambient corona. Photo taken by the SOHO coronagraph (LASCO); from the SOHO webpage.

Figure 1.3 shows a photo of a coronal mass ejection, or CME, taken by the Large Angle and Spectrometric Coronagraph (LASCO) on board the SOHO spacecraft. A coronagraph works by blocking out the light directly from the Sun, and instead only examining the light from the corona. In this image, the white circle is where the disk of the Sun would be if the light were not blocked. As can be seen in the figure, a CME is basically a large solar prominence that has enough energy to lift off the surface of the Sun. In this case, the CME extends five solar radii away from the Sun. Sometimes, a CME will expand at a speed higher than the solar wind speed. Such a CME will drive a magnetohydrodynamic shock. This shock might accelerate particles in the ambient corona, causing a gradual solar particle event. Since the acceleration mechanism will operate at many heliolongitudes, the event will have a large spatial extent. In gradual events, then, the particles are expected to be accelerated out of the corona.

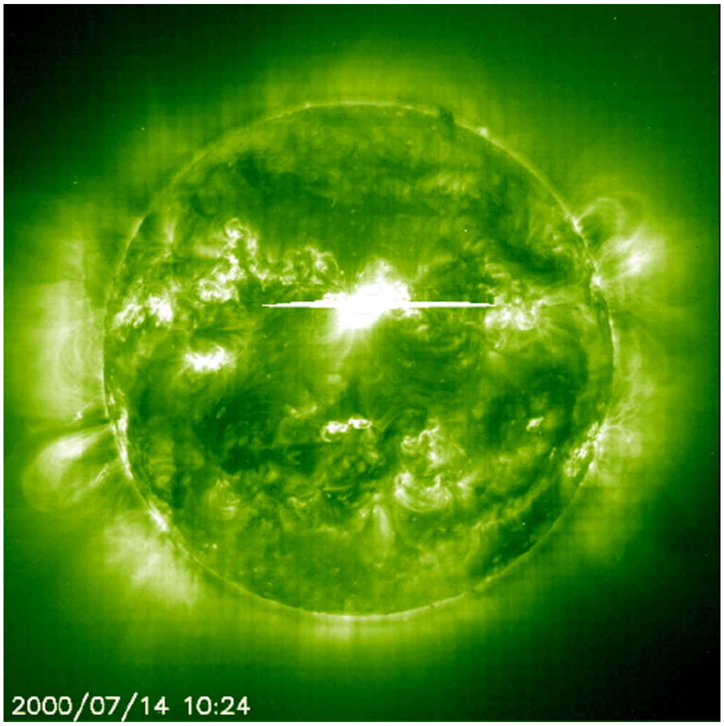

Figure 1.4: The hot flare event of July 14, 2000 (the so-called Bastille Day event). Photo taken by EIT on board SOHO. This X20 X-ray flare was so powerful that it saturated the CCD in EIT (horizontal white bar in the photo). Flare sites are likely source locations for SEPs in impulsive events. The temperature in such a region can reach higher than 10 million kelvins. From the SOHO/EIT web page.

Figure 1.4 is a photo taken by the SOHO/EIT instrument at 171 Å (the emission line for iron that has had eleven electrons stripped) of a very intense X-ray flare that occurred on July 14, 2000. This event came to be known as the Bastille Day event. The horizontal bar in the photo happened because the CCD in EIT was saturated by the flare. Flare sites such as this one are thought to be the source locations for SEPs in impulsive events. Acceleration is thought to occur at the flare site, where the plasma temperature can reach over 10 million kelvins.

One of the large differences between the proposed acceleration sites in gradual and particle events is the source plasma temperature. In a hot flare region, this temperature is expected to be ~10 million kelvins, or MK. In the corona, the temperature is expected to be ~ 1-2 MK. One possible way to determine the source location for SEPs, then, would be to measure their temperature. But where is one to find a thermometer that can measure an extremely rarefied plasma in interplanetary space at temperatures in the millions of kelvins?

1.2 SEP charge states: a solar thermometer?

One possible thermometer might be in the ionic charge states of the SEPs themselves. One of the possible ways to interpret SEP charge states is as being representative of the plasma from which they were accelerated. When a shock accelerates particles out of a source plasma, the assumption is that the particles in the plasma are in thermodynamic equilibrium at the temperature characteristic for the source location.

At the temperatures one expects in the corona or a hot flare region, the energy in the random collisions is high enough to strip electrons from atoms, producing a plasma. As the temperature rises, more electrons are stripped. Arnaud & Rothenflug (1985) evaluated ionization and recombination rates for elements that are astrophysically abundant, including all of the most abundant elements in SEPs. They also calculate the average charge state of the ions of a certain atomic species in a plasma as a function of energy.

The results of the Arnaud & Rothenflug (1985) calculations for oxygen can be seen in Figure 1.5. This figure shows the average charge state of oxygen ions in a plasma as a function of the plasma temperature. This is plotted over a large range of temperatures: from 10,000 kelvins to ten million kelvins. The charge state rises with temperature, as one might expect (higher temperature means higher center of mass energy in collisions in

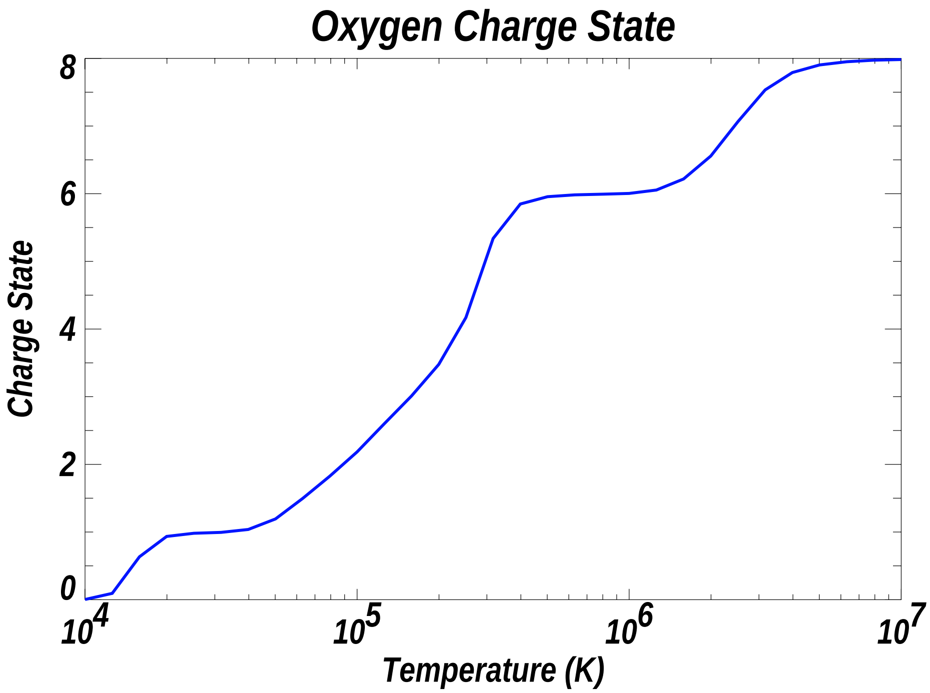

Figure 1.5: Average oxygen charge state as a function of plasma temperature. Calculation from Arnaud & Rothenflug (1985).

the plasma). However, there are three distinct plateaus in the charge state. Two of these plateaus are at temperatures that might be of astrophysical interest. At ∼0.3-1 MK, oxygen has become helium-like,and has an average charge state of about six. Above about 2 MK, the average charge state has again begun to rise. The ultimate plateau where all of the oxygen has become fully stripped is above 6 MK. So in a coronal sample of material (as one should find in a gradual event), one would expect an average charge state of perhaps 6.5. In an impulsive sample, one might expect to see fully stripped oxygen.

Figure 1.6 shows the charge state of iron ions in a plasma as a function of temperature. This plot is taken from the calculations of Arnaud & Raymond (1992), who specifically examined iron ionization and recombination rates, and calculated average charge states. Unlike oxygen in Figure 1.5, there are no plateaus in the charge state below 10 MK. At

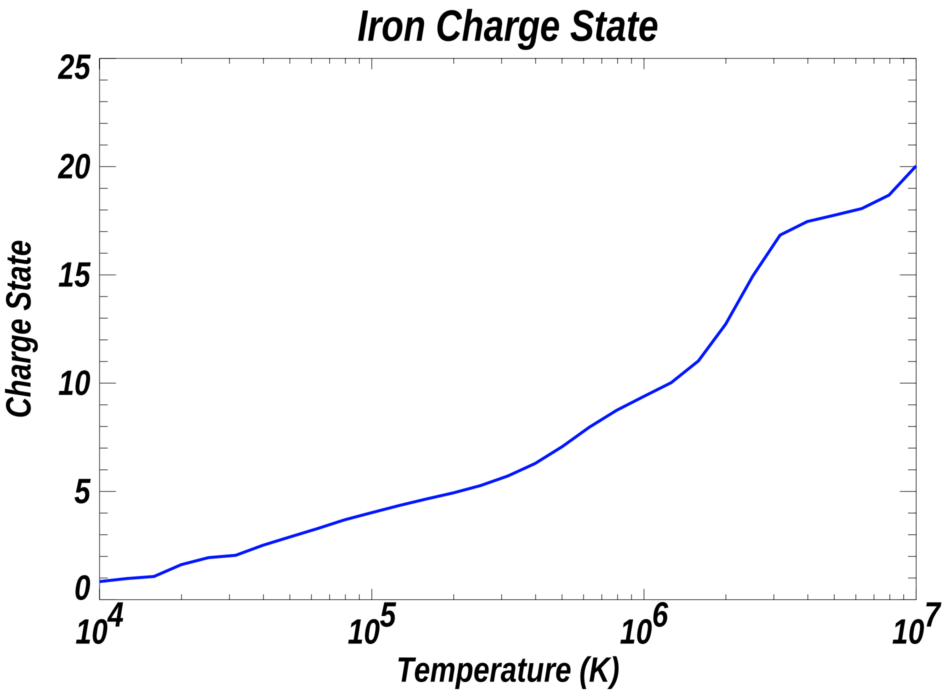

Figure 1.6: Average iron charge as a function of plasma temperature. Calculation from Arnaud & Raymond (1992).

~3-7 MK, the charge state climbs more slowly than at other temperatures, but it never becomes flat with temperature. At coronal temperatures, one might expect a charge state of roughly 10. At 10 MK, the charge state reaches 20.

1.3 Acceleration effects

If the assumption is true that SEP charge states represent the temperature of the source plasma, then charge states can be used to determine where these particles are coming from in an event. However, there might be nonthermal processes that occur during acceleration that might render the observed charge state different from its thermal value. A signature of such a process might be a charge state that changes with the particle energy.

Models for acceleration in a dense plasma including charge-changing processes have been worked out by many authors, including Ostryakov & Stovpyuk (1999), Barghouty & Mewaldt (2000) and Kovaltsov *et al.* (2001). Processes that might affect a particle's charge state during acceleration include ionization and recombination due to collisions with electrons and other ions in the source plasma. Given a long enough period of time, or a dense enough plasma, a particle population at a given energy will assume an equilibrium average charge state, just as particles in an accelerator beam do when they are passed through a foil. Typical acceleration times are of the order of ∼1-10 sec, in plasma densities of $\sim 10^8$-10^9 particles per cm^3. Generally, high-Z particles such as silicon and iron are not in a dense enough plasma for a long enough period of time for the population average charge state to reach its equilibrium value. Lower-Z particles such as oxygen might become fully stripped in the acceleration process.

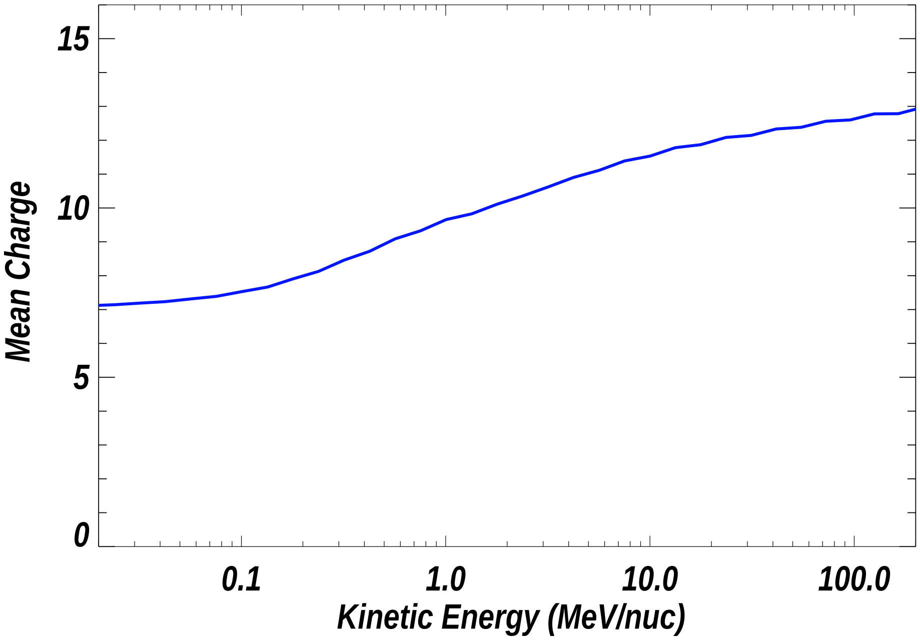

Figure 1.7: Average silicon charge as a function of particle energy (in MeV/nuc) in a solar particle event. Calculation from Barghouty & Mewaldt (2000).

Figure 1.7 shows the average charge state of silicon as a function of energy (in MeV/nuc) as modelled by Barghouty & Mewaldt (2000) for a solar particle event that happened on November 6, 1997. At low energies (e.g., ∼0.1 MeV/nuc) the charge state is about seven, which would be consistent with a source plasma temperature of about 1 MK. The charge state rises montonically, and the rate of rise decreases above ∼10 MeV/nuc. At these high energies, the particles have been in the shock region long enough to approach the charge state equlibration. In the Barghouty & Mewaldt (2000) work, the shape of the charge state spectrum will depend on the product of the acceleration time τ_{acc} and the square root of the electron density $\sqrt{n_e}$. Based on X-ray intensities in this event, an acceleration time to 30 MeV/nuc of ∼10 sec was assumed. From this acceleration time, the electron density assumed in this calculation was 2×10^9particles per cm^3.

Ostryakov & Stovpyuk (1999) found that for coronal temperatures (e.g., ∼1 MK, for which the charge state of iron is ∼9 according to Arnaud & Raymond (1992)), an electron density of $5 \times 10^8 \mathrm{cm}^-3$ could produce a charge state for iron from ∼14 to ∼16 at about 100 MeV/nuc; an electron density of $5 \times 10^9 \mathrm{cm}^-3$ could produce a charge state for iron from ∼21 to ∼24 at the same energy. In both cases, the time spent accelerating the particles is at most a few seconds. At lower energies, they expected the charge state to reflect the thermal value.

Kovaltsov *et al.* (2001) extended the work of Ostryakov & Stovpyuk (1999) and Barghouty & Mewaldt (2000). These authors examined the charge equilibration of iron during acceleration in a hot plasma. They included effects due to interactions with protons as well as electrons, and examined effects due to the nature of the acceleration mechanism. They assumed that the rate of energy gain for a particle being accelerated would be a power law in the particle's energy:

$$\left(\frac{dE}{dt}\right)_a = \frac{E_1}{\tau_1}\left(\frac{E}{E_1}\right)^S$$

where $E_1 = 1\text{MeV/nuc}$ and τ_1 is the characteristic time for an ion to be accelerated to 1 MeV/nuc. Figure 1.8, from Kovaltsov *et al.* (2001), shows the product of $n \times \tau_1$ as a function of the iron charge state at 30 MeV/nuc. Here, n is the plasma density. For this plot, $S = 0$ is assumed: that is, the rate of energy gain is constant. Different values of S would give different curves. One can see that if the value of S can be found, and the charge state at an appropriate energy known, it would be possible to find the product $n \times \tau_1$ for a solar particle event.

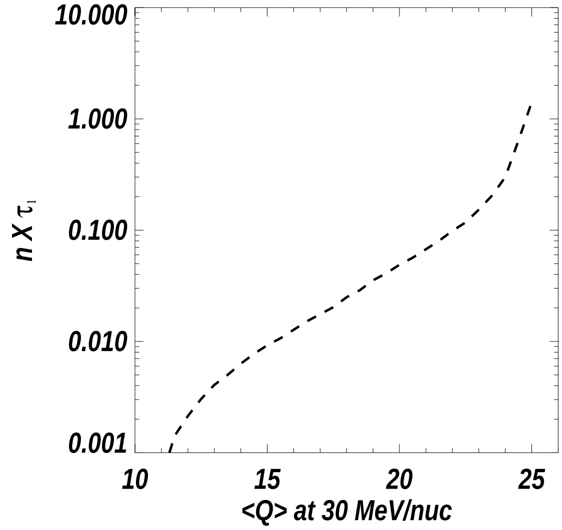

Figure 1.8: The product of electron density and time of acceleration to 1 MeV/nuc as a function of the average charge state of iron at 30 MeV/nuc. Calculation from Kovaltsov *et al.* (2001). A measure of the charge state of iron at ~ 30 MeV/nuc would provide a measure of the product of the electron density and the acceleration time.

Figure 1.9, also from Kovaltsov *et al.* (2001), shows a set of calculations by those authors of the charge of iron at various energies for various values of $n \times \tau_1$ and S. It can be seen

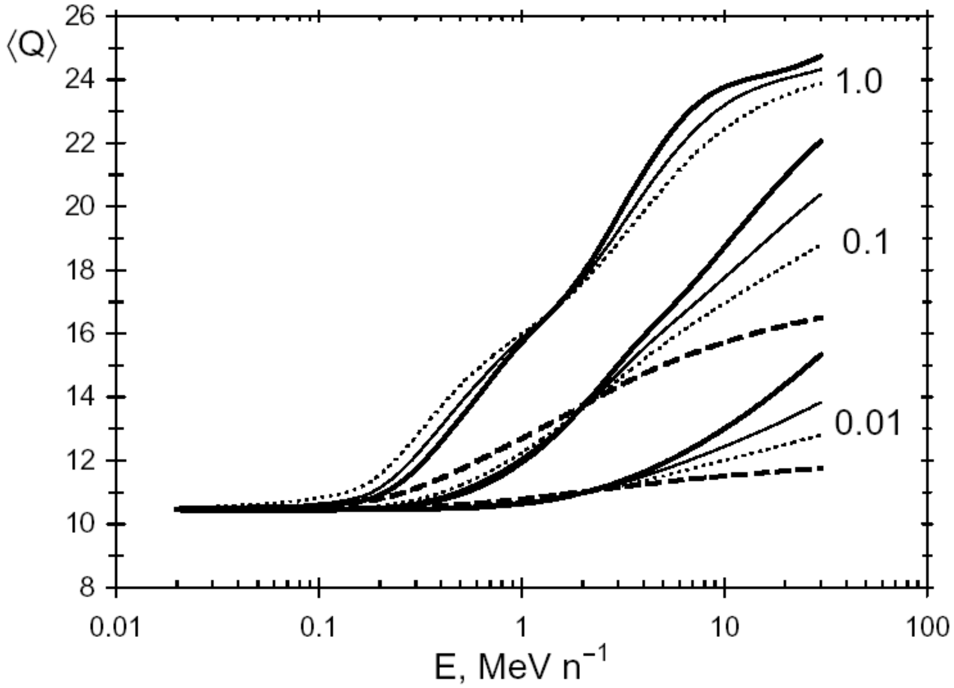

Figure 1.9: The mean charge state of iron as a function of several energy, from Kovaltsov *et al.* (2001). The several curves in the plot all correspond to different parameters being used the calculation. Each family of curves corresponds to a different fixed value for the product of the acceleration time and the electron density: either 0.01, 0.1, or 1.0 $\times 10^{10}$ cm^{-3}sec. Within each family of curves, each curve represents a different value of S: heavy solid curves are $S = 0$, light solid curves are $S = 0.25$, dotted curves are $S = 0.5$, and dashed curves are $S = 1.0$. Examining energy dependence in a single event might provide insight into the acceleration process by fixing which of these curves is correct for the event.

that there is a wide variety of charge state energy spectra that can be predicted by this model for various values of $n \times \tau_1$ and S. Measurements of the iron charge state at high and low energies in a single event might be able to specify which of these curves is the correct one for the event, and in so doing, provide some information as to the conditions in the source plasma and the nature of the acceleration mechanism.

More generally, if one examines the charge states at high energies, and compares to other measurements at low energies in a particular solar event, it may be possible to differentiate between the two different interpretations of the charge states. That is, it may be possible to determine whether the charge states observed are indicative of the source plasma temperature or show that stripping occurs in particle acceleration in large gradual events. In the current work, charge states will be inferred at high energies ($\sim 10-100$ MeV/nuc), and compared to lower energy measurements where available.

Chapter 2

From Decay Times to Charge States: A Curious Character's Journey through the Lands of Models and Theory

2.1 The basics

In the analysis of Solar Energetic Particle (SEP) data from the Solar Isotope Spectrometer (SIS) on board the Advanced Composition Explorer (ACE) spacecraft, it is observed in several solar particle events that the rate at which the SEPs flow out of the inner heliosphere depends on particle energy and species. This is not a newly discovered phenomenon: similar energy dependencies were seen by Lupton (1973), Lupton & Stone (1973), and many others over the years (see, for example, Lee, 2000). It is possible that this energy and species dependence, really a velocity and rigidity dependence, could be used as a tool to study properties of solar energetic particles (SEPs) and the interplanetary medium. In particular, one might be able to use this dependence to determine average ionic charge states of SEPs. In the coming pages, the question is addressed as to how one might be able to use the velocity/rigidity dependence of SEP decay timescales to determine average ionic charge states.

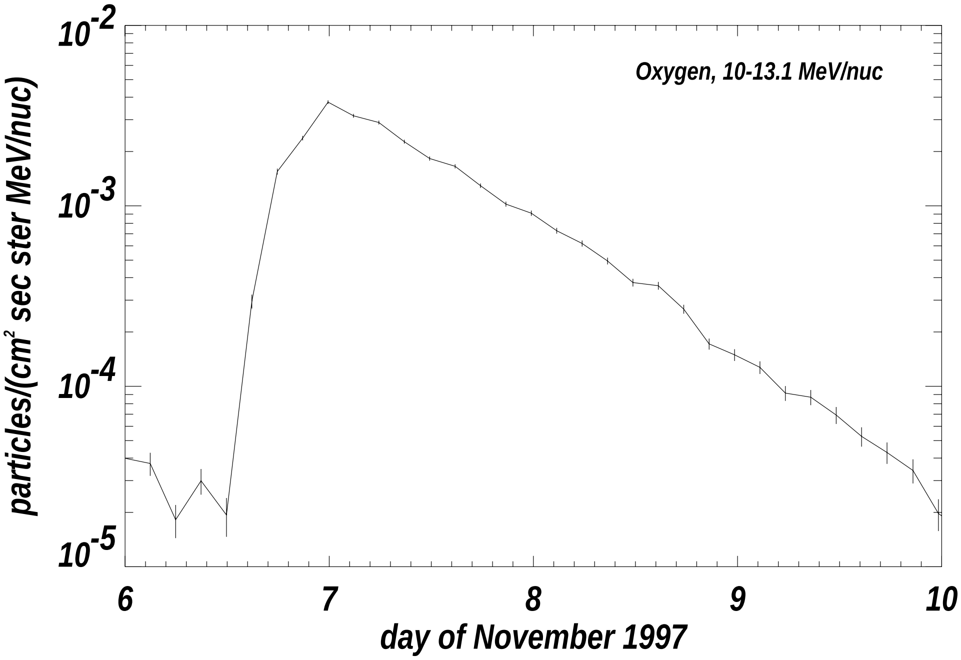

Figure 2.1: Time intensity profile of oxygen at 10 – 13.1 MeV/nuc in the November 6, 1997 solar particle event. Note the hours-long rise time, but the days-long exponential decay phase. The fluxes are 3-hour averages from the ACE/SIS instrument.

For the last forty years or so, various efforts have been made to accurately describe the time intensity and anisotropy profiles of solar particle events. Large SEP events generally follow similar time intensity profiles: a rapid (∼hours) rise, followed by a slow (∼days) exponential or quasi-exponential decay, as was first observed before the Space Age in a ground-level event by Meyer, Parker & Simpson (1956). Figure 2.1 shows a typical time intensity profile for a solar particle event. The fluxes plotted in Figure 2.1 are three hour averages for oxygen ions at 10-13.1 MeV/nuc as measured with the SIS instrument. The uncertainties shown are purely statistical, with Gaussian statistics (that is, for N particles observed, the uncertainty is $\sigma_N = \sqrt{N}$). The flux of oxygen ions rises by almost three orders of magnitude over the course of a few hours, but then decays away exponentially over the course of a few days.

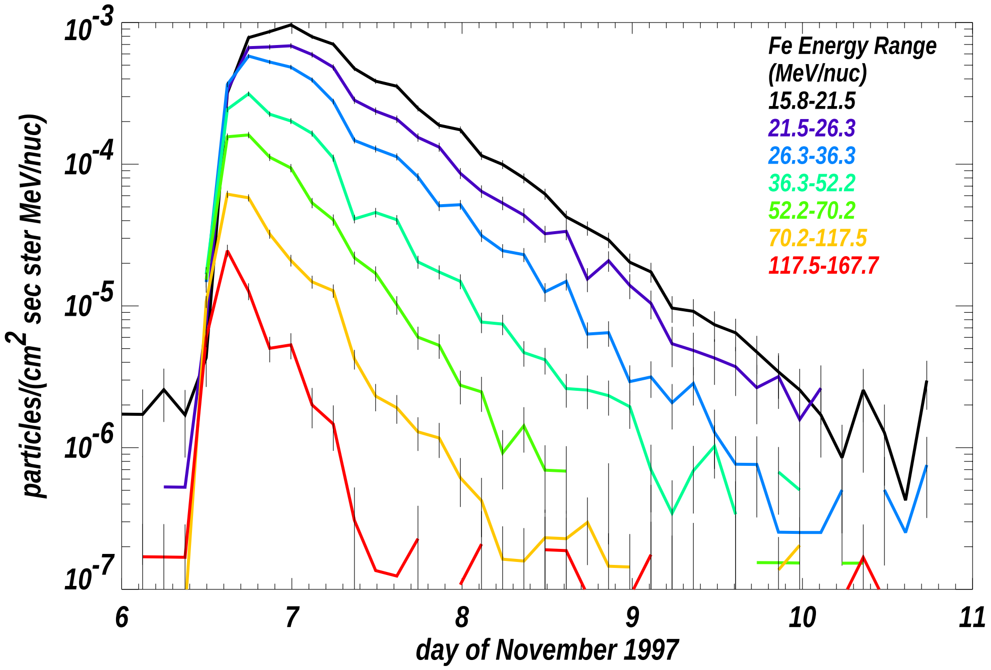

Figure 2.2: Fluxes of iron at various energies in the November 6, 1997 solar particle event. As energy increases, the flux decays away more rapidly.

Figure 2.2 shows time intensity profiles for iron at different energies. The fluxes here are three hour averages. Iron flux is seen to decay away more rapidly at higher energies: there is an energy dependence (or rigidity dependence) to the decay timescale.

There are several different models that describe the physical process of the transport of SEPs (Dalla *et al.*, 2002). Of the models presented in Dalla *et al.* (2002), only interplanetary diffusion has the capability to explain the energy dependent (or rigidity dependent) decay timescales that are observed in the SIS data. The models of continuous acceleration at the shock front (Reames, Barbier & Ng, 1996) and the magnetic bottle/reservoir (Reames, Kahler & Ng, 1997) do not contain any explicit energy or rigidity dependence and are usually invoked to explain the invariant (time and space independent) spectra that are observed at low energies (Reames, Kahler & Ng, 1997). The extended leakage model of Simnett (1996) may not be an accurate model for propagation: it predicts that particle flux should change on sector crossings or with different solar wind conditions, which is not what is observed by Dalla *et al.* (2002) using Ulysses data. In contrast, the interplanetary diffusion model might well provide the needed rigidity dependence for the decay timescale τ. It will be found that this dependence will show up in the diffusion coefficient κ. The form of the rigidity dependence of κ is given by quasi-linear theory.

Early theoretical efforts, such as that in Meyer, Parker & Simpson (1956), described a solar particle event as an impulsive injection, followed by diffusion away from the inner heliosphere through a medium. This medium might be a thick shell, a thin shell, or be in a number of other configurations. As the years have gone by, refinements have been made to this model, with such additions as a diffusion cavity that extends from the Sun past 1 AU with an outer boundary, convection in the solar wind, and adiabatic cooling (Parker, 1963; Burlaga, 1967; Forman, 1971; Lupton, 1973; Lupton & Stone, 1973). All of these authors solve a Fokker-Planck equation for SEP particle density n, sometimes called the Parker equation:

$$\frac{\partial n}{\partial t} = \vec{\nabla} \cdot (\underline{\underline{\kappa}} \cdot \vec{\nabla} n) - \vec{\nabla} \cdot (n\vec{V}) + \frac{1}{3}\vec{\nabla} \cdot \vec{V} \left[\frac{\partial}{\partial T}(\alpha(T)Tn)\right]. \tag{2.1}$$

Here, κ is the diffusion coefficient, V is the solar wind speed, assumed to be radial, and T is the particle kinetic energy. In this equation, the terms on the right are the diffusive term, the convection term, and the adiabatic energy loss term.

2.2 Rigidity and the physics of SEP propagation

It will be shown below how a particle population's decay timescale will depend on that population's average rigidity. In order to understand what follows, it is important to understand exactly what rigidity is. A particle's rigidity is defined as its momentum per unit charge. A useful way to think about rigidity is that the particle's Larmor radius r_L (also called its gyroradius) in a uniform magnetic field B_0 is given (in the non-relativistic treatment) as

$$r_L = \frac{mv}{qB_0} = \frac{R}{B_0}. \tag{2.2}$$

Here, v, m, and q are the particle's speed, mass and charge, and R is then the rigidity. At relativistic energies, the rigidity is given by

$$R = \frac{A}{Qec}\left[E_{KE/n}^2 + 2E_{KE/n}m_p c^2\right]^{\frac{1}{2}}. \tag{2.3}$$

Here, A is the atomic number of the particle (number of nucleons), Q is its charge state, e is the charge of the proton (so that $q = Qe$), $E_{KE/n}$ is the particle's kinetic energy per nucleon, and m_p is the mass of the proton ($\sim$ 938 MeV/c^2). This particular form of the rigidity is chosen because of the way energy measurements are done for SEPs. If $E_{KE/n}$ is measured in MeV/nuc, as is customary for SEP measurements, then rigidity is measured in units of MV/c, which is usually abbreviated MV.

One may well ask what gives rise to the diffusion coefficient in the Fokker-Planck equation for SEP transport. Against what do the SEPs scatter to create diffusion? For that matter, why is there diffusion at all? Why do SEPs not simply stream out of the Sun to the observer in a laminar flow? The answer lies in the nature of the interplanetary medium.

Even before the space age started, it was predicted from observations of comet tails that space is filled with an extremely rarefied plasma streaming from the Sun (Biermann, 1951). This plasma, dubbed the solar wind (Parker, 1958a), is composed of the same material that makes up the corona: mostly protons, with some helium and heavier material. The flow is supersonic and radial away from the Sun, with speeds around 400 km/sec. See Fisk *et al.* (2000) for a recent discussion of the theory of the origins of the slow solar wind. In essence, solar wind is coronal material that is heated by the Sun itself and boiled off. The boundary between the corona and the solar wind is merely the point where the particle velocity becomes large compared to the sound speed, or where turbulent flow is overtaken by supersonic (streaming) flow. The solar wind plasma is only part of the picture, however. The other part is the solar and interplanetary magnetic field.

The Sun is basically a huge ball of hot dense plasma. It has an extremely intense magnetic field, by far the most intense of any object in the solar system. At solar minimum, the solar magnetic field is nominally a dipole. Were there no solar wind, this would be the end of the story. There is a solar wind, however, and according to magnetohydrodynamics, a magnetic field in a plasma will not move with respect to that plasma. So as the solar wind streams away from the Sun, it carries "frozen in" solar magnetic field with it. This field becomes the interplanetary magnetic field. The equilibrium configuration of the field was first worked out by Parker (1958b) to be an Archimedean spiral, thereafter called the Parker Spiral.

If the solar wind had a perfectly smooth, laminar flow, and the interplanetary magnetic field were a perfect Parker Spiral, the story would end here. In reality, the solar wind flow is actually quite turbulent. Since the magnetic field is frozen in, it too becomes turbulent: the field can be thought of as the Parker spiral with a second random, turbulent component. Part of this turbulent component is comprised of the Alfvén waves that arise from particle acceleration. This component will have large variations in direction and magnitude on various length scales. Oftentimes, the turbulence is thought of as a discreet set of "magnetic irregularities" that flow at the solar wind speed away from the sun. This picture is not quite accurate, however. The power spectrum of the magnetic turbulence is continuous: turbulence exists at many length scales, continuously through the region in which SEPs propagate. As an energetic particle moves through the inner heliosphere and encounters this turbulent component of the magnetic field, it will pitch angle scatter into a random direction. Whether and how the particle will scatter depends on whether its Larmor radius is comparable in size to the length scale of the turbulence at that point, or much smaller, or much larger. For instance, extremely high energy ($\sim 10^{21}$ eV) cosmic rays will not tend to scatter off of the turbulent component of the interplanetary magnetic field since their gyroradii are larger than the Solar System (indeed, larger than the galaxy). Likewise, low energy pickup ions will also not tend to pitch angle scatter off of the turbulence, since their Larmor radii are much smaller than the typical turbulent length scale.

The detailed theory that derives scattering mean free paths of SEPs from the properties of the interplanetary magnetic field and its turbulence is called quasi-linear theory (QLT). QLT was first proposed by Jokipii (1966) in an effort to determine a diffusion coefficient from the power spectrum of measured interplanetary magnetic fields. An early history of QLT is given in Palmer (1982); a recent review is given in Dröge (2000a).

Dröge (1994) shows that the mean free path λ scales as a power law in the rigidity R:

$$\lambda = \lambda_0 R^{\gamma_0} = \lambda_0 R^{0.2-0.4} \tag{2.4}$$

The normalization constant λ_0 and the power law index γ_0 depend on various parameters of the solar event, including the magnetic field strength, the solar wind speed, and the power spectrum of the interplanetary magnetic turbulence. The range of 0.2–0.4 represents typical values for γ_0 as derived by Dröge (1994) from energetic electron and ion data. In a multispacecraft study during two solar events in November and December of 1977, Beeck *et al.* (1987) measured rigidity dependences of $\lambda \sim R^{0.45}$ and $\lambda \sim R^{0.2}$ respectively.

The diffusion coefficient depends on the mean free path in a very straightforward way:

$$\kappa = \frac{1}{3} v \lambda, \tag{2.5}$$

where v is the particle speed. From this one deduces the velocity and rigidity dependence of the diffusion coefficient:

$$\kappa = \frac{1}{3} v \lambda_0 R^{\gamma_0}. \tag{2.6}$$

2.3 A tale of two solutions

Though there have been more sophisticated refinements added to the model, such as focused transport (see, for instance, Earl, 1976), during the decay phase of a solar particle event the older (and simpler) solutions can still be reasonably accurate. Detailed effects, such as those due to focused transport, may be ignored in this phase of the event: these effects are important only in the event onset, when anisotropies are frequently large, and the Fokker-Planck equation cannot be used (Jokipii, 1971). Particle focussing is also more important close to the Sun, where $\nabla \cdot B$ is large. The two simple solutions of the Parker equation of Forman (1971) and Lupton (1973) (also Lupton & Stone, 1973) describe the equilibrium decay phase of a solar particle event when anisotropies are small.

In finding these two solutions, many simplifying assumptions are made: all quantities (except for particle density n) are assumed to be independent of energy; the solar wind speed V is assumed to be radial and constant with time; a perfectly absorbing boundary exists at

$r = L$ such that the particle density vanishes at L; terms in the diffusion tensor relating to drifts are assumed to be small; additionally, Forman assumes that the terms in the diffusion tensor $\underline{\underline{\kappa}}$ relating to perpendicular diffusion are small and that the magnetic field is radial, whereas it is more appropriately described by a Parker spiral (Parker, 1958b). The chief difference between the two solutions is in the form of the diffusion coefficient assumed. Forman assumed a diffusion coefficient that was proportional to the radius r from the Sun:

$$\kappa = \kappa_0 r. \tag{2.7}$$

In solving the Fokker-Planck equation (2.1), κ_0 is treated as a constant.

Lupton assumed a diffusion coefficient that was constant with radius. For both solutions, the diffusion coefficient was treated as constant with energy (particles at different energies were treated as separate populations), though both authors considered the models at various values of κ, and Lupton applied different κ to different energy particles. As perpendicular (cross-field) diffusion has been shown to be small in the inner heliosphere (Palmer, 1982), only the radial solution of each model need be considered. In effect, only leakage radially away from the Sun is considered; leakage out of the side of the cavity is ignored. Since the length scale for drifts is very large (Zank *et al.*, 1998), the terms in the diffusion tensor relating to drifts are also ignored. The two different forms of the diffusion coefficient lead to different radial solutions.

In the Forman solution, the characteristic decay time τ_F depends on the diffusion coefficient κ in the following way:

$$\tau_F = \frac{4L}{\left(j_{\eta,1}\right)^2 \kappa_0} \tag{2.8}$$

Here, κ_0 is defined in (2.7), L is the boundary of the diffusive cavity (taken by Forman to be about 2.3 AU), $j_{\eta,1}$ is the first nonzero value of a dimensionless quantity x where the Bessel function $J_\eta(x)$ goes to zero, and η is given by

$$\eta = 2\left[\left(1 - \frac{V}{2\kappa_0}\right)^2 + \frac{2CV}{\kappa_0}\right]^{\frac{1}{2}}. \tag{2.9}$$

Here, V is the solar wind speed, and C is the Compton-Getting factor. The Compton-Getting effect was first noted by Compton & Getting (1935); full discussions of the effect may also be found in Gleeson & Axford (1968) and Forman (1970). SEPs propagate in a medium that is itself moving: the solar wind. If the SEP flux is isotropic in the solar wind frame, then when a spacecraft examines SEPs, it will observe an anisotropic effect on the particle energy: particles arriving from upstream in the solar wind will have a slightly higher energy than in the solar wind frame, and particles coming from downstream will have a slightly lower energy. At a given fixed energy in the spacecraft frame, one is actually sampling two (or more) different energies; the flux observed will not be the correct one for that energy in the solar wind frame. Instead, the observed flux must be multiplied by the Compton-Getting factor, which is related to the shape of the particle flux spectrum. If the differential particle flux $j(E)$ (sometimes written dJ/dE) is given by

$$j(E) \sim E^{-\delta}, \tag{2.10}$$

and if adiabatic deceleration is the only energy loss mechanism, then the Compton-Getting factor is given by

$$C = \frac{2 + 2\delta}{3}. \tag{2.11}$$

In the solution where κ = constant is assumed (Lupton, 1973; Lupton & Stone, 1973) the corresponding decay timescale τ_L is given by

$$\tau_L = \frac{\kappa}{4\kappa^2\psi + V^2} \tag{2.12}$$

where once again, V is the solar wind speed, and ψ solves the boundary condition

$$F_0\left(\frac{\beta}{2\sqrt{\psi}}, \sqrt{\psi}L\right) = 0 \tag{2.13}$$

where F_0 is a Coulomb wave function (a form of confluent hypergeometric function), and β (which here is not particle speed) is given by

$$\beta = \frac{V(2C-1)}{\kappa} \tag{2.14}$$

Once again, C is the Compton-Getting factor.

A third and earlier solution by Burlaga (1967) incorporated diffusion only. The terms of the Fokker-Planck equation associated with the solar wind speed, that is, convection and adiabatic cooling, were neglected. In this solution, one finds the decay timescale τ_B to be given by

$$\tau_B = \frac{L^2}{\pi^2\kappa} \tag{2.15}$$

Figure 2.3 shows calculations of the decay rate, $1/\tau$, for the three different solutions of the Parker equation as a function of the diffusion coefficient κ. For these calculations, a boundary of 3 AU was used and the solar wind speed was assumed to be 400 km/sec. The SEP spectral index δ was assumed to be 3. As can be seen in Figure 2.3, the decay

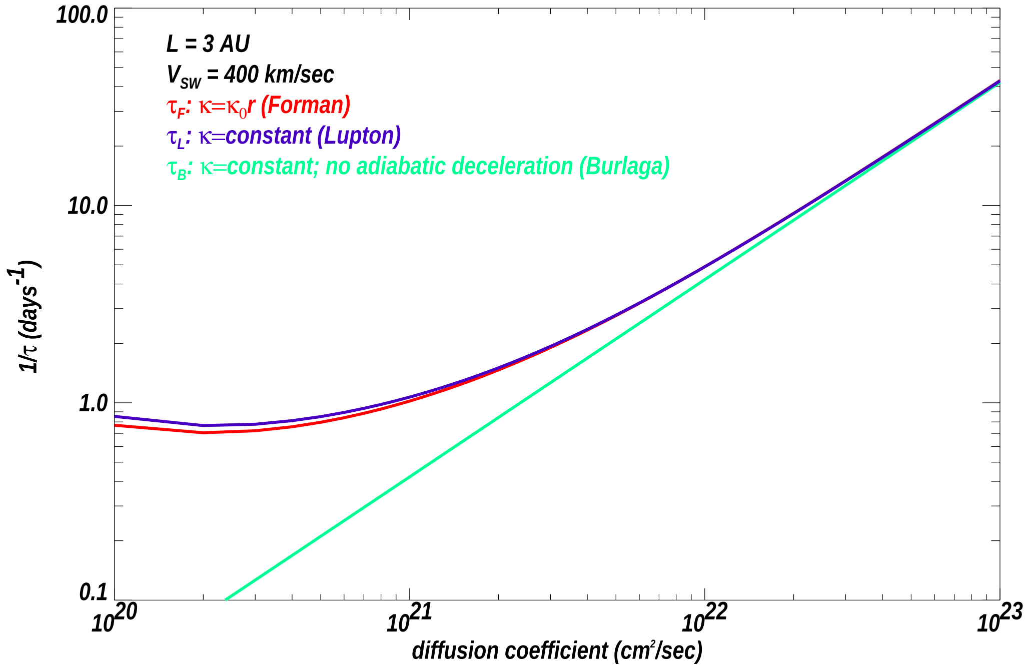

Figure 2.3: Model calculations of decay times as a function of the diffusion coefficient for the three solutions of the Parker equation discussed.

timescales τ_L and τ_F are very similar at all values of κ. At large κ, all three decay times converge: at large κ, τ_L and τ_F are inversely proportional to κ.

For τ_F at large κ, one can see from (2.9) that the terms in η involving κ become small and η tends to a value of 2. Thus, the $j_{\eta,1}$ turn into $j_{2,1}$, and the decay time is inversely proportional to the diffusion coefficient. Examining the large κ behavior of τ_L, it can be seen from (2.14) that at large κ, β tends to zero. Thus, from (2.13), ψ becomes independent of the diffusion coefficient. For large enough κ, the solar wind speed V can be neglected in (2.12) (the κ term dominates), and once again, the decay time will be inversely proportional to the diffusion coefficient. It can be seen in Figure 2.3 that at large κ, both τ_F and τ_L converge to the value τ_B that was derived by Burlaga (1967) neglecting convection and adiabatic deceleration. Indeed, one finds that at large κ, ψ is inversely proportional to L^2. At large κ (and for $V \to 0$), one finds

$$\psi = \frac{\pi^2}{4L^2}. \tag{2.16}$$

At smaller κ, τ_f and τ_L diverge from τ_B as effects due to convection and adiabatic cooling become important. At intermediate κ ($\sim 10^{20} - -10^{21}$cm^2/sec) both τ_F and τ_L become mostly flat with κ, and at low κ ($< 10^{20}$cm^2/sec) decrease with κ. This fits with the observations at intermediate energies of time and space independent particle spectra: in other words, with decay times that are independent of energy and species (Reames, Kahler & Ng, 1997; McKibben, 1972). At intermediate κ, both τ_F and τ_L are dominated by a decay timescale τ_C due to convection and cooling. This decay timescale τ_C is given by

$$\tau_C = \frac{r_L}{2CV}. \tag{2.17}$$

Once again, V is the solar wind speed, C is the Compton-Getting factor, and r_L is the distance from the Sun of the highest flux region in the equilibrium decay.

2.4 The road to simplicity: parameterization of the solutions

The inclusion of the factors η and ψ in the two solutions of the Parker equation makes understanding decay timescales in terms of those solutions very complicated, perhaps more complicated than is strictly necessary. However, since both solutions tend to behave the same way at intermediate to high energies (and κ), there might be a much simpler way to parameterize the behavior accurately. In effect, at intermediate to high energies one sees two superposed decays for the flux j. On the one hand, there is a decay timescale τ_C that is constant with energy and particle species (or velocity and rigidity) that dominates at intermediate energies. On the other hand, diffusion sets up a decay timescale τ_D that depends on the diffusion coefficient, and dominates at higher energies. This suggests the following parameterization:

$$j = De^{-\frac{t}{\tau_C}} e^{-\frac{t}{\tau_D(\kappa)}} = De^{-\frac{t}{\tau}} \tag{2.18}$$

From this, one can see that the decay timescale of a particle population that will be measured will be given by

$$\frac{1}{\tau} = \frac{1}{\tau_C} + \frac{1}{\tau_D(\kappa)} \tag{2.19}$$

This is a much simpler expression mathematically than either (2.8) or (2.11) above, because only the (much simpler) limiting forms of the decay constant, τ_C and $\tau_D(\kappa)$, are used. Recall from (2.5) and (2.6) that the diffusion coefficient depends on the particle rigidity. Then the large-κ decay timescale τ_D will be given by

$$\tau_D = W_1 \frac{1}{\frac{1}{3} v\lambda} = \frac{1}{W_0 v R^{\gamma_0}}. \tag{2.20}$$

Here, W_1 is the constant of proportionality between κ and τ_D; it will have different values for each solution to the Parker equation. The constant W_0 folds in the constant λ_0 from QLT. In fitting the data it will be allowed to float. This suggests an expression for τ_D that parameterizes the various solutions of the Parker equation for SEP propagation:

$$\frac{1}{\tau} = \frac{1}{\tau_C} + \frac{1}{\tau_D(\kappa)} = \frac{1}{\tau_C} + W_0 v R^{\gamma_0}. \tag{2.21}$$

We now have an expression for the decay timescale in terms of the velocity and the rigidity of the particle species. We are most of the way to an accurate parameterization of the solutions. This equation must be re-expressed in terms of the quantity that is measured in an SEP instrument, particle energy, and the quantity that is finally sought: the average particle charge state.

Recall from (2.3) that the rigidity, in MV/c, of a particle depends on its charge state Q (in integer units of proton charge) and its energy $E_{KE/n}$ (in MeV/nuc):

$$R = \frac{A}{Qec}\left[E_{KE/n}^2 + 2E_{KE/n}m_pc^2\right]^{\frac{1}{2}}, \tag{2.22}$$

which at the low energies of SEPs can be re-written in the nonrelativistic form as

$$R = \frac{A}{Qec}\left[2E_{KE/n}m_pc^2\right]^{\frac{1}{2}}. \tag{2.23}$$

Also, recall that the speed v is given by

$$\frac{v}{c} = \sqrt{\frac{2E_{KE/n}}{m_pc^2}} \tag{2.24}$$

Then the parameterization in (2.21) may be rewritten as

$$\frac{1}{\tau} = \frac{1}{\tau_C} + W_0vR^{\gamma_0} = \frac{1}{\tau_C} + W_0c\sqrt{\frac{2E_{KE/n}}{m_pc^2}}\left[\frac{A}{Qec}\left[2E_{KE/n}m_pc^2\right]^{\frac{1}{2}}\right]^{\gamma_0}. \tag{2.25}$$

Equation (2.25) can be simplified quite a bit by recalling that W_0 is allowed to float. Then all of the constants are folded into a new constant W, leaving the quantities that are of interest, A, Q, γ_0 and $E_{KE/n}$:

$$\frac{1}{\tau} = \frac{1}{\tau_C} + W\left[\frac{A}{Q}\right]^{\gamma_0} E_{KE/n}^{\frac{\gamma_0+1}{2}} = \frac{1}{\tau_C} + W\left[\frac{A}{Q}\right]^{2\gamma-1} E_{KE/n}^{\gamma}. \tag{2.26}$$

Here, the new power law index $\gamma = \frac{\gamma_0+1}{2}$ is the actual quantity that will be fit to the data.

2.5 The joys of comparing to carbon

Equation 2.26 does not actually determine, by itself, the charge state Q of a particle species. There is a degeneracy in the free parameters W, Q, and γ. The constant W is treated as a free parameter in the system since it depends on the power spectrum of the interplanetary magnetic turbulence (and on L), which as can be deduced from fitting particle time intensity profiles and anisotropies (Dröge, 2000b,a) varies from event to event. In examining the measured decay timescales for various particle species in a solar event, the power law index γ is also allowed to float, and the Q is unknown. They all combine in a degenerate way: W is multiplied by Q which is raised to a power of γ. However, what happens when two particle species X and Y have the same decay timescale? Since the quantities τ_C, γ, and W are the same for both species, it can be seen from (2.26) that

$$\left[\frac{A_X}{Q_X}\right]^{2\gamma-1} E^{\gamma}_{(KE/n)_X} = \left[\frac{A_X}{Q_Y}\right]^{2\gamma-1} E^{\gamma}_{(KE/n)_Y} \tag{2.27}$$

Both $E_{(KE/n)_X}$ and $E_{(KE/n)_Y}$ are measured. Then we have

$$E_{(KE/n)_Y} = \left[\frac{Q_Y}{A_Y}\frac{A_X}{Q_X}\right]^{\frac{2\gamma-1}{\gamma}} E_{(KE/n)_X} = \alpha E_{(KE/n)_X} \tag{2.28}$$

where a multiplicative constant is now defined:

$$\alpha \equiv \left[\frac{Q_Y}{A_Y}\frac{A_X}{Q_X}\right]^{\frac{2\gamma-1}{\gamma}} . \tag{2.29}$$

If the charge state of species Y is known, then the charge state of species X can be found by determining the multiplicative constant, α, that separates the energies (in MeV/nuc) of the particle species at the same decay timescale τ. Then the charge state of species X is found by solving (2.29):

$$Q_X = \alpha^{\frac{\gamma}{1-2\gamma}} \frac{Q_Y}{A_Y} A_X. \tag{2.30}$$

In applying this parameterization to the data, the inverses of the decay lifetimes for each species are fitted to the following equation:

$$\frac{1}{\tau} = \frac{1}{\tau_C} + W(\alpha E)^{\gamma}. \tag{2.31}$$

The values of τ_C, γ and W are all allowed to float, but are constrained to be the same for all species. For each species, α is allowed to float. In this analysis, the reference element used is carbon. For carbon, $\alpha = 1$ is assumed. In order to account for the mass distributions in SEPs, an average mass for each particle species is used; this average mass is calculated from the abundances of nuclides presented in Anders & Grevesse (1989).

2.6 Comparing the parameterization to the solutions

At very low energies (and small κ), this parameterization naturally does not apply: at small κ, the decay rate increases with decreasing κ. However, that region of the parameter space is, in energy, far lower than the energies that are observed in SIS. The point of the parameterization is to provide a simplified but accurate description of the propagation model for SEPs at energies E $\geq$ 10 MeV/nuc. Figure 2.4 shows comparisons between model calculations and the corresponding fits to those calculations using the parameterization.

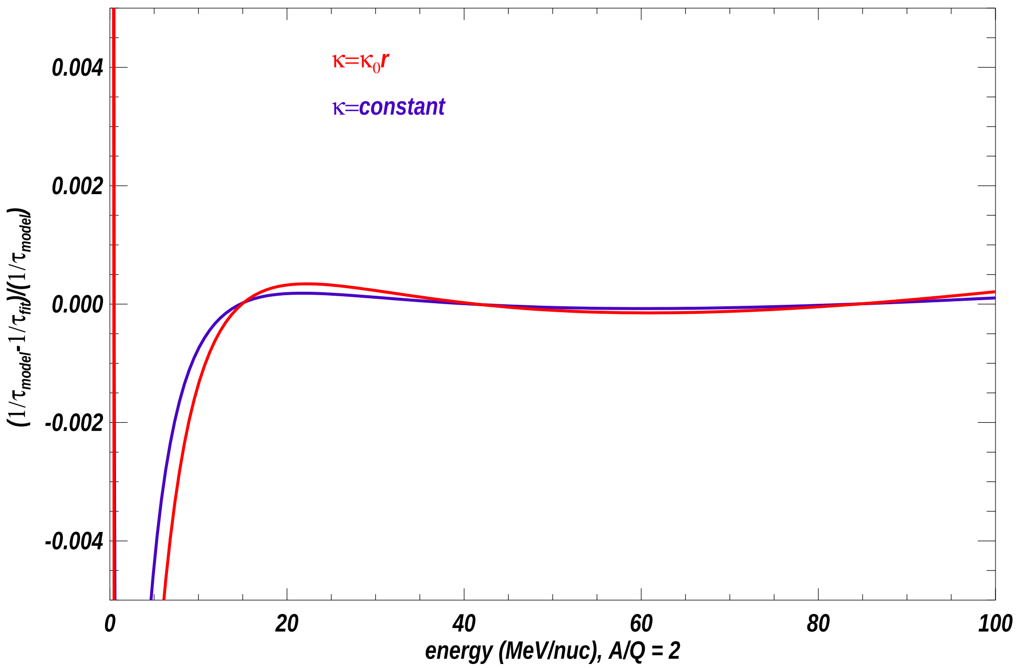

Figure 2.4: Comparison of decay rates calculated for κ = constant (Lupton, 1973) and $\kappa = \kappa_0 r$ (Forman, 1971) solutions with the corresponding fits using the $1/\tau_C + 1/\tau_D(\kappa)$ parameterization.

For Figure 2.4, the $\kappa = \kappa_0 r$ and κ = constant solutions were used to calculate predictions of $1/\tau$ for various values of κ. For these calculations, a solar wind speed of V = 400 km/sec was assumed, along with an outer boundary of $L = 3$ AU. The spectral shape was assumed to be $f \sim E^{-3}$. The results from Dröge (2000b,a) and Dröge (1994) were used to convert $1/\tau(\kappa)$ into a function of energy per nucleon for $A/Q = 2$ in the following manner: the scattering mean free path was assumed to vary with the rigidity as $\lambda \sim R^{0.4}$, and the normalization λ_0 was chosen such that the mean free path was $\lambda = 0.1$ AU at a rigidity $R = 100$ MV/c.

In order to test the validity of the parameterization, the calculated values of $1/\tau$ as a function of energy per nucleon were used as pseudo-data and fitted with (2.31), setting $\alpha = 1$. In Figure 2.4, the fractional deviation $(1/\tau_{Model} - 1/\tau_{Fit})/(1/\tau_{Model})$ is plotted versus the energy per nucleon of a particle species with $A/Q = 2$ for both the $\kappa = \kappa_0 r$ and $\kappa =$ constant solutions. Note that in the limit $\tau_C \rightarrow \infty$, the solution of Burlaga (1967) is described exactly by the parameterization. Therefore when fitting data to the parameterization, a finite τ_C will denote a system where adiabatic deceleration is important. It can be seen in Figure 2.4 that the fractional deviation for $E > 7$ MeV/nuc is less than half a percent for both $\kappa = \kappa_0 r$ and $\kappa =$ constant. For $E > 10$ MeV/nuc, the deviation is less than 0.1 percent! It can be seen that the parameterization describes both solutions equally well: the small differences in the curves in Figure 2.4 are not significant. These numbers are for a particular set of parameters, but the agreement between the solutions and their parameterizations does not change appreciably for other values of solar wind speed, cavity size, and spectral index.

The excellent agreement between the model calculations and their parameterizations provides confidence in this method for describing the various solutions of the Parker equation. Furthermore, it gives a great deal of confidence in this method as a way of calculating charge states: regardless of which solution is chosen, whether the diffusion coefficient in the inner heliosphere depends linearly with radius from the Sun or is independent of it, or whether adiabatic deceleration is an important effect, this parameterization should accurately describe any of these solutions at the energies of interest.

Chapter 3

Welcome to the Machine: Charting the Arduous Journey through the Forests of Method and Data Analysis

3.1 Of spacecraft and Lagrange points

When one starts learning about solar energetic particles (SEPs), one of the first things to be noticed is that it is very hard to detect them here on Earth. Only the most intense solar particle events have effects that can be measured on Earth, such as the event observed by Meyer, Parker & Simpson (1956). Such ground level events, or GLEs, are pretty rare (Stoker & Makgamathe, 1990). The problem is that at SEP energies, the Earth's magnetic field deflects most particles, and the atmosphere does a good job of absorbing the rest. In fact, even in a GLE, what is observed at the Earth's surface is not the primary SEP flux, but rather the neutrons that are generated from collisions in the upper atmosphere (Meyer, Parker & Simpson, 1956). To really look at SEPs, one needs to get a detector out in space among them, and that means going through all the exciting and complicated machinery and process of spaceflight.

In this work, the data that are used were collected with the Solar Isotope Spectrometer

(SIS) instrument on board the Advanced Composition Explorer (ACE) spacecraft. A full description of the instrument is given in Stone *et al.* (1998a); a broader description of the ACE spacecraft and mission is given in Stone *et al.* (1998c). However, some of that information bears repeating (or at least summarizing) here.

ACE was launched on August 25, 1997, on a mission to explore particle populations ranging in energy from low speed solar wind (∼400 km/sec) up through low energy cosmic rays (≤400 MeV/nuc), and make measurements of the interplanetary magnetic field. The nine instruments on board together make up one of the most comprehensive single spacecraft set of measurements ever done of the interplanetary environment. In order to avoid the effects of the Earth's magnetic field, ACE was sent into a halo orbit around the Earth-Sun L1 point, about one million miles away from the Earth (see Figure 3.1, from the ACE web site).

The concept of the L1 point, or first Lagrange point, is most easily understood by considering a frame of reference corotating with the Earth's orbit. In this frame, the L1 point is the point on the Earth-Sun line where the effects of gravity due to the Earth and Sun balance out with the apparent centrifugal force generated by the orbital motion. In practice, one does not put a spacecraft exactly at the L1 point for two reasons. First, it is only metastable. Along the Earth-Sun line, L1 is an unstable equilibrium point; for motion perpendicular to that line, L1 is a stable equilibrium point. Second, in order to receive a signal from a spacecraft exactly at L1, one would have to point one's radio receiver directly into a very intense radio source: the Sun itself. The solution to both of these problems is the same, and it is called a halo orbit. This orbit is inclined with respect to the ecliptic, and is broad enough that the spacecraft stays outside of the most intense region of solar radio emission. From our perspective on Earth, the shape of the orbit is such that the spacecraft

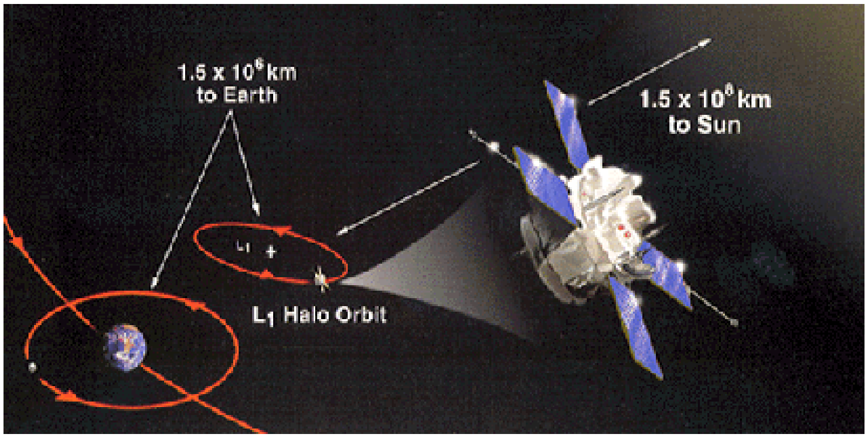

Figure 3.1: Diagram of the ACE halo orbit. From the perspective of an observer on the Earth, the spacecraft orbit appears to make a halo around the Sun. From the ACE web page.

appears to make a halo about the Sun. This orbit is still only metastable: the spacecraft relies on maneuvering thrusters to maintain the orbit. As of this writing, it has been five and a half years since launch, and there are still many years of operations left to go for the spacecraft.

3.2 Catching cosmic rays in a silicon bucket: the ΔE vs. E$'$ technique

In making spacecraft observations of energetic particles, one is faced with two competing issues. On the one hand, one wishes to detect particles at energies comparable to those found in cyclotrons; on the other hand, one wants to keep the weight of the instrument and the power it consumes to a minimum because of the prohibitively high costs of spaceflight. This problem was solved early in the space age by the development of solid state particle telescopes. The SIS instrument aboard the ACE is one of the largest and most complicated examples of this kind of instrument to yet be flown in space (Stone *et al.*, 1998a).

A particle telescope like SIS takes advantage of a method called the ΔE versus E′ technique to measure the atomic number and mass of an incoming energetic particle. Full descriptions of this technique are given in Stone *et al.* (1998b) and in Stone (1974), though a brief description will be given here. In measuring the atomic number and mass of a particle using the ΔE versus E′ technique, one is relying on the notion that a particle of mass M and atomic number Z will lose energy in a unique way as it traverses a material such as silicon. That is, there will be a unique relation between a particle's energy per nucleon E/M and its range R in silicon:

$$R = R_{Z,M}(E/M). \tag{3.1}$$

Equation (3.1) is called a range-energy relation. The exact form of this relation need not be the same for different Z and M, and it changes for each kind of material that a particle can traverse. In analysis of the SIS data, tabulated range-energy tables scaled from the range energy table for hydrogen of Andersen & Ziegler (1977) were used to determine SEP atomic numbers and masses.

One cannot actually use a particle telescope to measure how far a given particle penetrates silicon. Instead, one measures how much energy ΔE the particle loses in a known thickness of silicon, and the particle's residual energy E′. Figure 3.2 shows a schematic of this process. A particle of atomic number Z and mass M hits the silicon detectors at an angle θ. The first detector has a known thickness L: the thickness traversed in this detector will be $L\sec(\theta)$. The total range of a particle with energy $E = \Delta E + E'$ will be $R_{Z,M}(E/M) = R_{Z,M}((\Delta E + E')/M)$. As the particle enters the E' detector, it will have energy E', and will have a range of $R_{Z,M}(E'/M)$ left to go in the detector. The difference

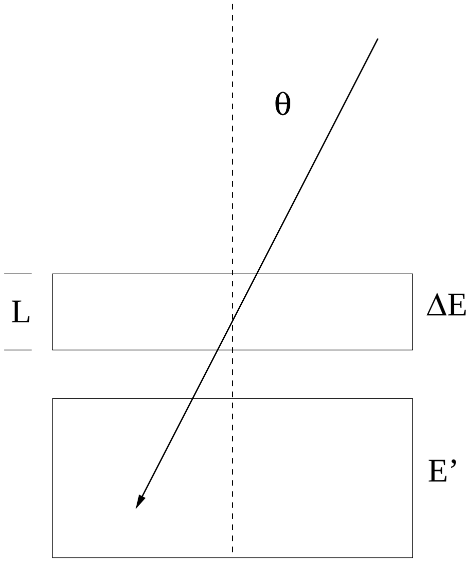

Figure 3.2: Schematic of the ΔE versus E′ method. A particle enters the detector stack at angle θ, depositting energy ΔE in the first detector, and energy E′ in the stopping detector. The thickness of the ΔE detector is L.

between these two ranges is just the amount of material traversed in the dE detector:

$$R_{Z,M}((\Delta E + E')/M) - R_{Z,M}(E'/M) = L \sec(\theta). \tag{3.2}$$

For a given Z and M, equation (3.2) can in principal be solved to give a dependence of ΔE on E'. Figure 3.3 shows an example of this kind of behavior. This figure derives from particles stopping in a particular detector layer (T4) of the SIS instrument. In this figure, the E′ detector is the detector layer in which the particles stop; the ΔE detector is the detector layer just above. Each curve derives from a unique range-energy relation at a given Z and M. The data are from the November 6, 1997, solar particle event. The three thick curves at the lower left hand corner are for (from the bottom) carbon, nitrogen and oxygen. The uppermost thick curve is for iron. Curves for many other particle species can be seen, such as nickel, neon and magnesium.

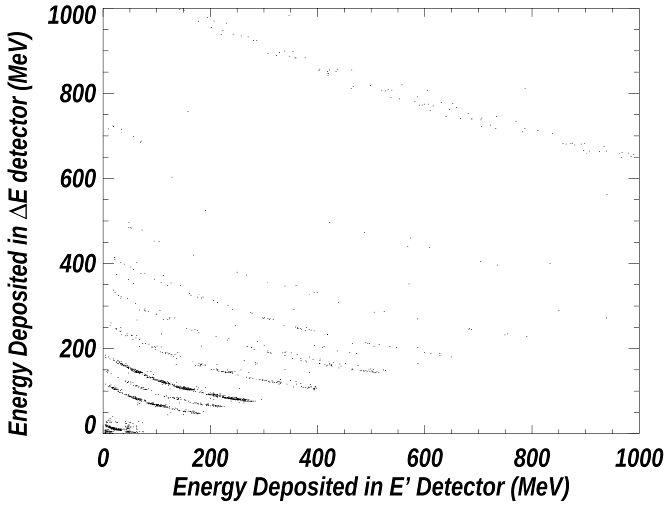

Figure 3.3: Plot of ΔE vs. E$'$, corrected for angle, for particles stopping in the T4 detector of SIS in the November 6, 1997 event.

Equation (3.2) cannot, by itself, determine Z and M. If one assumes that $Z/M = 1/2$ (or, really, that each particle species is monoisotopic, and that there is a specific Z/M), then (3.2) can be solved for Z. Figure 3.4 shows a histogram of atomic charge for the curves in Figure 3.3 making this assumption. Peaks can clearly be seen for carbon, nitrogen, oxygen, neon, sodium, magnesium, aluminum, silicon, sulphur, argon, calcium, iron and nickel. Some of the rarer elements have very small peaks. Neon and magnesium each have two very distinct peaks. One does not actually expect to have neon with $Z = 10.3$. Obviously, the charge of neon is well known to be 10. If that value is used in (3.2), then that equation can be re-solved to find the various masses, which would result in a mass histogram for neon. The second neon peak is for the heavier isotope ^{22}Ne. On this plot, each isotope of an element shows as having a slightly different charge.

The SIS detector scheme is a great deal more complicated than the simple example in Figure 3.2. Figure 3.5 shows a schematic of a stack of detectors in SIS. There are seventeen

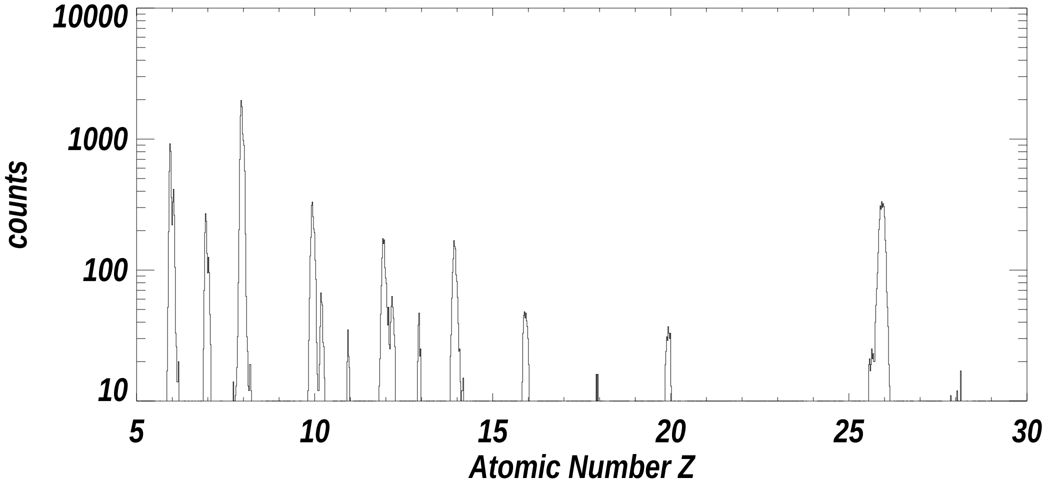

Figure 3.4: Charge histogram of the particles from Figure 3.3.

different detector layers. Not all of the layers are individually instrumentated: as can be seen in the figure, the T6 and T7 detectors are compound detectors, each made up of several silicon wafers with common electronics.

The first two detectors, M1 and M2, are position sensitive, and make up the SIS hodoscope. Each detector is divided into two sides. Each side is composed of 64 individual silicon strips, and is about 34 cm^2 in area. Each strip is 1 mm wide. The two sets of strips are oriented orthogonally to each other. The signal from each strip is separately analyzed, allowing the x (from one side of strips) and y (from the other side) position of an incoming ion to be accurately determined. When a particle goes through both the M1 and M2 detectors, measurements of x and y are made at two different heights in the instrument, and the trajectory of the particle through the instrument may be deduced. This is done to obtain a reliable measurement of the thickness of silicon traversed in the dE detector. The angle information can also be used to infer the anisotropy of the incoming particles.

Underneath the matrix detectors is the main detector stack. The detectors vary in

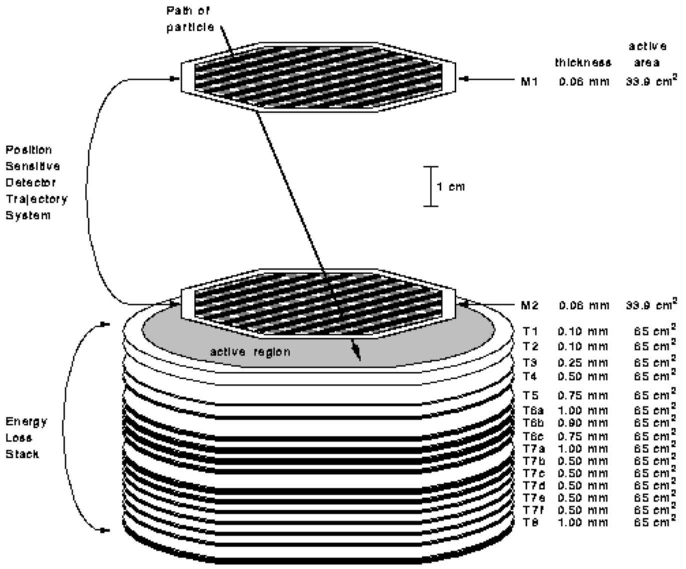

Figure 3.5: Diagram of a SIS stack. Eight silicon detectors, some made of multiple layers, make up the main stack for measuring dE and E′. Two position-sensitive detectors provide trajectory information as well as energy measurements. From the SIS Critical Design Review Document.

thickness from 0.1 mm up to 3.5 mm for the compound detector T7 (which is made up of silicon wafers T7a through T7f), and are about 65 cm^2 in area. The last detector layer, T8, is used in this analysis as a veto layer: particles that deposit energy in T8 are deemed to have penetrated the instrument and not stopped. This plethora of detectors in the stack allows several measurements of dE and E′ for a given particle if that particle stops deep enough in the stack. For the particles in Figure 3.2, the dE chosen was the energy deposited in T3. The E′ plotted was the energy deposited in T4. However, this plot could have been made by using as dE the total energy deposited in M1, M2, and T1-T3, or with a great many other combinations for dE and E′. This redundancy allows for a consistency check for the charge measurements made on all of the particles that stop in T1 through T7. Particles stopping in M2 can have their atomic charge Z measured, but there can be no consistency check, as there is only one way to set up dE and E′.

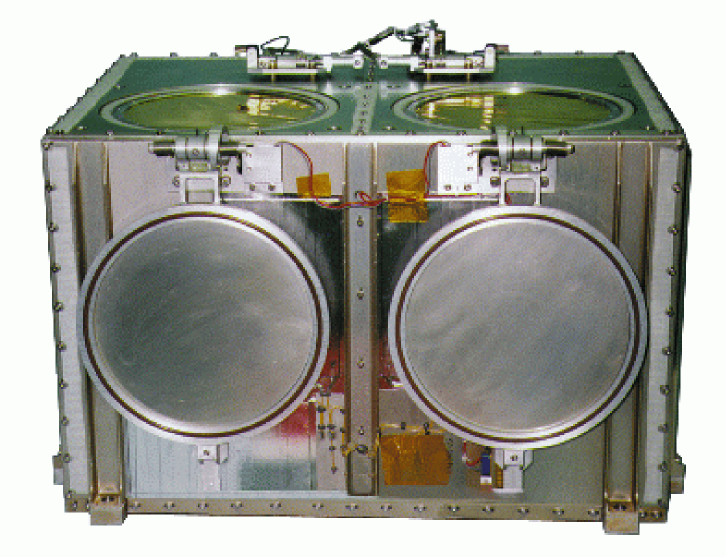

Figure 3.6: The SIS instrument. There are two detector stacks in the instrument. The two large roundels are covers that were opened after launch. From Stone *et al.* (1998a).

Figure 3.6 shows a photograph of the SIS instrument prior to integration onto the spacecraft and launch. SIS is made up of two of the stacks of detectors shown in Figure 3.5. The total geometry factor, or acceptance, of SIS is about 40 cm^2 ster, which makes it the largest solar isotope spectrometer ever flown on a spacecraft. There are many sources of uncertainty in the charge resolution of this kind of instrument, from such things as pixellation of the angle and energy measurements to Landau fluctuations, to name but a couple. A full (and excellent) discussion of the limits of charge resolution for this kind of instrument is given in Williams (1998); a discussion of the these limits specifically for the SIS instrument is given in Stone *et al.* (1998a).

3.3 Getting by with a little help from a friend: ULEIS

The lowest energy SEPs observed with the SIS instrument (or at least, the lowest energy points used in this analysis) are still fairly high in energy at over 9 MeV/nuc. In fitting to the parameterization of Chapter 2, the regime in which τ_C dominates equation (2.18) might not be well represented by the low energy data in SIS. However, there is another instrument on board the ACE spacecraft that measures SEPs in a lower energy band: the Ultra-Low Energy Isotope Spectrometer, or ULEIS (Mason *et al.*, 1998). ULEIS is an instrument quite different from SIS. A particle's speed is measured using a time-of-flight system, and its total energy is measured with a solid state detector. From the particle's speed and energy, its mass is determined. ULEIS cannot determine a particle's atomic number Z, and isomers cannot be resolved. However, its excellent mass resolution allows unique identification of most isotopes of astrophysical interest, and certainly all of those of interest here.

ULEIS can measure oxygen and carbon energies as low as 0.04 MeV/nuc and as high as 10-14 MeV/nuc. The lower energies will not be of interest in this analysis, as they are too susceptible to transient low energy phenomena. However, the higher energy data, those at or around 3-7 MeV/nuc, will prove useful in helping to constrain τ_C in the fits to come.

3.4 Wrangling the data the science cowboy way

In order to examine decay times, one must have measurements of the fluxes of various elements in various energy ranges as a function of time. This is not what the SIS instrument provides directly in the processed raw data – called Level 1 data. Level 1 data consists of pulse heights, time tags and event rates. The pulse heights are used to reconstruct such quantities as energy depositions and angles of incidence. A standard set of procedures is used to process the data into fluxes. These data are made available to the public through the internet, and are called Level 2 data. The data used for this analysis are updated Level 2 data provided by C.M.S. Cohen. There are two differences. First, the updated data make use of the latest instrument analysis. Secondly, Level 2 data exist only for the most common elements in solar particles: helium (SIS does not really do hydrogen), carbon, nitrogen, oxygen, neon, magnesium, silicon, sulfur, and iron. The data used here also include sodium, aluminum, argon, calcium and nickel.

A detailed description of the SIS data processing is given in Stone *et al.* (1998a). The data stream from the SIS instrument is organized into a standardized format called data frames. A major frame is recorded by the instrument every 256 seconds. It contains 256 1-second minor frames that can have pulse height information for up to about ten events. Time tags are placed on the major frames only. When converting to Level 2, all of the particle counts and other pertinent data are put into 256-second bins because of this organization. The data provided by C.M.S. Cohen contain particle counts and calculated fluxes for all of the elements listed above in these 256-second bins. The flux j for a particular element and range is calculated from the counts N, as well as the livetime t_L, the energy interval ΔE and geometry factor GF in the following way:

$$j = \frac{N}{t_L \times GF \times \Delta E}. \tag{3.3}$$

The geometry factor GF and the energy interval ΔE are unique to each range of each element. In high flux (and low livetime) periods, the overall instrument livetime will be affected by factors that arise as a result of a complicated priority system in the instrument. The purpose of the priority system is to select out more interesting events, such as high-Z events with clear single tracks through the hodoscope, and events at higher energies. Therefore each range of each element has its own effective livetime, which might be different from the overall instrument livetime. Having both the fluxes and the counts allows a calculation of the effective livetime, which is not included in the Cohen data.

When there are no counts, the livetime cannot be deduced from the Cohen data: both the counts and flux are identically zero. It is still important to account for zero count periods in the averaging and analysis to follow. For these periods, the overall instrument livetime from the Level 1 data is used. No correction factors are used on this livetime, as the priority system only becomes important in high flux periods. The zero counts periods will generally come from time periods when the fluxes are small.

The 256-second time bins from the spacecraft data are not necessarily the best format with which to analyze decay timescales. Much of the data in this format (or even most, depending on element or range) will consist of zeroes. Such a short time resolution would make it difficult to visualize the data and the fitting: one would never see more than a few counts in any given time bin, and would have long period many bins at the end of the decay phase with no counts. A longer time binning would decrease the zeroes in the data, and provide a more natural way to present the data graphically. For this work the time binning chosen was 10752 seconds, being 42 256-second periods, or approximately three hours.

For finding the three hour average fluxes j_3, the following equation is used:

$$j_3 = \frac{\sum\limits_{i=1}^{42} N_i}{\sum\limits_{i=1}^{42} (t_L)_i \times GF \times \Delta E} \tag{3.4}$$

where the summation is over each of the 42 256-second periods in the $\sim$ three hours. Though the counts N_i and effective livetimes $(t_L)_i$ will change over the course of the 42 periods, the geometry factor GF and energy interval ΔE do not.

In the case of the ULEIS data, the data came from two sources: either in the form of Level 2 data available on the web, or directly from Prof. G. Mason of the University of Maryland. These data are in one hour averages, fluxes with statistical uncertainties. In the case of the Level 2 data, the uncertainties quoted are fractional, that is, they are simply $1/\sqrt{N}$. For these data, three hour averages were done by making weighted averages of the one-hour data in the standard way (see, for example, Bevington, 1969).

3.5 The meat: data analysis

3.5.1 Enter the fish: using maximum likelihood fitting and Poisson statistics

In the journey from decay times to charge states, one is faced with a seemingly trivial first step: finding decay times. It seems easy enough: one has to fit a function for the particle flux j of the form:

$$j = j_0 e^{-\frac{t}{\tau}}. \tag{3.5}$$

When one takes the natural log of this equation, one gets an extremely simple expression: $y = \ln j = A + Bt$, where A and B are constants. The normal way to fit this kind of equation is a linear least squares fit, with Gaussian statistics, and can be done with just about every data analysis program in existence – even with Microsoft spreadsheets. The simplicity of the problem is deceptive, however. At low flux levels, Gaussian fitting results in large systematic deviations from the parent (input) distribution: decay timescales fit using this simple method are systematically longer than the parent timescales, typically by several standard deviations.

A different way to approach this problem is to examine the actual measurement process. SIS is a detector in space, being exposed to a parent population of particle fluxes. The data wrangling in Section 3.4 gives samplings of that parent population in (approximately) three hour bins, along with effective livetimes for those bins. In an approximately three hour period, then, for a given energy range of a given element, two numbers are known: the integer number of particles observed, and the effective livetime fraction. This describes exactly the process of Poisson sampling of a parent population. Using Poisson statistics, along with maximum likelihood fitting, tends to yield better results than linear regression fitting with Gaussian statistics. At low fluxes, though, there are still systematic deviations, though they are smaller than with linear regression. This will lead to a criterion for a threshold number of particles counted in a single bin for the fitting process.

Maximum likelihood fitting is a standard data fitting procedure, and is described in many standard references (see, e.g. Bevington, 1969; Press *et al.*, 1992). It is a relatively straightforward idea: if $p_i = p_i(y_i, y\{x_i; \mathbf{a}\})$ is the probability to measure a given data point y_i for some ideal parent distribution $y(x_i, \mathbf{a})$ which is described by a set of parameters $\mathbf{a}$ for points x_i, then the probability to observe any given set of N data points is given by

$$P = \prod_{i=1}^{N} p_i(y_i, y\{x_i; \mathbf{a}\}) = \prod_{i=1}^{N} \{e^{[-\rho(y_i, y\{x_i; \mathbf{a}\})]} \Delta y\}. \tag{3.6}$$

Here, ρ is defined as the negative logarithm of the probability density: $\rho(y_i, y\{x_i; \mathbf{a}\}) \equiv -\ln(p_i/\Delta y)$. The best fit for the data is found when the likelihood $W = \ln P$ has been maximized; that is, at the maximum likelihood. This corresponds to minimizing $-\ln P \sim \sum_{i=1}^{N} \rho(y_i, y\{x_i; \mathbf{a}\})$. For a normal distribution, we have (ignoring normalization):

$$p_{Normal} \sim e^{(-[y_i - y(x_i)]^2/\sigma_i^2)} \Delta y. \tag{3.7}$$

Then the quantity to be minimized is given by

$$\sum_{i=1}^{N} \rho(y_i, y\{x_i; \mathbf{a}\}) = \sum_{i=1}^{N} \frac{[y_i - y(x_i)]^2}{\sigma_i^2} = \chi^2. \tag{3.8}$$

Equation 3.8 merely reproduces linear least-squares fitting, and shows that χ^2 is the natural maximum likelihood estimator for normal statistics (Press *et al.*, 1992). Note that the extra factor of Δy is ignored in the maximizing of W, as it is only a constant. A Poisson distribution has a form quite different from the normal distribution:

$$p_{Poisson}(x, \mu) = \frac{\mu^x}{x!} e^{-\mu} \Delta y. \tag{3.9}$$

Here, μ may be described by several variables, and can be thought of as the "true" or parent physical quantity that is sampled by the data points y_i in the samples x_i. In finding the maximum likelihood, then, one is minimizing the following quantity:

$$-W = -\ln P_{Poisson} = \sum_{i=1}^{N} [\mu - x_i \ln \mu + \ln x_i!] - N\Delta y. \tag{3.10}$$

The terms $N\Delta y$ and $\sum_{i=1}^{N} x_i!$ only introduce constant offsets to the likelihood, and can be ignored for the purposes of finding the maximimum likelihood with respect to μ. In the decay phase of a solar particle event, the quantity μ is the true number of particles in a given three hour period, multiplied by the effective livetime fraction of that three hour period for the energy range and element in question:

$$\mu = (Ae^{-t/\tau} + B) * \text{livetime fraction}. \tag{3.11}$$

Since t and the livetime fraction are arrays of three hour periods, μ is actually a set of numbers. The quantity A is the overall normalization, which will be directly related to

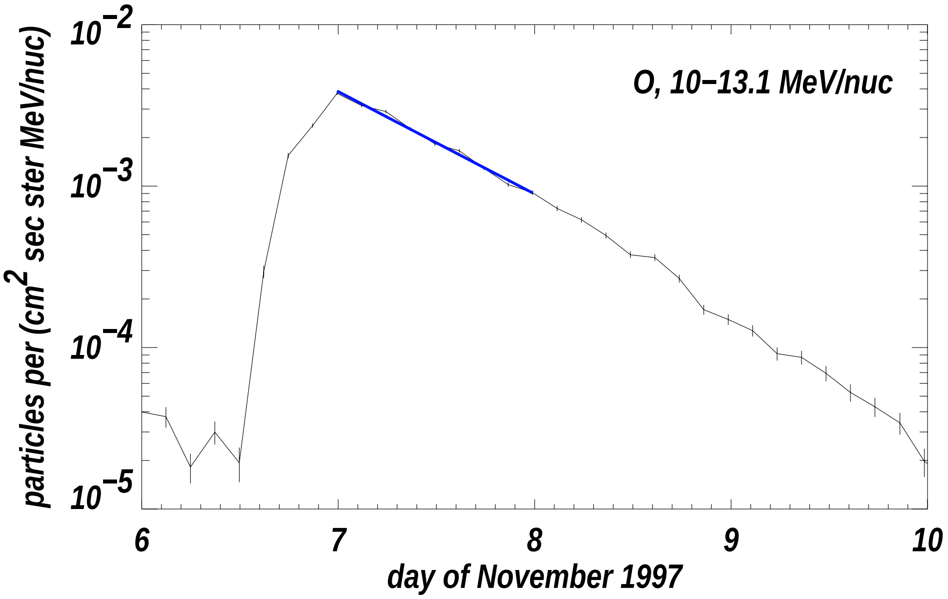

Figure 3.7: Time intensity profile for oxygen at 10-13.1 MeV/nuc in the November 6, 1997 event, with a fit (thick line). The fit is a simple exponential.

the intensity of the particle event; the quantity B is a constant background term which is used only for low flux periods – where two or fewer particles are observed in the three-hour period. The constant offset is not used in higher flux periods: it is smaller than the high fluxes.

Figure 3.7 shows a typical high flux time intensity profile, along with a fit (bold line) which ignores the constant background flux B. The data are for oxygen at $10 - 13.1$ MeV/nuc. The solar particle event in Figure 3.7 started on November 6, 1997, and extended through November 10. One can see in the figure that only the data for November 7 were used in the fit: the period for which the fitting is done is constrained to be the same for all ranges of all the elements used in the fit, in spite of the fact that at higher energies (and rigidities) the decay begins earlier than at lower energies and rigidities. Were this constraint not used, and different fitting periods used for each range of each element, then changing

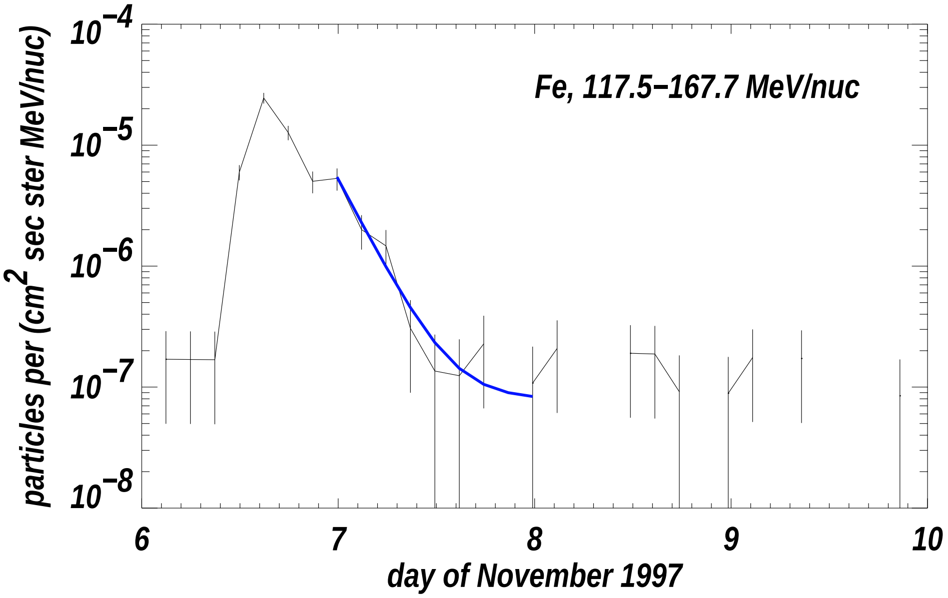

Figure 3.8: Time intensity profile for iron at 117.5-167.7 MeV/nuc in the November 6, 1997, event, with a fit (thick curve). The fit is an exponential with a constant background.

interplanetary conditions might introduce systematic differences in each fit decay timescale. Using the same time period for all fits ensures that the same interplanetary conditions are present for all of the decay timescales fit, even though it might limit the fitting region.

Figure 3.8 shows a low flux time intensity profile, this time for iron at $117.5 - 167.7$ MeV/nuc, in the same event as in Figure 3.7. The same period of data is used for the fit (bold curve). At late times on November 7, it can be seen that the iron flux is tending to a constant background, which warrants the use of the constant term B in the fit to Equation (3.11). Note that the decay begins on November 6 for this energy range of iron, where in Figure 3.7, it can be seen that the decay started on November 7.

The question remains as to exactly what kind of machinery to use to find the maximum likelihood. Obviously, one does not use a linear regression. Instead, the routine that seems most reliable is the amoeba routine, which is described in Press *et al.* (1992). The amoeba is a standard function in the IDL programming environment, which was the environment used for this work. An amoeba procedure is a simplex search through parameter space, essentially guessing at minima in the parameter space until the true minimum is found.

Another of the complications that arises in using maximum likelihood fitting and Poisson statistics is in the calculation of uncertainties for the fit parameters. When one uses Gaussian statistics, the same programming packages that do the fitting generally find uncertainties as well. There is no special coding to be done. Unfortunately, the standard machinery of data analysis that is available with normal statistics is generally not as available when one wishes to use Poisson statistics.

When faced with up to eight ranges of up to thirteen elements, one has to find a way to calculate statistical uncertainties that is not computationally intensive. The method selected for the decay phase fitting depends on how many parameters are being fitted – in other words, whether the fit is for high intensities (two parameters, A and τ) or for low intensities (three parameters, A, τ, and B).

For fits to high flux time intensity profiles, the method chosen is described graphically in figure 3.9. The axes are labelled "Fit Variable X" and "Fit Variable Y"; the space is two-dimensional. Which variables are which is not really important for the purpose of illustrating the technique. The point at the origin in Figure 3.9 is the point of maximum likelihood L_{max}. The ellipse is the contour that corresponds to a likelihood $L = L_{max} - 1/2$. This represents a 1-σ confidence interval (Press *et al.*, 1992). In order to find the uncertainty for fit variable X, a grid of points is laid out in the parameter space, and likelihoods calculated. The uncertainties are taken from the two points that have the maximum deviation from the origin within the ellipse in fit variable X. In Figure 3.9,these points are shown in bold, just as the point of maximum likelihood (at the origin). As can be seen in the figure, this

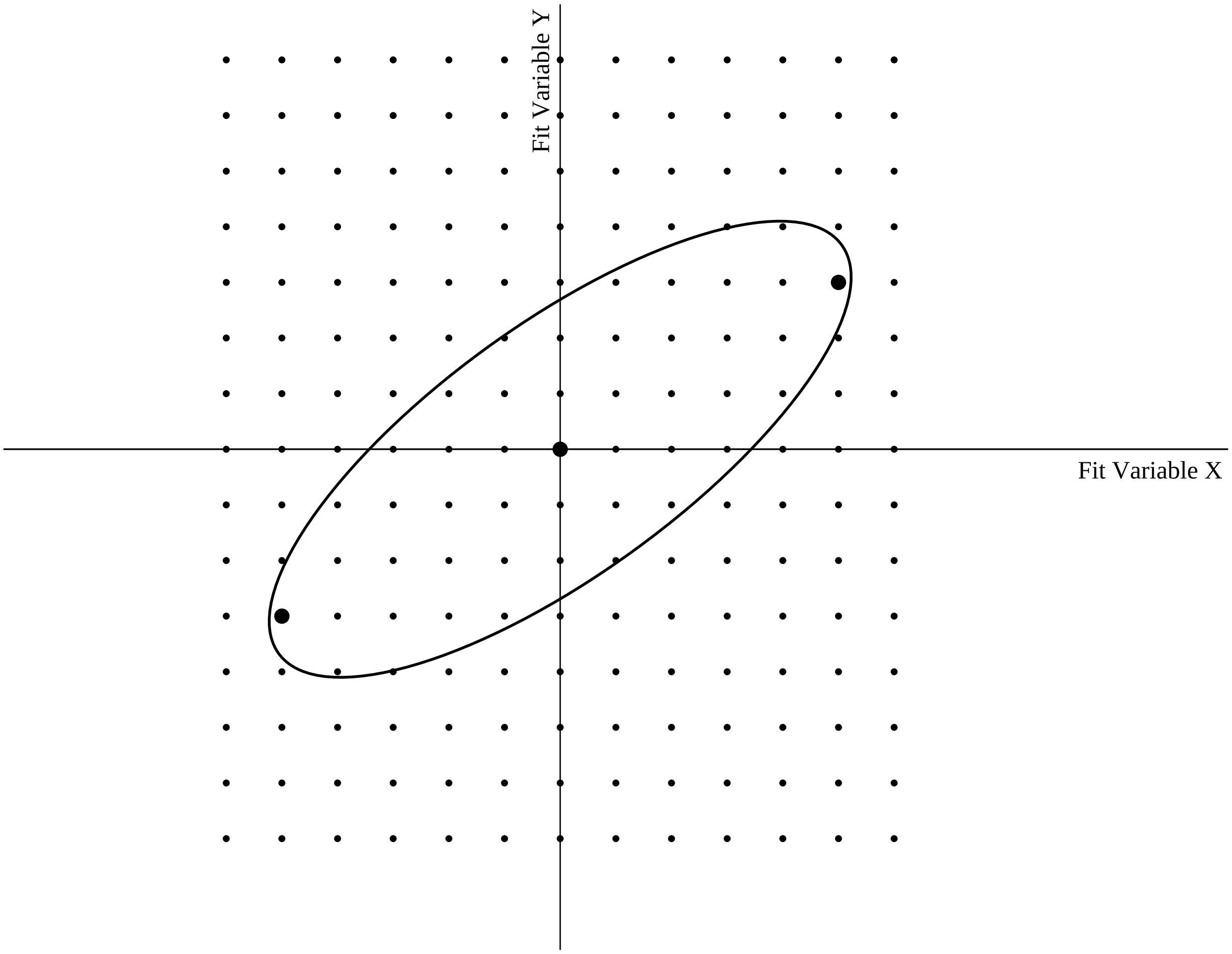

Figure 3.9: Illustration of the method for finding statistical uncertainties with maximum likelihood estimation for two-parameter fits.

will tend to slightly underestimate the uncertainties. However, the grid used is 100 by 100, yielding 10,000 points. If the ellipse does not contain at least 2000 of these points, the grid is re-sized accordingly, and new likelihoods calculated for each of the new points. With 2000 points inside the ellipse, uncertainties estimated should be accurate to within 2%.

In the low intensity fits, there is a three-dimensional parameter space. The grid method discussed above would result in a very intensive calculation – there would be one million points at which to calculate likelihoods. Instead, each fit parameter is treated separately. Figure 3.10 shows the technique. For each fit parameter, a one-dimensional grid of points

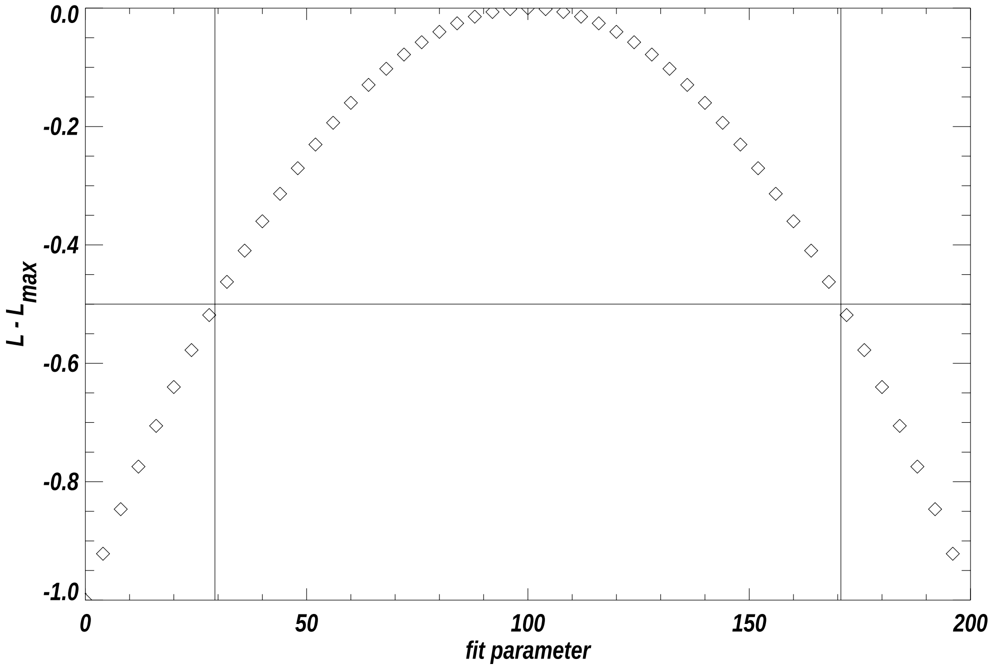

Figure 3.10: Illustration of the method for finding statistical uncertainties with maximum likelihood estimation for three-parameter fits.

is specified that contains the point of maximum likelihood. For each point, the likelihood is minimized with an amoeba, just as is done in the regular fit. However, the parameter whose uncertainty is sought is held fixed to be the value on the grid point. This produces a curve in likelihood versus parameter that looks somewhat parabolic. The horizontal line in Figure 3.10 is at $L_{max} - 1/2$; the vertical lines would be the exact places in the parameter space where $L_{max} - 1/2$ would be seen. In practice, though, this is a finite element grid, and as in the two-parameter method above, the uncertainties will be underestimated slightly. The grid spacing cannot be known *a priori*, just as with the two-parameter method. One hundred grid points are used. Once likelihoods have been calculated for a grid, it is determined how many points lie inside the vertical lines. If that number is less than ninety, the grid is re-sized accordingly, and the calculation redone. With ninety points inside the parabola, the uncertainties estimated should be accurate to within about 1%.

In the case of the ULEIS data, instrument livetimes and geometry factors are not available. This means that sophisticated analysis of the sort described above cannot be done for these data. Instead, a standard weighted linear regression fitting was used for the natural log of the flux during the decay phase. Error analysis was performed in the standard way.

3.5.2 Separating the wheat from the chaff

In Chapter 2, it was discussed how the Parker equation could be solved to examine the behavior of the decay timescale with the diffusion coefficient or rigidity. One of the very important assumptions in the solutions discussed was that the various parameters of the event, such as the solar wind speed, the diffusion coefficient, and the boundary size all remained constant over the period of interest. Under these assumptions, one could expect a very orderly exponential decay after a sharp rise in intensity, and that the slope of the decay would depend on the particle population's average rigidity. However, the space environment is highly dynamic. The reality is that the solar wind speed can change very rapidly, as can the magnetic field strength and direction. Large fluctuations in these quantities will tend to make void the assumptions that led to the solutions of the Parker equation in Chapter 2. The task, then, will be to find a period during which the various parameters of the space environment are reasonably stationary, and an exponential decay can be observed.

Figure 3.11 is a synopsis plot for the various quantities that are considered when finding an equilibrium decay period. Each of the panels in the plot plays a role in finding the equilibrium decay phase of a solar event. Though each subsequent plot deals with only one phenomenon in a solar particle event, all of these phenomena are occuring simultaneously. Figure 3.11 is particularly useful for looking at how the interplanetary environment might

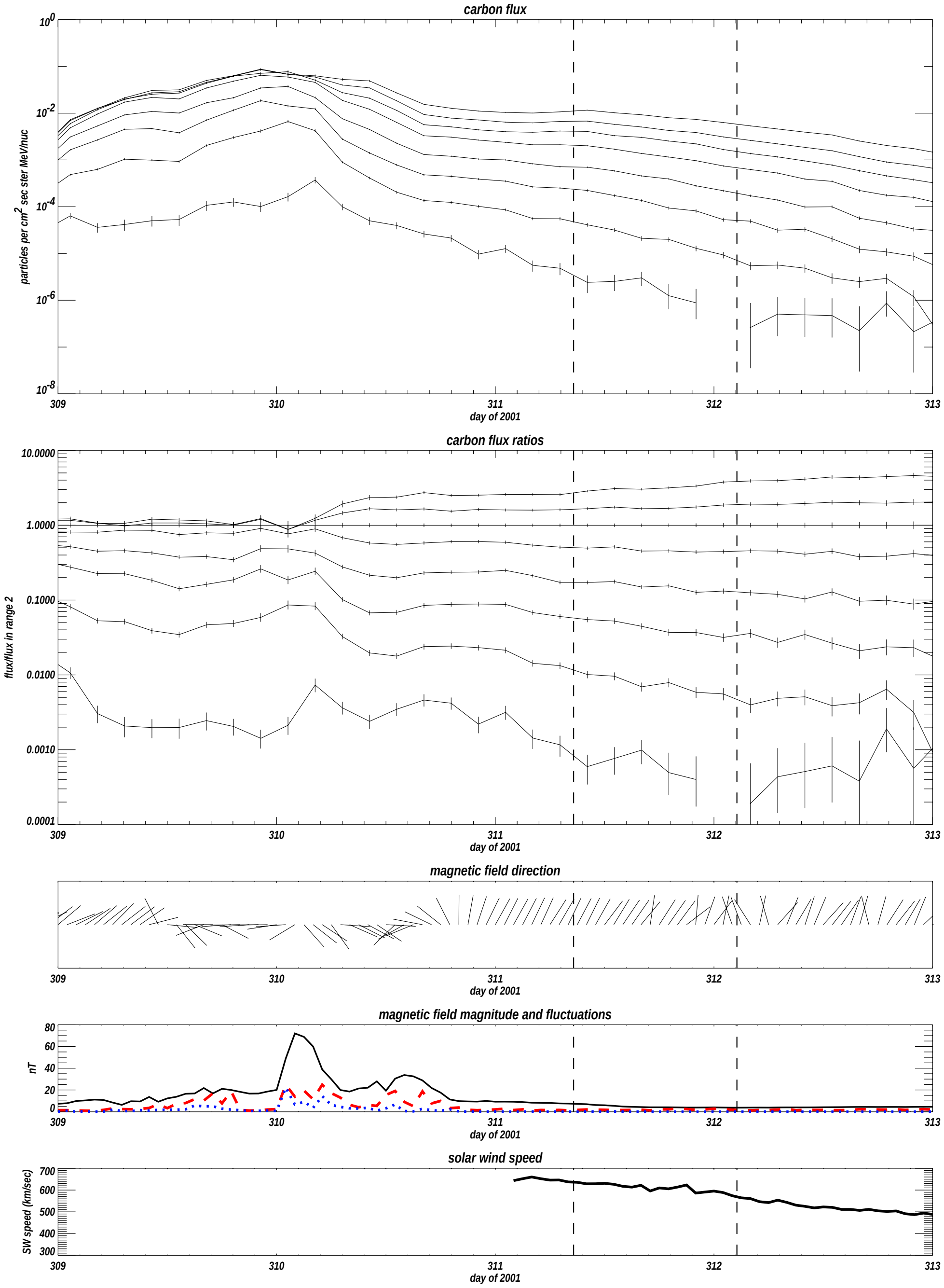

Figure 3.11: Synopsis plot for the November 4, 2001, solar event. Five panels show different quantities considered in the selection of the period of interest. Panel (a) shows time-intensity profiles of carbon at eight different energies in SIS. Panel (b) shows ratios of the various fluxes in (a) with the flux at 12 MeV/nuc. Panel (c) shows the magnetic field direction in a graphical form. Panel (d) shows properties of the interplanetary magnetic field, including its field strength. Panel (e) shows the solar wind speed. The dashed vertical lines through all of the panels denote the start and end of the period of interest. Each panel is reproduced and discussed in subsequent figures.

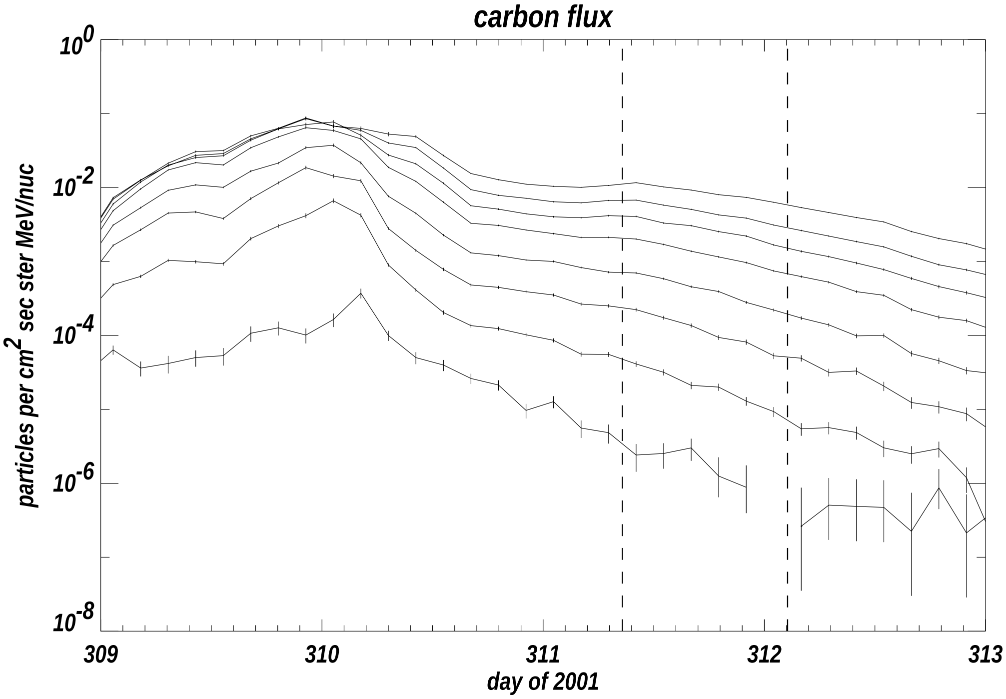

Figure 3.12: Time intensity profiles for the November 4, 2001, event. Eight different energies of carbon in SIS are plotted. The curves are, from the top, for carbon at energies of 6.5, 9.5, 12, 16, 21.5, 29.5, 45, and 66 MeV/nuc.

affect the particle fluxes.

The first step in selecting an event is to look at the time intensity profiles. Figure 3.12 shows time intensity profiles for the eight different energy ranges of carbon measured with the SIS instrument. These profiles are for a solar particle event that occured on November 4, 2001. The highest energy curve has the lowest flux (and is at the bottom). This decay profile is reasonably complicated, and illustrates the issues in finding a period during which the decay is exponential. The peak of the particle intensity occurs at about midnight (UTC) on day 310. Immediately thereafter, there is a complicated decay that is distinctly non-exponential in the period of day 310.0 to 310.8. At this point, several of the lower energy fluxes stop decaying altogether, remaining constant until right after day 311.3, when exponential decay starts. This is, then, the beginning of the period of interest. After about

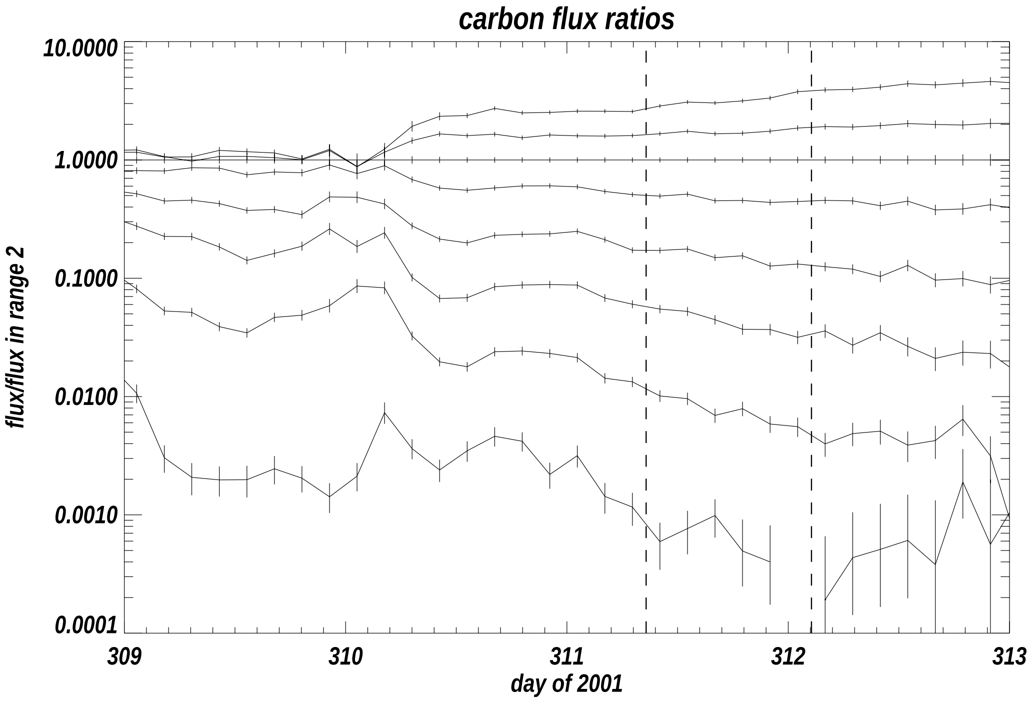

Figure 3.13: Flux ratios for the November 4, 2001, event. For this plot, all of the fluxes from Figure 3.12 have been divided by the flux at 12 MeV/nuc. Energy-dependent decay timescales in Figure 3.12 will appear here as diverging flux ratios. The flux ratio at 12 MeV/nuc is identically 1.

day 312.1, fluxes at the higher energies seem to deviate from exponential decay. Although the lower energy fluxes are still exponentially decaying at this time, the behavior of the higher energy fluxes suggests that this is the end of the period of interest.

The effect in Figure 3.12 is very subtle. There is another way to look at the event, as illustrated in Figure 3.13. This figure shows flux ratios of carbon. In this figure, the flux of carbon at the various energies discussed above has been divided by the flux of carbon at 12 MeV/nuc. In the period of interest, defined above to be the period of day 311.3 to day 312.1, it can be clearly seen that at energies lower than 12 MeV/nuc (the two higher curves), the ratio is increasing with time, but at energies higher than 12 MeV/nuc (the lower curves), the flux ratios decrease with time. This is exactly what one would expect for decay timescales that depend on energy as described by Equation (2.31). One cannot determine periods of interest with flux ratios alone: it can be seen in Figure 3.13 that during day 309, the flux ratios diverge in a way similar to that in the period of interest. This is during the rise time of the event. However, it is evident from Figures 3.12 and 3.13 that looking at flux ratios can be an easier way to spot energy-dependent decay timescales than looking at the event profiles themselves.

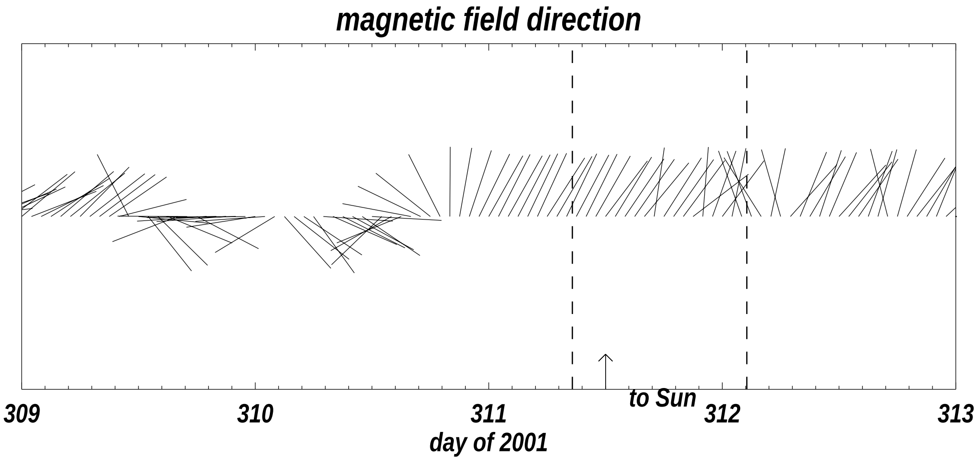

Figure 3.14: Magnetic field longitudinal direction for the November 4, 2001 event. The field direction at a given time is shown by a line segment that originates at $y = 0$ at that time, and points into the direction of the field. In this plot, the Sun is straight up.

Figure 3.14 shows a graphical representation of the longitudinal magnetic field directions during the November 4, 2001 event as recorded by the ACE magnetic fields experiment instrument (MAG) (Smith *et al.*, 1998). The data plotted are Level 2 data that are available to the public on the World Wide Web. In the figure, the longitudinal field direction is graphically represented by a line segment that starts at $y = 0$ at a given time on the x axis. The direction in which the line segment points (away from the point of origin for the segment) is the field direction. For reference, the Sun would be located straight up in the figure for each time on the x axis. For a Parker spiral field, the nominal field direction would be either 45 degrees (clockwise) from the top, or 215 degrees from the top, depending on whether the magnetic polarity is positive or negative. One can see that in the period of interest in this event, the field is mostly lined up with the nominal angles of a Parker spiral, though it is somewhat more radial. Earlier, in days 309 and 310, the field is varying rapidly, and is frequently in a quite different direction. This period corresponds to the period of rise, rapid fall, and flattening of the particle fluxes. In other words, a simple exponential decay does not occur in these days.

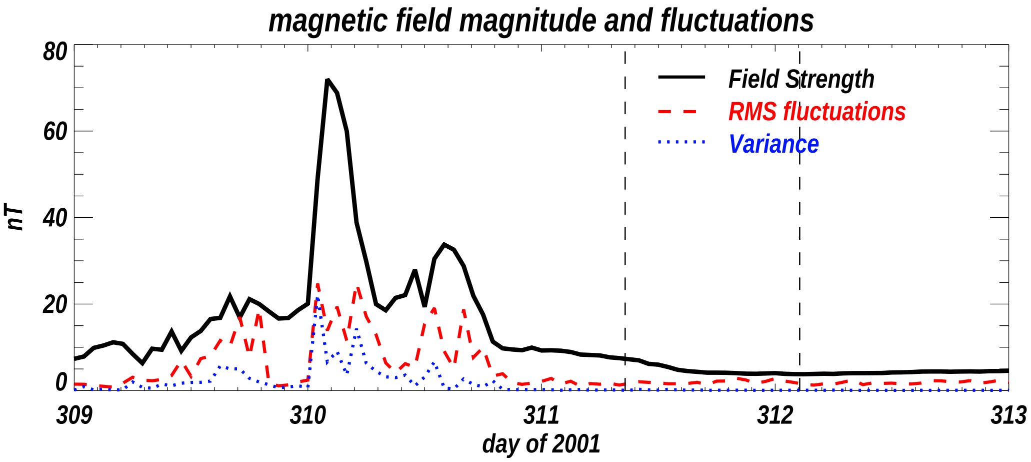

Figure 3.15: Interplanetary magnetic field conditions during the November 4, 2001 event. Magnetic field intensity $|B|$ (solid line), variance of the field, $[<|B^2|> - <|B|>^2]^{1/2}$ (dashed line), and the RMS variation of the high time resolution measurements (dotted line), in nT.

Not only the direction, but the intensity of the interplanetary magnetic field and the magnitude of its fluctuations, can indicate whether a given flux decay will occur in conditions appropriate to the solutions in Chapter 2. Figure 3.15 shows the magnetic field intensity, the variance, and the RMS variation of the high time resolution measurements during hte November 4, 2001 event. During the period of interest, the field is at about 5 nT, which is a typical value (Parks, 1991). The blue and red curves show that the field is also relatively quiet. Earlier, in the same period in which the field direction is changing so much, the field strength is higher and changing, and the field seems overall a great deal more active.

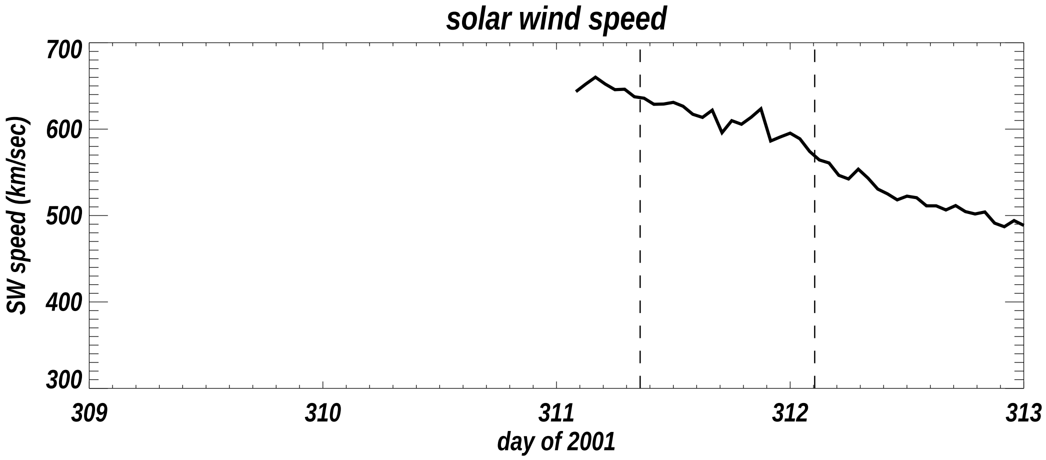

Figure 3.16: Solar wind speed during the November 4, 2001 event. There were no data from the SWEPAM instrument until after day 311 of 2001. During the period of interest, the solar wind speed decreases from ~650 km/sec to ~550 km/sec.

Another important quantity to examine is the solar wind speed. Figure 3.16 shows the solar wind speed for this event. These data are from the Solar Wind Electron Proton Alpha Monitor (SWEPAM) instrument aboard ACE (McComas *et al.*, 1998), which is used to study the solar wind and low energy interplanetary plasmas. Measurements do not exist for the whole event: the high fluxes earlier in the event can affect the SWEPAM algorithm for calculating solar wind speeds. For the period of interest, the solar wind is slowing from about 650 km/sec to 550 km/sec. That the solar wind speed is not perfectly constant should not be a great concern – it is important mostly that there is no discontinuity or shock during the period of interest that affects particles at the higher energies. A changing solar wind speed will have the effect of changing the decay time τ_C from equation (2.17); this effect will contribute to the uncertainty in τ_C.

Figures 3.12 through 3.16, collected as Figure 3.11, give a synopsis of the conditions of and around an exponential decay. Appendix A shows several collections of these plots, one for each of the events used in this analysis. There is also a synopsis plot for an event that does not have an energy dependent decay timescale.

There are a number of reasons that an event might not be suitable for finding charge states. The most common reason is statistics. This analysis requires several energy ranges of several elements with sufficient counts to be statistically significant. Since each element (except for carbon) has its own free parameter α_X, there are a great many free parameters in the fit for the number of data points. Exclusions due to changing magnetic field parameters or solar wind speed are less important. In the selection process, the most important part of the selection process is finding periods of exponential decay. Often, as in the November 2001 event, this will correspond to periods of relative quiescence in the interplanetary medium. Sometimes, as in the November 2000 event (see Appendix A, the exponential decay phase occurs during a period of relatively high activity in the solar wind and interplanetary magnetic field.

Events with soft spectra, or which are iron poor, will not yield many ranges of data, even if the low energy intensity is very high. High flux is also a problem. At very high fluxes, the livetime of the SIS instrument decreases. At high enough fluxes, the livetime fraction can be much less than one percent, resulting in very few particles counted. Notably absent from the events for which charge states are inferred is the Bastille Day event in 2000. This event was extremely large and extremely well studied: see, for example, the many papers in Solar Physics, v.204. In the early part of the decay, the livetime fraction decreases to less than one percent, yielding very few particles counted. In the latter part of the event, the very soft spectrum (power law index of ~ -4) and low relative abundance of heavies (Smith *et al.*, 2001) results in very few particles at the higher energies and higher atomic numbers.

Some events will exhibit exponential decay, but the decay timescale will be constant with energy. One such event is shown in Appendix A, which is the August 15, 2001 event. This event had a decay timescale that was on the order of days. This might indicate a very large boundary L. If the boundary L becomes very large, then the "flat section" of the Forman and Luptons curves (Figure 2.3) becomes wider: since (from Equation (2.17))

$$\tau_C = \frac{r_L}{2CV} \tag{3.12}$$

where V is the solar wind speed, C is the Compton-Getting factor, and r_L is the distance from the Sun of the highest flux region in the equilibrium decay, and the diffusive limit is given by

$$\frac{1}{\tau_D} \sim \frac{L^2}{\kappa} \tag{3.13}$$

then one can see that for a large boundary L the constant convective/cooling decay will dominate over the diffusive portion of the decay. In the August 2001 event, the very long duration of the event ($\sim$ two weeks) would correspond to a boundary four to eight times the size of that in the other events, and the region in energy where τ_C dominates extends through the energies measured in SIS.

Once an event has been selected, the time intensity profiles must be carefully scrutinized for inclusion in the fit to determine the parameters α_X. Various instrumental, statistical, and physical effects may lead various ranges of elements to be excluded, as will be explained below.

One broad exclusion made is for all particles stopping in the SIS matrix detectors, the so-called "range 0" particles. In the current state of the analysis, correct fluxes are not being measured in the high flux periods of solar particle events in range 0. This results in systematic deviations of the decay timescales.

Although Poisson statistics and maximum likelihood fitting are better choices than Gaussian statistics and linear regression at low flux levels, at the lowest flux levels even the maximum likelihood method will give inaccurate results. It can be seen from Monte Carlo simulation of decay phases that at low enough flux levels, one will tend to consistently get fit decay timescales that are longer than the parent timescales. This leads to a criterion for a minimum number of particles in any given three hour bin during a decay. The minimum number, which was determined from a Monte Carlo simulation, depends on the number of three hour bins in the event: fewer particles are required in longer events. For events with only four periods, there must be at least 50 counts in at least one three hour bin during the decay phase. For events with five periods, that number decreases to 40; it is 30 for six periods, 20 for seven periods, and 15 for eight or more periods. One might be tempted to base a criterion on numbers of particles in successive bins. However, this would tend to eliminate the faster decays that occur at higher energies and therefore at lower fluxes.

Sometimes, the solar event itself will yield a range of an element that is not acceptable. A solar particle event is a very complicated system, and the Parker equation is only a very simplified model. Secondary injections and shock effects that cause non-statistical variations from the exponential decay are a common reason to exclude an event, or a range of an element in an event. Figure 3.17 shows an example of such a fluctuation during the November 6, 1997 solar particle event. The element plotted is calcium. It can be seen that at about day 7.5 to 7.6, a small increase occured at many ranges of calcium. At most of those ranges, there was a quick recovery to the previous exponential decay. In the lowest energy range, 15.2-20.3 MeV/nuc, the flux proceeded to decay, but at a higher flux level.

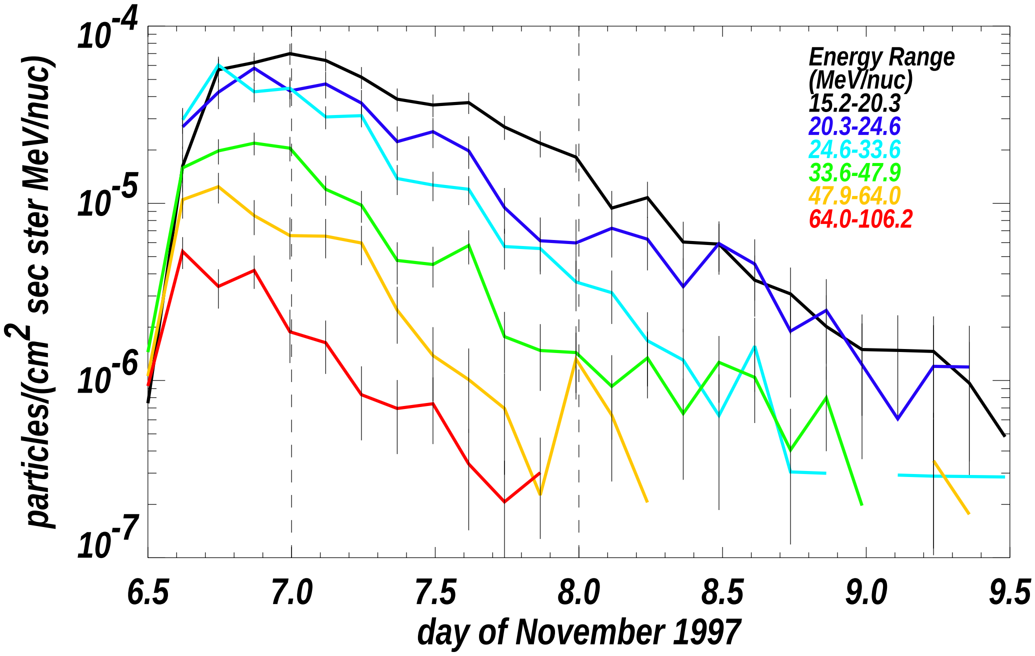

Figure 3.17: Time intensity profiles for calcium at various energy ranges in the November 6, 1997 event. The period used for finding decay lifetimes is between the two vertical dashed lines. There seems to be an increase at about November 7.6 in the lowest four energies of calcium. For calcium at 15.2-20.3 MeV/nuc, this results in an artificial lengthening of the decay timescale. The higher energies seem to be less affected.

This has the effect of artificially lengthening that particular decay timescale.

Complete lists of the time periods of interest and the energy ranges used in SIS and ULEIS in the four events analyzed are in Appendix A.

3.5.3 The Big Bad Amoeba

In Chapter 2 it is seen that the parameterization predicts that for an elemental species, denoted X, the decay rate should depend on that element's energy per nucleon as described in Equation (2.31), which is reproduced here as Equation (3.14):

$$\frac{1}{\tau} = \frac{1}{\tau_C} + W(\alpha_X E)^\gamma. \tag{3.14}$$

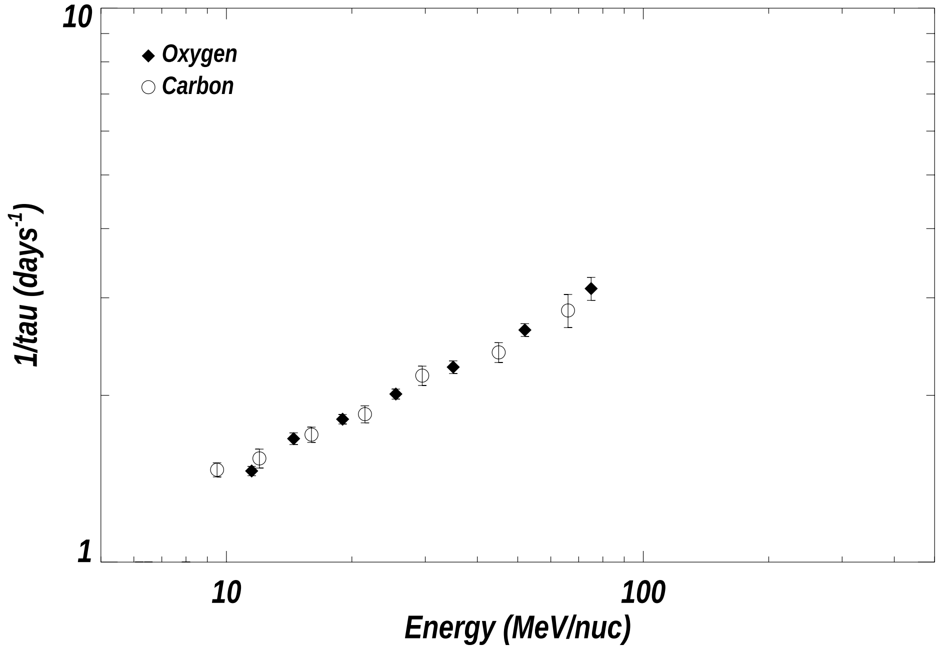

Figure 3.18: Decay rate versus energy (in MeV/nuc) for carbon (open circles) and oxygen (solid diamonds). The data points follow the curve predicted by Equation (2.31). In this plot, oxygen and carbon seem to follow the same curve, indicating that they have the same charge to mass ratio.

Recall that τ_C is the constant term that dominates at low energies; W is an overall normalization that depends on the power spectrum of the turbulence in the interplanetary magnetic field, γ derives from the rigidity dependence of the mean free path, and α_X is related to charge Q_X and mass A_X of the element, as well as the charge Q_C and mass A_C of the reference element, carbon, according to Equation (2.29), which is reproduced as Equation (3.15):

$$\alpha_X \equiv \left[\frac{Q_C}{A_C}\frac{A_X}{Q_X}\right]^{\frac{2\gamma-1}{\gamma}}. \tag{3.15}$$

Figure 3.18 shows a plot of the decay rate, $1/\tau$, versus energy per nucleon for carbon (open circles) and oxygen (solid diamonds). These data are for the November 6, 1997 solar

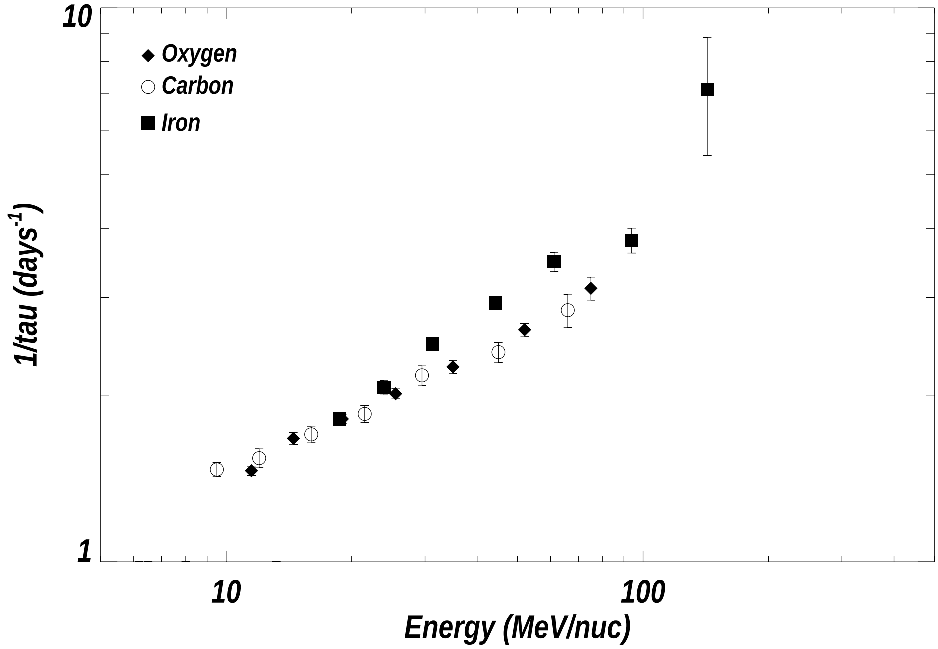

Figure 3.19: Decay rate versus energy (in MeV/nuc) for carbon (open circles), oxygen (solid diamonds) and iron (solid squares) in the November 6, 1997 event. This plot is similar to Figure 3.18, except that iron is included as well. Note that the iron points do not fall on the same track as the carbon and oxygen points. This would indicate that iron has a different charge to mass ratio.

particle event. It is evident that both species follow the same kind of curve, of the sort predicted by Equation (2.31). There are small deviations, owing to the statistics, but the two elements seem to follow the same curve, which would indicate that they have the same charge to mass ratio. At the highest energies plotted, the decay timescale is of order eight hours. At the lowest energies, it is about eighteen to twenty hours.

Figure 3.19 shows a similar plot to Figure 3.18, only now with iron added. Note that the iron points do not lie atop the carbon and oxygen points. It is apparent that iron must have a charge to mass ratio different from those of oxygen and carbon, which are expected to be similar.

Figure 3.20 is similar to Figure 3.19, except that it is for the solar particle event of April

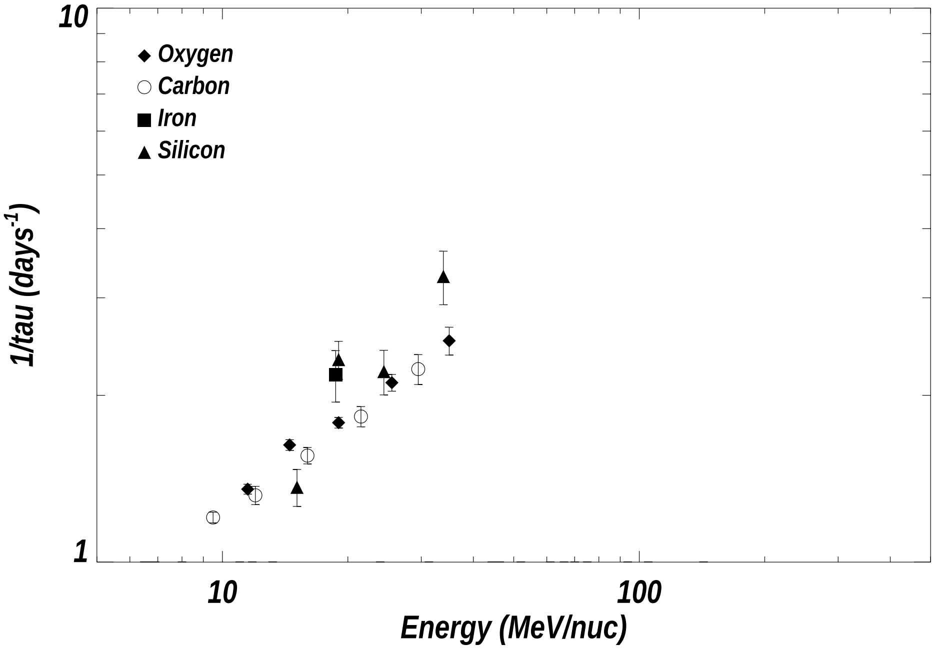

Figure 3.20: Decay rate versus energy (in MeV/nuc) for carbon (open circles), oxygen (solid diamonds), silicon (solid triangles) and iron (solid square), similar to Figure 3.19.

21, 2002. For this plot, carbon, oxygen, iron and silicon are all plotted. There is only a single range of iron that is used in the fitting in this event. One can see that the iron and silicon points do not lie on the same curve as carbon, and that in fact there are differences between carbon and oxygen. There is only one point of iron plotted in this figure: this event was not as rich in heavies as the November 6, 1997 event, and fluxes at high energies were lower. In fact, the November 6, 1997 event was the only event that had high enough statistics for sodium, calcium and nickel.

The parameters of interest in a solar particle event are the constant term of the decay timescale τ_C, the overall normalization W, the power law index of the energy dependence γ, and α_X for each element with sufficient statistics to be included in the fit. In the November 6, 1997 event, there are 11 elements in the fit, including carbon. This gives 10 factors α_X.

There are, therefore, 13 parameters total. In most of the other fits, eight elements are used, giving seven factors α_X. In the April 1998 event, there are only seven elements fit, as iron does not have sufficient statistics.

Equation (3.14) seems like a reasonably simple equation, and one would be tempted to fit it with normal linear regression fitting. However, just as in the discussion of fitting decay times in Section 3.5.1, appearances can be deceiving. The appearance of the constant term $1/\tau_C$ in Equation (3.14) means that one cannot take the log of the equation to obtain a simple expression. More importantly, the treatment of the various factors α_X is somewhat tricky. A given α_X only applies to the data for a single element. In effect, one is making simultaneous fits of between seven and eleven elements: the three overall factors τ_C, γ, and W are constrained to be the same for all elements, while the various α_X are allowed to float freely, but only apply to subsets of data. This requires that the fitting procedure be non-analytical.

Just as in Section 3.5.1, the best analytical tool for this problem will be an amoeba. An amoeba procedure does not require the use of derivatives, being only a simple search through parameter space. It does not require that the function being fit be analytical. Once again, maximum likelihood estimation is used, but this time with normal statistics. From Equation (3.8), one can see that use of the maximum likelihood method with normal statistics leads to the minimization of a χ^2. Here, the $y(x_i; \mathbf{a})$ will be the predictions of $1/\tau$ from Equation (3.14), with a different factor α_X for each element. Unfortunately, the amoeba routine can be somewhat tempermental. It requires as inputs to the procedure first guesses for the values of the parameters to be fit. In Section 3.5.1, such estimates are easy to come by: a linear regression fit works well for the exponential decay part, and the initial guess for the constant is the same for all low flux decays: one particle per three-hour

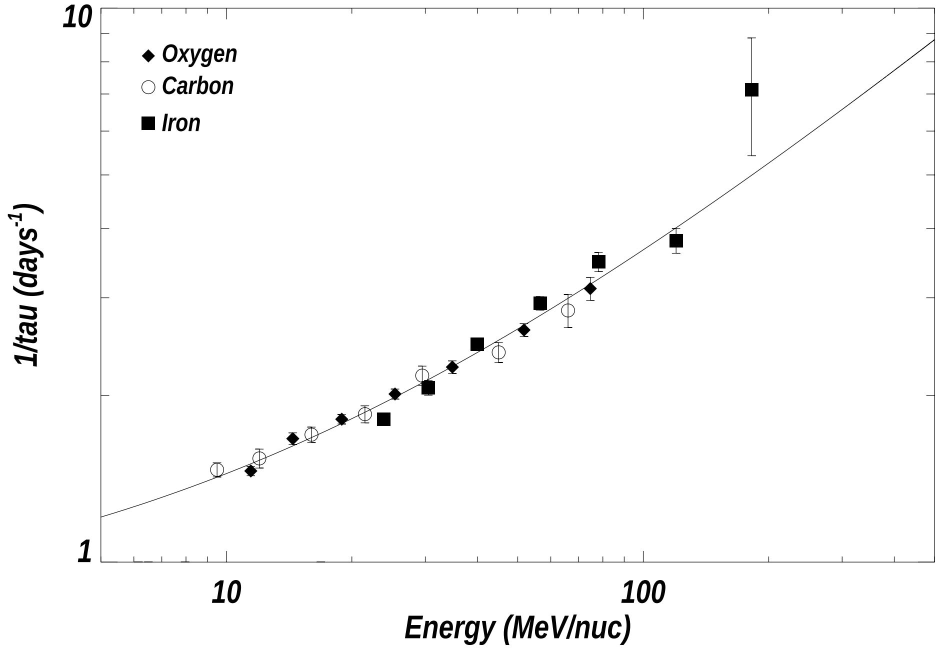

Figure 3.21: Decay rate versus adjusted energy (in MeV/nuc) for carbon (open circles), oxygen (solid diamonds), and iron (solid squares) in the November 6, 1997 event. For this plot, the energies of the various particle species have been adjusted by the factors α_X from the fit to Equation 2.31. The solid curve is determined from the other variables in the fit to Equation 2.31: W, τ_c, and γ.

bin. Here, the situation is quite different. One must make educated guesses about what the fit parameters should be, and then it is often desirable to iterate the amoeba process, using the results of the first amoeba as initial conditions for the next. A fit may be deemed stable when using the fit parameters as initial conditions returns the same results to within a fraction of a percent.

In calculating the uncertainties for this amoeba fit, one is faced with the issue that there are between nine and thirteen fit parameters, depending on how many elements are included in the fit. The uncertainties are calculated in much the same fashion as for the low flux fits in Section 3.5.1: for each fit parameter, a one dimensional grid is specified that includes the fit value of the parameter, and a χ^2 calculated for each grid point. Using an amoeba

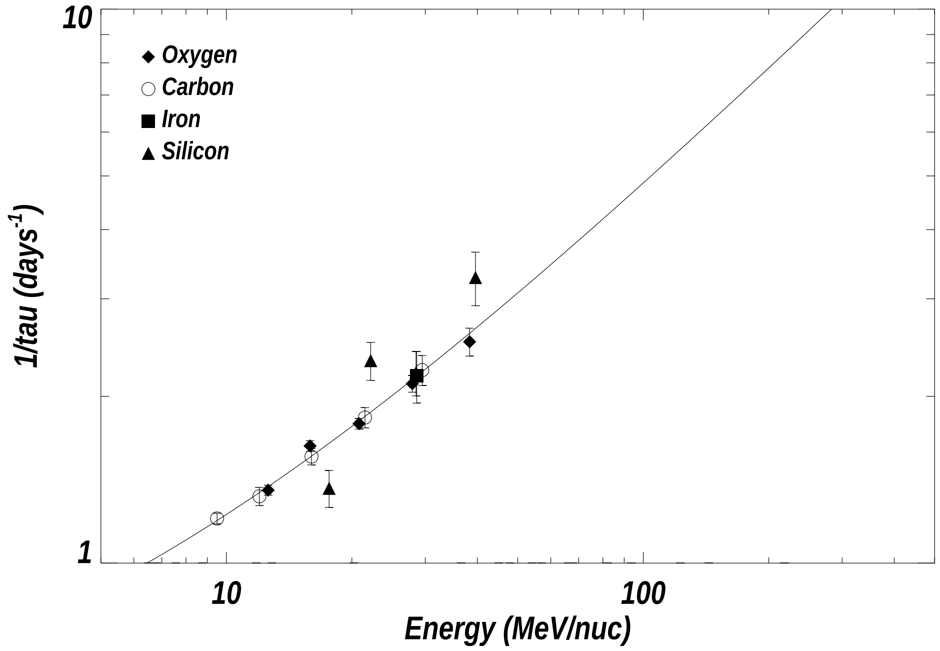

Figure 3.22: Decay rate versus adjusted energy (in MeV/nuc) for carbon (open circles), oxygen (solid diamonds), silicon (solid triangles), and iron (solid square) in the April 21, 2002 event, similar to Figure 3.21.

to minimize the χ^2 for all of the grid points for all of the fit parameters would be far too computationally intensive. This is, however, what is done in finding uncertainties on all of the global parameters: $1/\tau_C$, W and γ. In finding the uncertainties for the various factors α_X, a new χ^2 is calculated for each grid point, holding all other fit parameters fixed. As each α_X only applies to a small subset of the data, the effect of not re-minimizing the χ^2 will be very small.

A 1-σ confidence interval is defined (Press *et al.*, 1992) as the grid point where χ^2 has risen from the minimum value for the fit, χ^2_{min}, to a value of $\chi^2 = \chi^2_{min} + 1$. In Section 3.5.1, the uncertainty is taken to be the points in the grid above and below the fit parameter that have the maximum value of the likelihood within the $L = L_{max} - 1/2$ boundary. The way to minimize the underestimation of the uncertainty is to require that of 100 grid points, 90 fall inside this boundary. Here, the amoeba procedure is so intensive that it is not practical to re-size the grid and recalculate. Instead, an interpolation is made on each side of the fit parameter (each side of the grid) between the point with the largest χ^2 within the 1-σ interval and the point with the lowest χ^2 outside.

The uncertainty in a given α_X does not stem from deviations of the element's data points from the adjusted fit curve. Instead, it arises from the increase in χ^2 as α_X is varied – in other words, from how much the curve may be shifted back and forth and yet keep the system within the $\chi^2_{min} + 1$ boundary.

Figures 3.21 and 3.22 show decay rates versus energy adjusted by α_X for the November 6, 1997 and April 21, 2002 events. These are similar to Figures 3.19 and 3.20. In both of these figures, the solid line is the decay rate versus energy curve as calculated using the global fit parameters τ_C, W, and γ. This also corresponds to the fit for carbon, for which $\alpha_C = 1$ is fixed. All of the other elements have had their energies per nucleon adjusted by the factors α_X so that they fall along the global fit curve.

Of the many (~40) solar particle events that occurred between August 1997 and May 2002, only four are suitable (as discussed in Section 3.5.2) for finding charge states. These four events are those of November 6, 1997, November 25, 2000, November 4, 2001, and April 21, 2002. These events have high fluxes at the higher energies and for the heavier elements. These events also have periods where the particle rate was not so high as to saturate the instrument. One of the highest rate events observed by ACE to date occured on July 14, 2000 – the so-called Bastille Day event. The fluxes in this event were so high that the instrument livetime fraction was well below 1%, and very few particles were counted. High livetime fractions exist late in the decay phase of the event, but owing to the steep particle spectra and low abundances of heavies (Smith *et al.*, 2001), there are not sufficient statistics

Parameter	$97-311$	$00-331$	$01-310$	$02-112$
α_N	$1.001^{+0.069}_{-0.067}$	$0.881^{+0.094}_{-0.105}$	$1.041^{+0.068}_{-0.066}$	$1.008^{+0.041}_{-0.040}$
α_O	$0.995^{+0.024}_{-0.023}$	$1.191^{+0.036}_{-0.048}$	1.095 ± 0.023	1.065 ± 0.014
α_{Ne}	$1.028^{+0.048}_{-0.047}$	$1.231^{+0.140}_{-0.142}$	$1.036^{+0.076}_{-0.075}$	$0.991^{+0.038}_{-0.037}$
α_{Na}	$1.194^{+0.247}_{-0.230}$	$--$	$--$	$--$
α_{Mg}	1.085 ± 0.058	$1.217^{+0.124}_{-0.118}$	$1.129^{+0.069}_{-0.068}$	$1.062^{+0.033}_{-0.032}$
α_{Si}	$1.208^{+0.069}_{-0.068}$	$1.436^{+0.213}_{-0.154}$	$1.168^{+0.090}_{-0.088}$	1.088 ± 0.046
α_S	$1.124^{+0.108}_{-0.104}$	$--$	$1.131^{+0.347}_{-0.320}$	$1.130^{+0.146}_{-0.140}$
α_{Ca}	$1.380^{+0.181}_{-0.173}$	$--$	$--$	$--$
α_{Fe}	$1.277^{+0.036}_{-0.035}$	$--$	$1.530^{+0.279}_{-0.265}$	$1.104^{+0.164}_{-0.157}$
α_{Ni}	$1.177^{+0.155}_{-0.149}$	$--$	$--$	$--$
$1/\tau_c$	$0.771^{+0.098}_{-0.129}$	$0.485^{+0.438}_{-1.343}$	$0.416^{+0.228}_{-0.506}$	$0.756^{+0.119}_{-0.165}$
W	$0.157^{+0.055}_{-0.036}$	$0.266^{+1.059}_{-0.204}$	$0.147^{+0.248}_{-0.075}$	$0.118^{+0.079}_{-0.046}$
γ	$0.633^{+0.054}_{-0.060}$	$0.492^{+0.332}_{-0.274}$	$0.740^{+0.169}_{-0.217}$	$0.632^{+0.107}_{-0.105}$

Table 3.1: Fit parameters for the four events analyzed.

in the heavy elements ($Z \geq 6$) to make the charge state calculation.

For these events, the results of the amoeba fitting are shown in Table 3.1. There are five columns in this table. The first is the name of the parameter sought: $1/\tau_C$, W, γ, and the factors α_X. The values in the second column are fit values for these parameters (along with uncertainties) in the event of day 311 of 1997 (written 97-311) – in other words, the November 6, 1997 event. The choice of day 311 corresponds not to the time of the event onset, but rather the first day in which data from the equilibrium decay are included in the fit. Some of the uncertainties are seen to be asymmetric. Not all elements are used in each fit; for those elements not included in the event fit, a dash is indicated.

Recall that $1/\tau_C$ is the constant offset decay rate that dominates at low energies, γ is the power law index of the energy-dependent portion of the decay rate, W is the overall normalization for the energy-dependent portion of the decay rate, and α_X are the proportionality constants for all of the elements included in the fit for each event. Note that in three of the four events listed, some elements are excluded entirely. In the November 6, 1997 event, eleven elements were fit: carbon, nitrogen, oxygen, neon, sodium, magnesium, silicon, sulfur, calcium, iron, and nickel. In the other events, sodium, calcium and nickel do not have sufficient statistics to be included in the fit. In the 00-331 event, sulphur and iron do not have sufficient statistics to be included in the fit.

Chapter 4

Results: Curious George Does Space Physics

4.1 We've got alphas! Now what?

The most important result from Chapter 3 was the various multiplicative constants α_X and power law indices γ for the various events and elements as given in Table 3.1. Equation (2.30) gives the charge state as a function of α_X and γ for a given particle species in a given event. It is reproduced here as Equation (4.1):

$$Q_X = \alpha_X^{\frac{\gamma}{1-2\gamma}} \frac{Q_C}{A_C} A_X. \tag{4.1}$$

Here, Q_X is the average charge state of the element X, and A_X is its atomic mass; A_C and Q_C are the atomic mass and average charge state of carbon. $Q_C = 5.9$ is assumed in all four of the events: over a wide range of coronal and higher temperatures, carbon is nearly fully stripped.

Table 4.1 gives all the charge states calculated from the various factors α_X listed in Table 3.1, with accompanying uncertainties. For the 00-331 event, the best fit value for γ is very close to 0.5, which would indicate a diffusion coefficient that was independent of rigidity. The uncertainty is quite large, though, and the upper bound on γ has been used to deduce upper limits for the charge states in this event. Uncertainties are not presented for the charge states in this event. For the other events, the uncertainties σ_{Q_X} are calculated from the uncertainties σ_{α_X} in Table 3.1 using standard error propagation with equation (4.1):

$$\sigma_{Q_X}^2 = \sigma_{\alpha_X}^2 \left(\frac{\partial Q_X}{\partial \alpha_X} \right)^2 + \sigma_\gamma^2 \left(\frac{\partial Q_X}{\partial \gamma} \right)^2 \tag{4.2}$$

From Equation (4.1), one can see that the total uncertainty σ_{Q_X} will be given by:

$$\sigma_{Q_X}^2 = \sigma_{\alpha_X}^2 \left[\left(\frac{\gamma}{1-2\gamma} \right) \frac{Q_X}{\alpha_X} \right]^2 + \sigma_\gamma^2 \left[Q_X \frac{\ln(\alpha_X)}{(1-2\gamma)^2} \right]^2 \tag{4.3}$$

The columns in Table 4.1 are similar to those in Table 3.1. The first column is a list of the element names. The second column contains the charge states for all of these elements in the November 6, 1997 event (the beginning of the data analysis period was on day 311 of 1997, which is actually November 7). The next columns are for the other events analyzed. As in Table 3.1, where a charge state (or upper limit) has not been determined, a double dash is indicated.

For some of the elements and events in Table 4.1, the dominant term in the uncertainty σ_{Q_X} will derive from σ_{α_X}. For others, such as iron in the November 1997 event (97-311), the dominant source of uncertainty will be in σ_γ.

4.2 Comparing to other measurements: How did we do?

Among the various solar particle events examined here, the November 6, 1997 event stands out. This event has been examined by many authors, particularly from the point of view

Element	$97-311$	$00-331$	$01-310$	$02-112$
Nitrogen	6.9 ± 1.1	≤ 7.0	6.47 ± 0.68	$6.75\ ^{+\ 0.66}_{-\ 0.65}$
Oxygen	$7.95\ ^{+\ 0.46}_{-\ 0.44}$	≤ 6.3	$6.83\ ^{+\ 0.51}_{-\ 0.62}$	$6.76\ ^{+\ 0.69}_{-\ 0.68}$
Neon	9.3 ± 1.0	≤ 7.6	9.4 ± 1.1	$10.13\ ^{+\ 0.94}_{-\ 0.92}$
Sodium	$7.4\ ^{+\ 3.8}_{-\ 3.6}$	$--$	$--$	$--$
Magnesium	9.8 ± 1.4	≤ 9.3	$9.9\ ^{+\ 1.3}_{-\ 1.5}$	10.3 ± 1.2
Silicon	$8.8\ ^{+\ 1.7}_{-\ 1.8}$	≤ 8.7	$10.9\ ^{+\ 1.8}_{-\ 2.0}$	$11.3\ ^{+\ 1.9}_{-\ 1.8}$
Sulfur	11.9 ± 2.9	$--$	$13.0\ ^{+\ 6.3}_{-\ 5.9}$	$11.8\ ^{+\ 4.3}_{-\ 4.1}$
Calcium	$9.1\ ^{+\ 3.6}_{-\ 3.7}$	$--$	$--$	$--$
Iron	$15.3\ ^{+\ 3.0}_{-\ 3.3}$	$--$	$14.2\ ^{+\ 6.0}_{-\ 6.9}$	$21.6\ ^{+\ 8.4}_{-\ 8.0}$
Nickel	$19.6\ ^{+\ 6.6}_{-\ 6.5}$	$--$	$--$	$--$

Table 4.1: Charge States inferred for the various events analyzed based on the fit parameters in Table 3.1.

of SEP charge states. At energies comparable to those observed in SIS, charge states have been determined in this event by the geomagnetic cutoff technique on SAMPEX (Mazur *et al.*, 1999; Leske *et al.*, 2001), from Q/M fractionation (Cohen *et al.*, 1999) and from examination of the time to maximum flux (Dietrich & Lopate, 1999). At lower energies, charge state distributions were measured directly with the Solar Energetic Particle Ionic Charge Analyzer (SEPICA) aboard ACE (Möbius *et al.*, 1999, 2000; Popecki *et al.*, 2000a,b; Klecker *et al.*, 2000), and with SAMPEX using the geomagnetic cutoff technique (Mazur *et al.*, 1999). Comparison here is made with other measurements at energies comparable to those observed with SIS. The lower energy measurements show evidence for an energy dependence which will be discussed in Section 4.4.

Other solar events are not as well studied as the November 6, 1997 event. For the other events studied here, the only other high-energy measurements of charge state are those of Labrador *et al.* (2003). The work of Cohen *et al.* (1999) and Dietrich & Lopate (1999) has not been repeated for later events. The high voltage on the SEPICA instrument failed before the November 2000 event. Charge state measurements from SEPICA are not

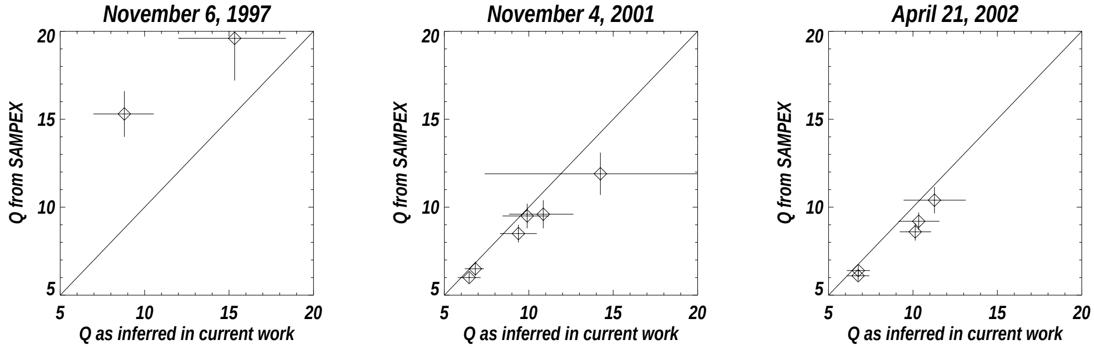

Figure 4.1: Comparison between SAMPEX measurements of charge states by Mazur *et al.* (1999) and the current work.

available for this or later events.

Figure 4.1 shows comparisons between the work presented here and charge states at high energies derived from SAMPEX using the geomagnetic cutoff technique for the November 6, 1997 event (left panel), the November 4, 2001 event (middle panel) and the April 21, 2002 event (right panel). The SAMPEX data are from Mazur *et al.* (1999) and Labrador *et al.* (2003). During the events in 2001 and 2002, it can be seen that the charge states measured with SAMPEX are consistent with those inferred here, even if somewhat lower. In the 1997 event, however, the SAMPEX measurements are systematically higher than those here. Clearly, there is some systematic problem in one of the measurement techniques that causes this discrepancy. The measurement of Mazur *et al.* (1999) for the silicon charge state in the November 1997 event is 15.3±1.3. Given that fully stripped silicon has a charge state of 14, it may be that the systematic problem might lie with the determination of the geomagnetic cutoff or elsewhere in the SAMPEX result.

Figure 4.2 shows a comparison between charge states inferred using abundances (Cohen *et al.*, 1999) and the current work. This comparison is only for the November 6, 1997 event. It can be seen that for almost all elements, the charge states inferred by the two methods

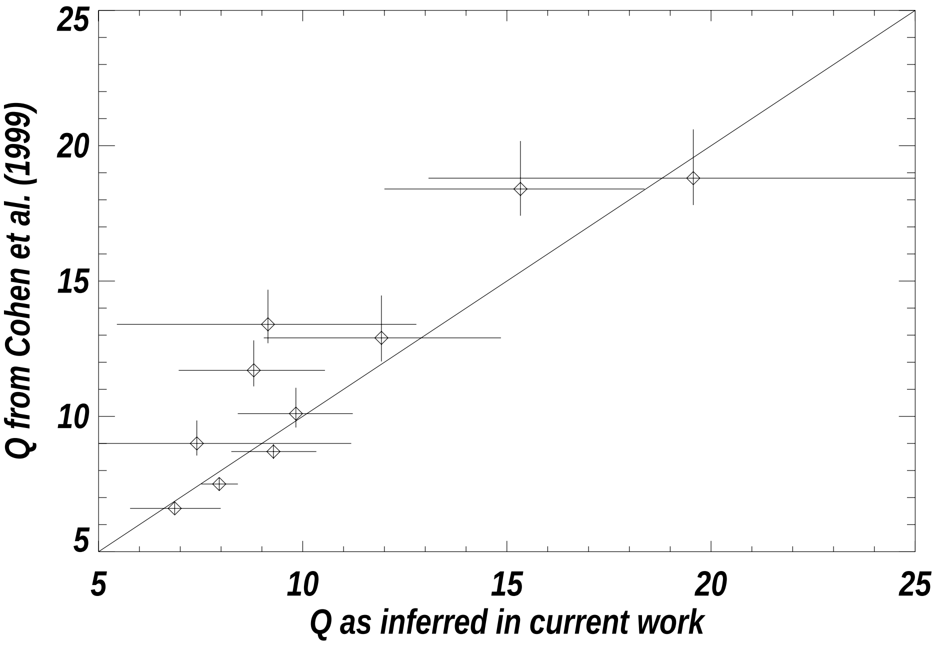

Figure 4.2: Comparison between charge states inferred from abundances (Cohen *et al.*, 1999) and the current work.

are consistent.

The method of Cohen *et al.* (1999) was to examine the different ways in which solar particles might be fractionated in their journey from the solar surface to the corona and into interplanetary space as SEPs. It was observed by Breneman & Stone (1985) that the abundances $R_{SEP}(Z)$ of elements in a solar particle event relative to mean averages R_{ph} in the photosphere could be organized as a power law in Q/M:

$$\frac{R_{SEP}(Z)}{R_{ph}(Z)} = \frac{F(Z)}{F(Z_0)} \left[\frac{Q(Z)}{M(Z)} \frac{M(Z_0)}{Q(Z_0)}\right]^{\gamma}. \tag{4.4}$$

In Equation (4.4), Z_0 is the atomic number of a reference element, carbon; Z is the atomic number of the element whose charge state is sought; and F is the enhancement factor due to fractionation (due to the first ionization potential, or FIP) at the solar surface

(Cook, Stone & Vogt, 1984).

Solar energetic particle abundances R_{SEP} of elements were compared with photospheric values R_{ph} from Grevesse, Noels & Sauval (1996). Charge states were determined by solving Equation (4.4) for the charge state $Q(Z)$:

$$Q(Z) = Q(Z_0)\frac{M(Z)}{M(Z_0)}\left[\frac{F(Z_0)}{F(Z)}\frac{R_{SEP}}{R_{ph}}\right]^{\frac{1}{\gamma}}. \tag{4.5}$$

The power law index γ is found from Q/M fractionation within the isotopes of magnesium. It is assumed in this process that γ, which is derived from a limited range of Q/M, applies equally well to all elements, even those which might have a substantially different Q/M, such as iron. Carbon is assumed to have a charge state of 5.9±0.1. The function $F(Z)$ is taken to be a quasi-step function with values of s for $FIP < 10$eV, 1 for $FIP > 11$eV, and $(s+1)/2$ for $FIP = 10.2$ (for sulfur). The uncertainties in Figure 4.2 are larger than those originally given in Cohen *et al.* (1999): these uncertainties were determined by adding in quadrature (as in Equation (4.2)) the uncertainties due to the abundances R_{SEP}, the assumed charge state $Q(Z_0)$ of carbon, s, γ and the uncertainties in R_{ph} from Grevesse, Noels & Sauval (1996). The original uncertainties in Cohen *et al.* (1999) were derived the same way, but only accounting for the uncertainties in R_{SEP} and R_{ph}.

Another method to find charge states, called the time-to-maximum (or TTM) method, was explored by Dietrich & Lopate (1999). These authors postulated that for a given particle rigidity R, the time delay τ_{TTM} between the event onset for particles of that rigidity and the point of maximum flux in the event for that population depended on R in the following manner:

$$\tau_{TTM} = aR^b \tag{4.6}$$

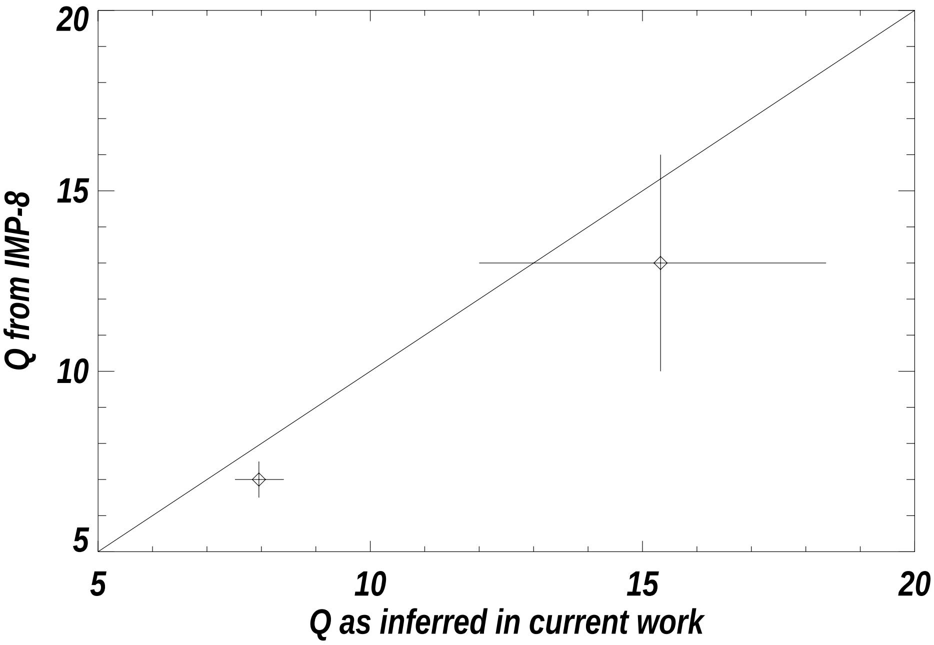

Figure 4.3: Comparison between charge states inferred by the TTM method with IMP-8 (Dietrich & Lopate, 1999) and the current work. The energy range for the IMP-8 iron result is ∼20-400 MeV/nuc.

where the quantities a and b are constants. Average charge states were found in a manner similar to the one here, applying equation (4.6) to τ_{TTM} versus particle energy E profiles and finding the correct rigidities by varying Q/M so as to minimize a χ^2.

Figure 4.3 shows a comparison between the charge states derived from IMP-8 data using the TTM method and the current work. The latest event analyzed in the IMP-8 work was the November 6, 1997 event, for which charge states for only oxygen and iron were quoted. The IMP-8 charge states for these elements are both lower than the work here, though the iron point is statistically consistent (within one σ) of the current result. The IMP-8 oxygen point is about two deviations away from the current result for oxygen.

The problem with this method is that it is not based on any particular physical model. In the subsequent work of Dietrich & Tylka (2001) it was argued that the time to maximum was proportional to $1/\beta R^{1/3}$, which would be consistent with a timescale to fill a diffusive cavity that was proportional to L^2/κ. By comparison, the decay timescales in this event here are found to be proportional to $1/\beta R^{0.28}$. It may prove worthwhile to re-analyze the data of Dietrich & Lopate (1999) using this more physical velocity-rigidity dependence, instead of the original rigidity dependence.

4.3 It's a hot time in the old Sun tonight

In Chapter 1 it was discussed how, using the results of Arnaud & Rothenflug (1985) and Arnaud & Raymond (1992), charge states might be used as a thermometer for the source plasma of solar energetic particles. The idea is simple: the tabulated results of Arnaud & Rothenflug (1985) and Arnaud & Raymond (1992) are treated as a model, and a χ^2 is calculated for the calculations versus the inferred charge states. The temperature fit in this manner is the one for which this χ^2 is the minimum value χ^2_{min}. The uncertainty in the fit temperature derives from the points where $\chi^2 = \chi^2_{min} + 1$ is true, just as was done with the fitting in Chapter 3.

The issue with this method is the grid spacing of the theoretical calculations. Charge states are calculated by Arnaud & Rothenflug (1985) and Arnaud & Raymond (1992) for each 0.1 dex in temperature, e.g., at log(Temperature)=6.0,6.1,6.2... In order to increase the precision of the uncertainty estimation, an interpolation was made: a spline was fit to the average charge states derived from the theoretical calculations at increments of 0.01 in dex, resulting in more grid points. In fitting this spline, it was assumed that increasing the resolution of the theoretical calculations would not result in large deviations from the original (coarser) shape.

Figure 4.4 shows inferred charge states for the November 6, 1997 solar particle event,

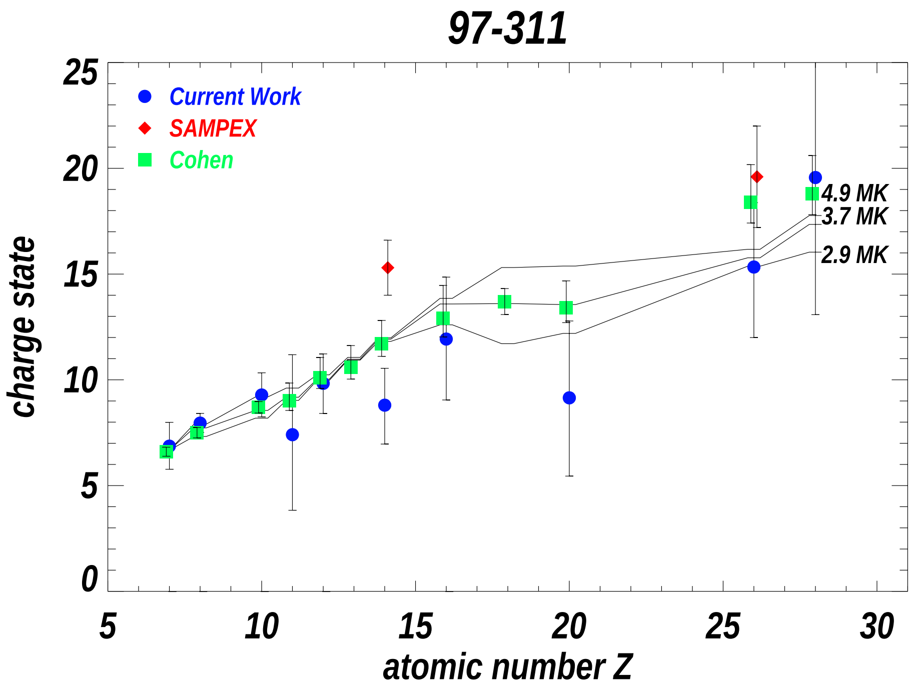

Figure 4.4: Charge states in the November 6, 1997 solar particle event. Disks are the current result. The charge state for carbon is for energies of 8.6-76.3 MeV/nuc; for iron, the charge state is for energies of 15.8-167.7 MeV/nuc. Diamonds are the results from Mazur *et al.* (1999); squares are the Cohen *et al.* (1999) results. For this plot, all of the different charge states have been offset from each other in Z to better show the error bars. The black lines are charge states corresponding to the best fit temperature and the 1-σ limits from the Arnaud & Rothenflug (1985) and Arnaud & Raymond (1992) calculations. These curves should be discontinuous steps at each value of Z, but are presented in this manner to better guide the eye. They are labelled with their corresponding temperatures in MK.

along with the best fit temperature, and the temperatures corresponding to the 1-σ confidence intervals. It is seen that almost all of the points are within one σ of the best fit temperature, with the exception of silicon. Also shown on the plot are the two high energy points from SAMPEX for this event from Mazur *et al.* (1999) and the charge states inferred for this event by Cohen *et al.* (1999).

It can be seen that the theoretical charge states of silicon do not change significantly over the range of temperatures within the 1-σ confidence interval. The best fit temperature is 3.7 MK; with a possible range from 2.9 MK to 4.9 MK. At these temperatures, the theoretical charge state of carbon is 5.99, very close to (within 0.1 charge units) the charge state assumed. If this value of Q_C were used in the determination of the other charge states, the deduced charge states Q_X would increase by about 1.5 %, which is small compared with the uncertainties in Table 4.1. This best fit temperature would seem to indicate that the source plasma for this event is hotter than the corona.

The SAMPEX points are much higher than the current results and are not consistent with the fit temperature. Recall that the charge state reported in Mazur *et al.* (1999) is 15.3; it may well be that the charge states reported by Mazur *et al.* (1999) at high energies are systematically high.

Of the charge states from Cohen *et al.* (1999), all but iron and nickel seem consistent with the best fit temperature. Iron and nickel seem to be indicative of a temperature closer to 8-10 MK, though only iron is further than 2σ from the best fit temperature. The silicon charge state, while not consistent with the current measurement, is nonetheless consistent with the best fit temperature. The error bars shown for the Cohen *et al.* (1999) points are different from the original numbers as was discussed in Section 4.2.

Figure 4.5 shows inferred upper limits for charge states in the November 2000 solar particle event. There are no SAMPEX measurements against which to compare for this event. For this event, there is no true "best fit" temperature, as there are no true best fit charge states. As shown in Table 3.1, the best fit value for γ is ~ 0.5. This would correspond to diffusion independent of the charge state; the charge states for this value of γ would be all identically zero. In order to find an upper limit for the charge states, the upper 1-σ limit of γ was used in equation 4.1 along with the best fit values of α_X. An upper limit temperature was found from the best fit temperature for these upper limits of the charge states. In this fitting, the upper limit for the temperature is 1.4 MK. This upper limit is

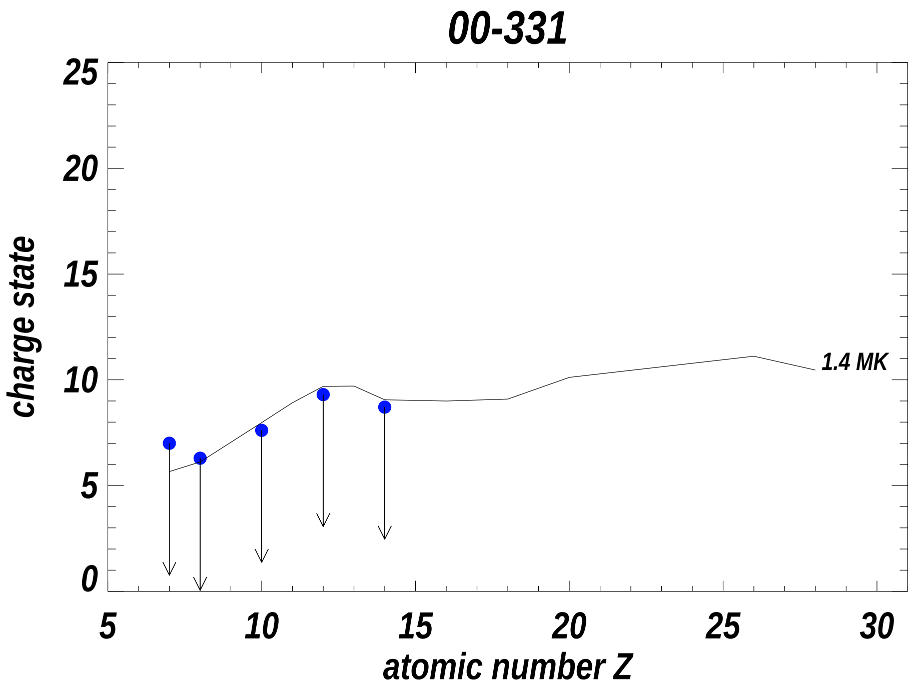

Figure 4.5: Upper limits for charge states in the November 2000 solar particle event. The charge states corresponding to the best fit upper limit temperature (from Arnaud & Rothenflug (1985) are also shown. The best fit upper limit temperature is 1.4 MK.

consistent with typical corona temperatures, and would imply that SEPs in this event were accelerated out of a coronal source plasma.

Figure 4.6 shows inferred charge states for the November 4, 2001 solar particle event, similar to Figure 4.4. The best fit temperature is 2.3 MK, with limits at 1.8 MK and 2.9 MK. It can be seen that the SAMPEX measurements for this event are completely consistent with the current work, and are also consistent with the best fit temperature of 2.3 MK, though they might be more indicative of a lower temperature of 1.8 MK. The best fit temperature is consistent with acceleration from a source plasma in the corona. It should be noted that the largest contribution to χ^2 comes from the oxygen point. In effect, the oxygen charge state dominates the temperature determination, though the other elements all have charge states that are consistent with this temperature.

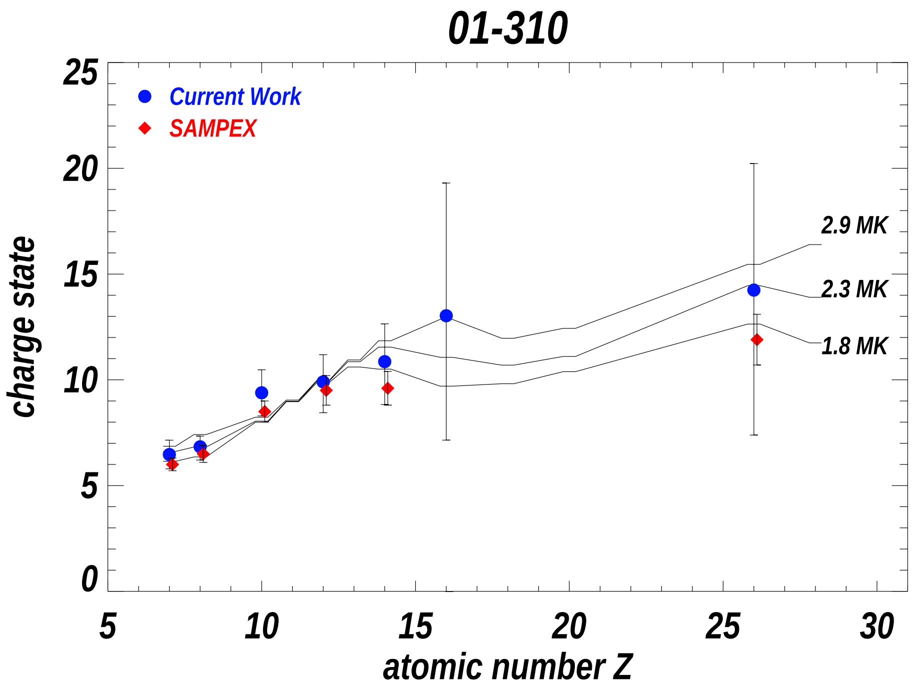

Figure 4.6: Charge states in the November 4, 2001 solar particle event. Similar in form to Figure 4.4, the disks are the current result and the diamonds are from Labrador *et al.* (2003). The charge states for the best fit temperature and the 1-σ limits are shown and labelled.

Figure 4.7 is for the April 2002 solar particle event. The best fit temperature for this event is 6.7 MK. The 1-σ range extends from 4.3 MK to 10.9 MK. Unlike in the November 2001 event, the largest contributor to χ^2 is neon, though most of the other elements have charge states consistent with the best fit temperature, except for oxygen which is low. The oxygen charge state might be more consistent with coronal temperatures (~ 2 MK). There are no SAMPEX measurements for this event for elements heavier than silicon. However, of those elements measured, all are consistent with the current results, though slightly lower, similar to the November 2001 event. The SAMPEX charge states are mostly consistent with a temperature of ~ 2 MK. The best fit temperature of 6.7 MK from the current result is much higher than typical coronal temperatures.

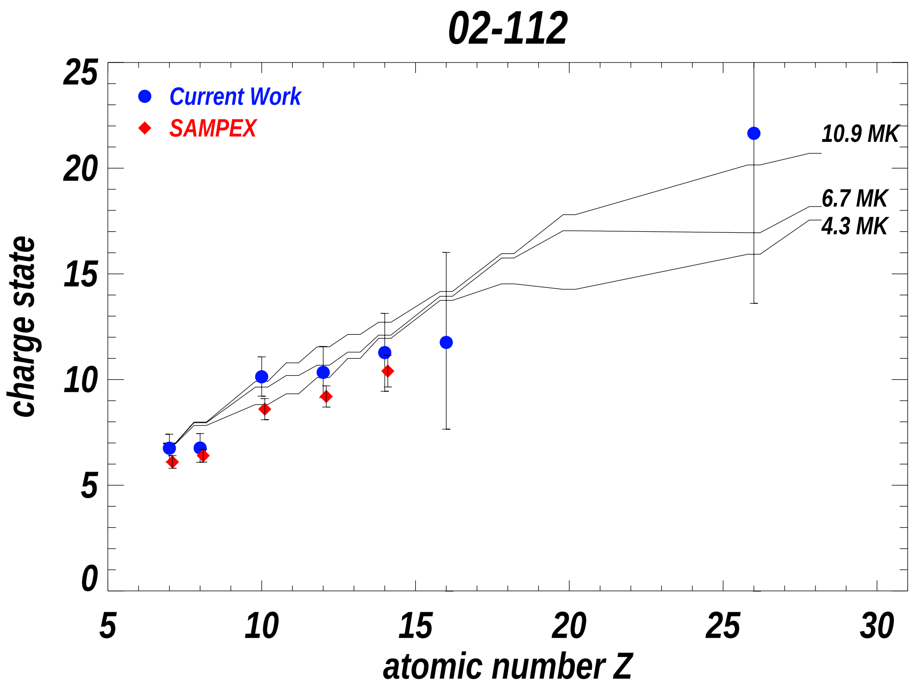

Figure 4.7: Charge states in the April 2002 solar particle event. It is similar to Figure 4.4 and Figure 4.6.

Table 4.2 shows the best fit temperatures for source plasmas in the four events. In the case of the 00-331 event, the temperature is an upper limit. It may be reasonably postulated that for two of these events, 00-331 and 01-310, the source plasma is in the corona, as the best fit temperatures are consistent with temperatures in the corona (Bochsler, 2000). For the November 6, 1997 event and the April 21, 2002 event, however, the best fit temperatures are higher than is typical for the corona. It may be that some of the SEPs in these events were accelerated out of impulsive flare regions, owing to the higher temperature (Garcia, Greer & Viereck, 1999).

If the model of collisionless acceleration out of a thermalized plasma is correct, then the charge states at lower energies should be the same as at higher energies. It may also be, however, that the best fit temperatures are not indicative of a source plasma temperature

Event	Temperature (MK)
97 − 311	$3.7\,^{+\,1.2}_{-\,0.8}$
00 − 331	≤ 1.4
01 − 310	$2.3\,^{+\,0.6}_{-\,0.5}$
02 − 112	$6.7\,^{+\,4.2}_{-\,2.4}$

Table 4.2: Fit temperatures for the four solar particle events.

at all. Examining the energy dependence of the charge states might indicate whether the best fit temperatures truly are indicative of a source plasma temperature.

4.4 Shock the monkey: charge-changing processes in shock acceleration

The temperature fitting in Section 4.3 proceeded from the assumption that the SEP charge states are unchanged by the acceleration process. The general idea was that the source plasma was in a thermal equilibrium when the CME-driven shock passed through, and that the shock acceleration process, being entirely collisionless, did not result in the further ionization or recombination of the solar particles. In other words, particle charge states are “frozen in” prior to acceleration.

But do the charge states remain the same through the shock acceleration process? If particle acceleration really is happening very close to the Sun, one would expect that the particles accelerated would pass through a very dense plasma low in the solar atmosphere. Particles might experience collisions in this plasma during acceleration with the ambient electrons and protons, resulting in charge stripping and recombination. As particles gain energy, they have been in the shock acceleration region for a longer period of time, and will have more electrons stripped. SEPs passing through a dense plasma during acceleration will approach an equilibrium charge state. This will give rise to a charge state spectrum that depends on the plasma density, the amount of time required to accelerate the particle, and the nature of the energy change process in acceleration.

As discussed in Section 1.3, several authors have looked at this problem. Calculations for charge states at energies measured in SIS were done by Ostryakov & Stovpyuk (1999) and Barghouty & Mewaldt (2000); Barghouty & Mewaldt (2000) did detailed models for two solar particle events that occurred in November 1992 and November 1997. Kovaltsov *et al.* (2001) extended the work of these authors, presenting detailed calculations of the expected charge state of iron as a function of energy for various different values of parameters in the acceleration process, as will be discussed below.

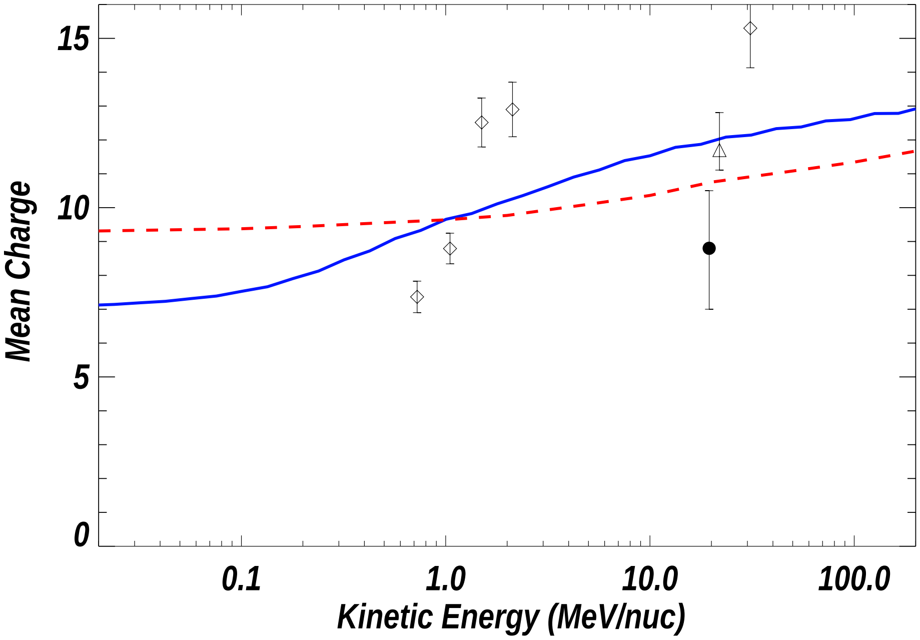

Figure 4.8: Charge states for silicon in the November 6, 1997 solar particle event (solid line) as calculated by Barghouty & Mewaldt (2000). Superposed on this calculation are charge states for the November 6, 1997 event from Mazur *et al.* (1999) (open diamonds), the result of Cohen *et al.* (1999) (open triangle) and the current result (solid circle). The dashed line is a different model calculation with a lower density and temperature.

Figure 4.8 shows calculations of silicon charge state as a function of energy by Barghouty & Mewaldt (2000) for the November 6, 1997 event. Superposed on this calculation are data for the 1997 event from Mazur *et al.* (1999), the result of Cohen *et al.* (1999) and the current result. In this calculation, a source plasma temperature of 1 MK and electron density of 2×10^9 particles per cm^3 were assumed. Also shown is another calculation (dashed line) assuming a temperature of 1.33 MK and an electron density of 3×10^8 particles per cm^3. Neither calculation does a good job of explaining all of the data. The higher density calculation is more consistent with the Cohen *et al.* (1999) result; the lower density calculation is more consistent with the current result. Neither calculation describes the SAMPEX points very well.

Figure 4.9 shows calculations of iron charge state as a function of energy by Barghouty & Mewaldt (2000) for the November 6, 1997 event. Superposed on this calculation are charge state data for this event from SAMPEX, low energy data from SEPICA, the result of Cohen *et al.* (1999) and the current result. Note that the discrepancy between the SEPICA and SAMPEX measurements is unresolved. The charge state inferred here for iron is, as is silicon, lower than that expected in the model for the 1997 event. Also shown is the lower density model calculation (dashed line). As with silicon, it would seem that the current result is more consistent with the lower density calculation than with the higher density calculation.

Barghouty & Mewaldt (2000) did calculations for silicon and iron only. It might prove fruitful to examine other charge state spectra. Figure 4.10 shows charge states of oxygen with energy per nucleon in the November 6, 1997 event. The data are from Möbius *et al.* (1999) and the current result. Oxygen is seen to be fully stripped at SIS energies. There does appear to be a large change in charge state between SEPICA energies and at ~20

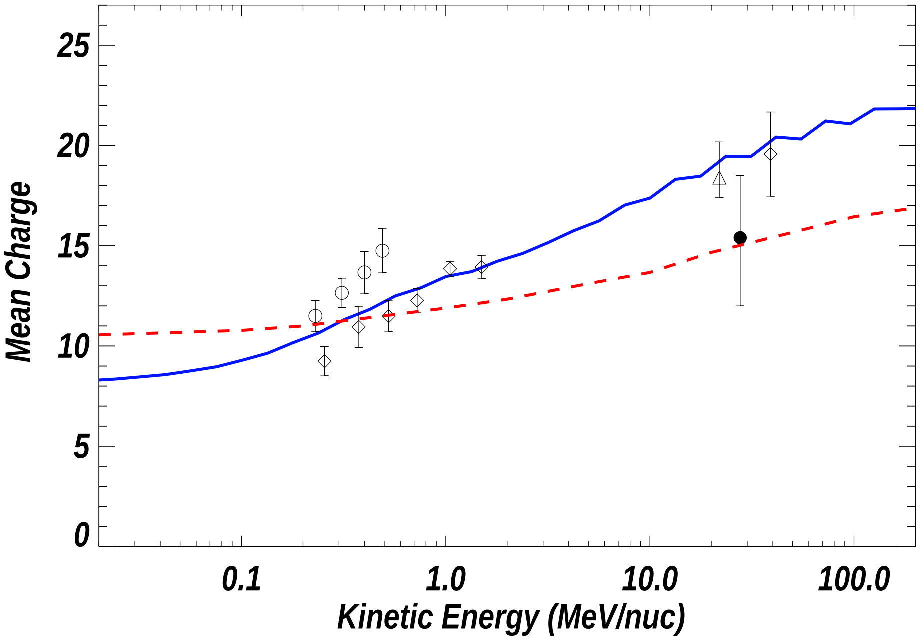

Figure 4.9: Charge states for iron in the November 6, 1997 solar particle event (solid line) as calculated by Barghouty & Mewaldt (2000). Superposed on this calculation are charge states for the November 6, 1997 event from Mazur *et al.* (1999) (open diamonds), the measurements of Möbius *et al.* (1999) (open circles), the result of Cohen *et al.* (1999) (open triangle) and the current result (solid circle). The dashed line is the lower density model calculation.

MeV/nuc. However, from the SEPICA points, it is suggested that oxygen might be fully stripped at reasonably low energies. This would mean that the oxygen charge state has reached its equilibrium value, though iron had not.

Figure 4.11 shows mean charge states of neon as measured by SEPICA (diamonds) and the current result as a function of energy. There is a one charge unit difference between the SEPICA measurements and the charge state inferred here. This difference is small compared with the size of uncertainties in all of the measurements. It would appear from the plot that the charge state could be relatively flat with energy (the measurements are consistent with each other), though the large error bars could be hiding an energy dependence.

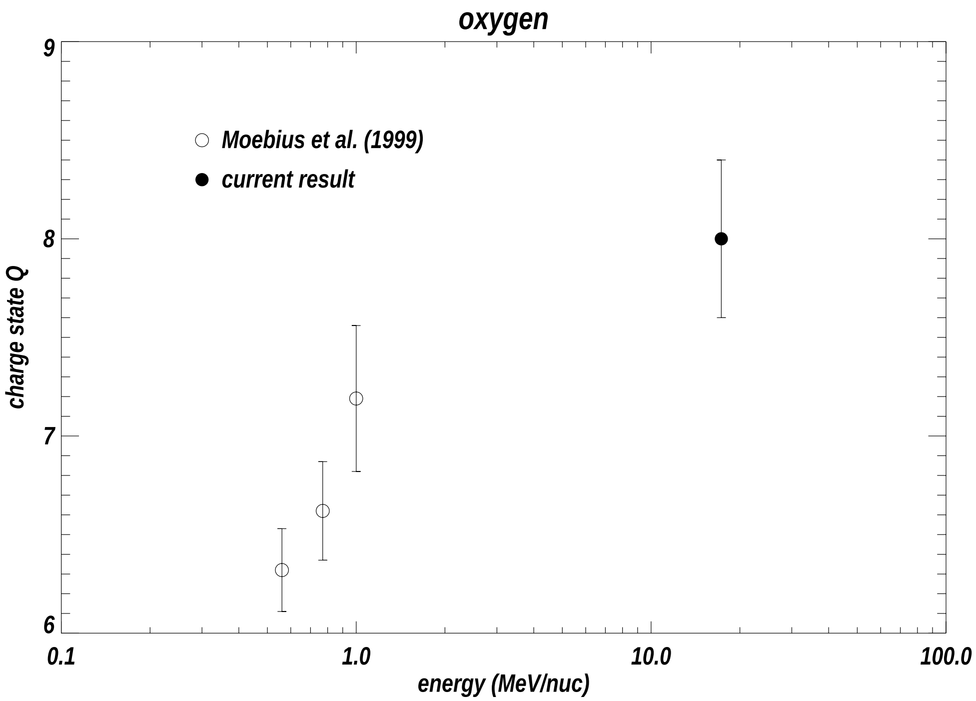

Figure 4.10: Charge states for oxygen in the November 6, 1997 solar particle event. Open circles are from Möbius *et al.* (1999); the solid circle is the current result.

Figure 4.12 shows mean charge states of magnesium, similar to figures 4.10 and 4.11. Here, the charge state looks almost completely flat with energy. As with neon, the error bars are fairly large, and could be hiding an energy dependence.

The oxygen spectrum seems to indicate that an equilibrium charge state was achieved at a fairly low energy. This might occur if there were a high density in the source plasma or a very fast energy gain mechanism (thus equilibrating the oxygen quickly in a less dense plasma). An appropriate model calculation for oxygen might show whether this is consistent with the relatively flat charge state spectra of magnesium and neon.

Another, more recent calculation was presented by Kovaltsov *et al.* (2001). In modelling the acceleration mechanism it was assumed that the rate of energy gain in acceleration of

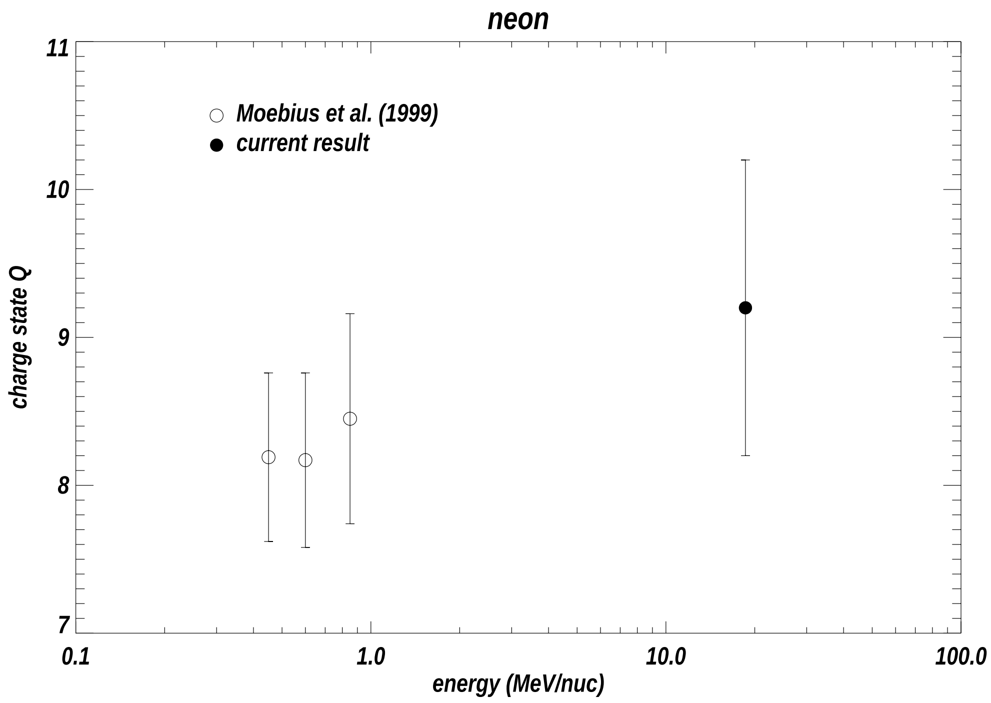

Figure 4.11: Charge states for neon in the November 6, 1997 solar particle event. Open circles are from Möbius *et al.* (1999); the solid circle is the current result.

a particle would be a power law in the particle's energy:

$$\left(\frac{dE}{dt}\right)_a = \frac{E_1}{\tau_1}\left(\frac{E}{E_1}\right)^S \tag{4.7}$$

where E_1 is taken to be 1 MeV/nuc, and τ_1 is the time required to accelerate the particle to that energy. In making their calculations, several values of the power law index S were examined.

Figure 4.13, which is a reproduction of Figure 1.8 in Chapter 1, shows a calculation of $n \times \tau_1$, or the product of the plasma density and the acceleration time to 1 MeV/nuc, as a function of the average charge state of iron at 30 MeV/nuc. For this figure, the value of the power law index is set at $S = 0$; that is, the rate of energy gain in acceleration is constant

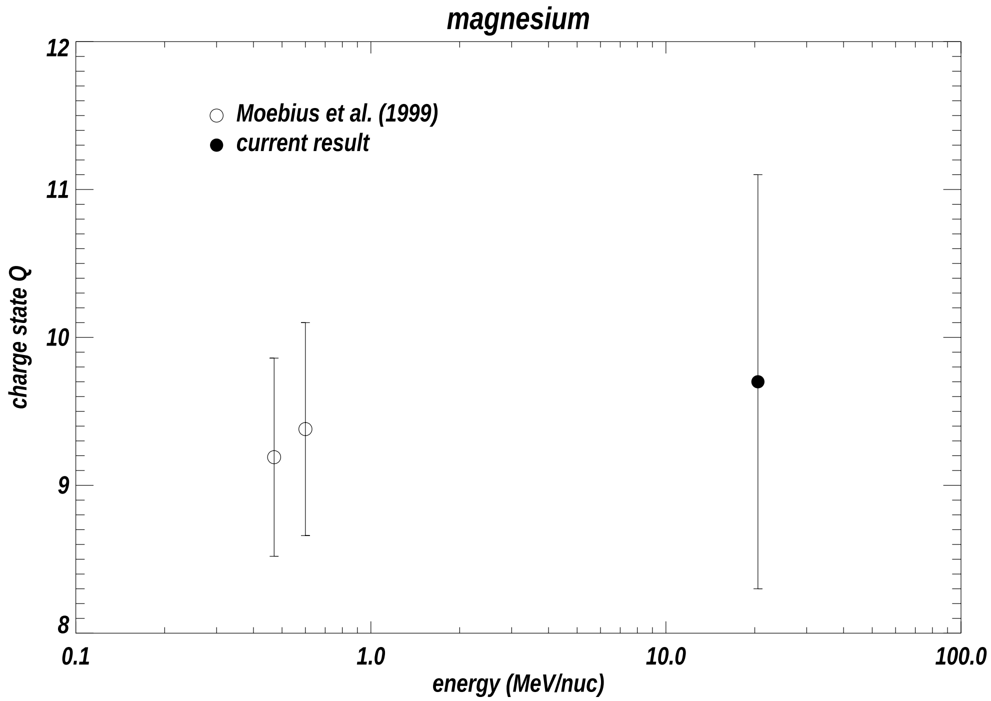

Figure 4.12: Charge states for magnesium in the November 6, 1997 solar particle event. Open circles are from Möbius *et al.* (1999); the solid circle is the current result.

with time. Superposed on this plot is the current result for iron. It can be seen that the inferred charge state for iron constrains the value of $n \times \tau_1$ to be $n \times \tau_1 = 0.010^{+0.017}_{-0.008}$ for this value of S.

The power law index S need not be constrained to be $S = 0$. Figure 4.14 shows charge state spectra of iron calculated by Kovaltsov *et al.* (2001) for different values of $n \times \tau_1$ and S. For these calculations, the charge state at 30 MeV/nuc has been fixed at $Q_{Fe} = 18$. The solid line is for $S = 1$ and $n \times \tau_1 = 2 \times 10^9 \mathrm{cm}^{-3}\mathrm{sec}$. The dashed line is for $S = 0.5$ and $n \times \tau_1 = 7.5 \times 10^8 \mathrm{cm}^{-3}\mathrm{sec}$. Either of these curves might represent the high energy data; a different selection of the parameters would also fit either of the sets of low energy data as well. These calculations are similar to those presented in Figure 1.9 in Chapter 1.

If the acceleration time τ_1 is approximately 10 seconds (Barghouty & Mewaldt, 2000),

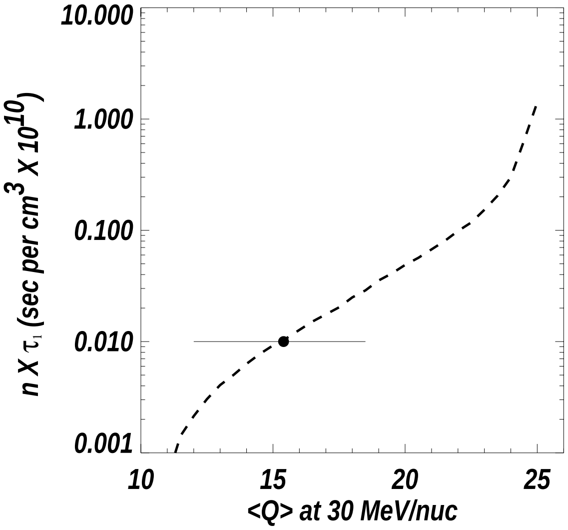

Figure 4.13: The product of electron density and time of acceleration to 1 MeV/nuc as a function of the average charge state of iron at 30 MeV/nuc. Calculation from Kovaltsov *et al.* (2001). The charge state of iron inferred for the November 6, 1997 event is superposed. It can be seen from the best fit charge state and uncertainties that the product of the electron density and time of accleration is $\sim 0.010^{+0.017}_{-0.008}$.

then the plasma density in the acceleration region is $\sim 0.75 - 2 \times 10^8$ particles per cm^3. According to Guhathakurta, Holzer & MacQueen (1996), this density is what one finds at about 1.1-1.3 solar radii above the surface of the Sun. This size scale would seem to indicate that particle acceleration happens relatively early in a CME, which can become much larger as shown in Figure 1.3 in Chapter 1. This density is also the same order of magnitude as in the lower density fit of Barghouty & Mewaldt (2000).

The various calculations of charge stripping processes in shock acceleration can be made to describe the charge state spectra in the November 6, 1997, event reasonably well. The temperatures assumed in these models are all typical for the corona. The locations from which the particles are accelerated in these models are also consistent with the lower corona. In this event, the energy dependence of the charge states would seem to indicate that the

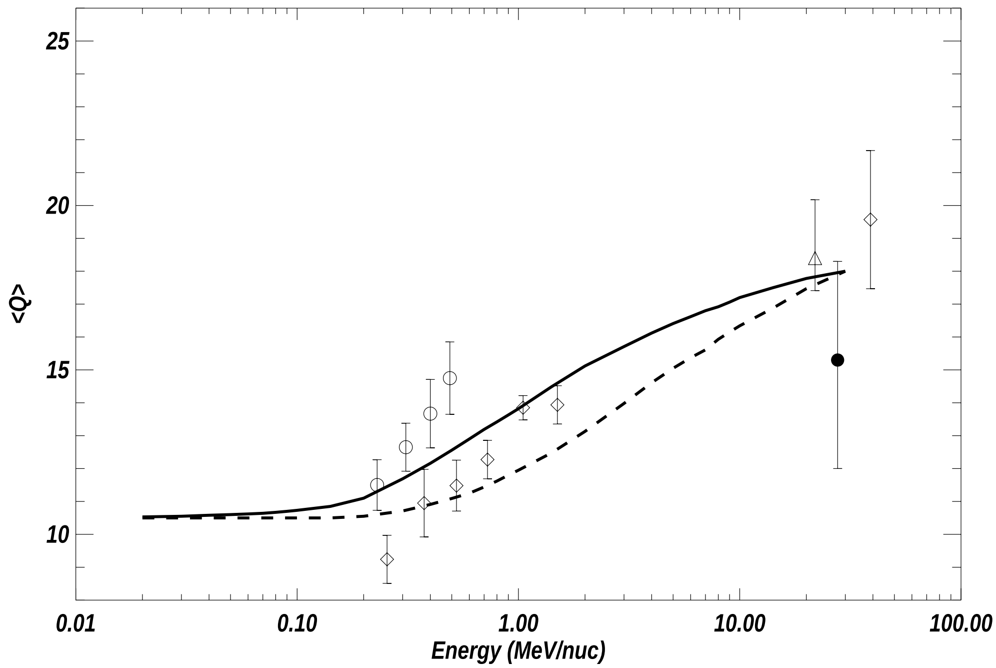

Figure 4.14: The mean charge state of iron as a function of energy as calculated by Kovaltsov *et al.* (2001). Here, the iron charge state at 30 MeV/nuc has been fixed at a value of $Q_{Fe} = 18$, and calculations have been done for $n \times \tau_1 = 2 \times 10^9 \mathrm{cm}^{-3}\mathrm{sec}$ and $S = 1$ (solid curve) and for $n \times \tau_1 = 7.5 \times 10^8 \mathrm{cm}^{-3}\mathrm{sec}$ and $S = 0.5$ (dashed curve). Also plotted are the various results for the November 6, 1997 event: the current result (solid circle), the results of Möbius *et al.* (1999) (open circles), Mazur *et al.* (1999) (open diamonds) and the Cohen *et al.* (1999) (open triangle) result.

temperature inferred in Section 4.3 is not a true source temperature. That a consistent temperature or "pseudotemperature" is measured for this event is therefore somewhat of a mystery. It may be that applying the model of Kovaltsov *et al.* (2001) to other elements may solve this mystery by predicting charge state spectra consistent with the data.

It has been suggested (Cohen *et al.*, 1999; Mazur *et al.*, 1999; Möbius *et al.*, 1999) that the particles in the November 6, 1997 event could be the result of mixing between source populations from a gradual event and from a hot flare region. The work modelling charge equilibration in shock acceleration indicates that a hot flare source need not be invoked to explain the charge states seen here or by other authors. Mixing with remnant suprathermal material (Mason, Mazur & Dwyer, 1999) is not excluded by this work, however, as remnant suprathermal ions would undergo the same equilibration process as other particles in the November 6, 1997 event.

The temperature inferred for the April 21, 2002 event may also not be a true temperature, but be indicative of this kind of charge changing process. Extending the model of Kovaltsov *et al.* (2001) to other elements might allow a calculation of expected charge state versus atomic number at the energies observed in SIS. Armed with such a calculation, measurements of the sort done here at high energies possibly could be used as a probe for the acceleration process even when lower energy measurements of charge states are unavailable.

Chapter 5

Conclusions

5.1 How well does this really work?

The propagation model used to deduce charge states in this work is practically as old as the field of space physics itself. Newer models have expanded upon it for the periods of event onsets. In the equilibrium decay phase of a solar particle event it is still quite accurate. The preceding ~100 pages have shown how to use this rusty old model to make a very difficult measurement in a relatively straightforward way. In solar particle events with appropriate conditions, that is, an equilibrium decay phase, one can deduce the charge states of solar particles at energies of ~ 10-100 MeV/nuc. This supplements only three other methods currently in use at these energies, two of which have been used for only a single event.

Deducing charge states is still difficult, however, and it is made so by the nature of the propagation mechanism itself. The rigidity dependence of the diffusion mean free path is slight enough ($\lambda \sim R^{0.28}$) that one requires very high precision measurements of the decay timescales, and very little change from a perfect equilibrium decay to differentiate from the case where there is no rigidity dependence at all, where charge state measurements cannot be made. Such a situation happens in other events, such as in the August 15, 2001 event. If the mean free path were more strongly dependent on the rigidity (if γ were higher) than that measured here, this would be a far more effective method.

The other limiting factor with this method is statistics. In order to make a high precision measurement of a decay timescale, one needs a large number of counts. The SIS instrument is one of the largest solid state particle telescopes ever flown in space, but only can gather enough particles to make firm estimates of charge states in three solar particle events over the course of four and half years that included a solar maximum. For some of the largest events that have occurred over the course of the ACE mission, however, the very size of SIS has limited its particle collection power when it has been saturated during high event rates periods.

The inclusion of ULEIS data can help for those events for which SIS returns high enough fidelity data, as those data are at a lower energy where the constant timescale τ_C dominates the equilibrium decay. This can help fix the value of τ_C, which in turn helps fix the value of γ. Data at higher energies, were it available, would also help fix the value of γ, which would greatly help the measurements presented here.

5.2 That's the one, Officer! – Making the identification from the line-up of models

The charge states deduced here have been used to examine two different and competing ideas on the origins of solar energetic particles. One of the models is that particles are accelerated out of a plasma with which they are in thermal equilibrium. The successful fitting of a single temperature to as many as ten different charge states would seem to bolster this idea. Three solar events have been observed to have charge states of several different particle species consistent with a single source temperature. An upper limit for a temperature has been placed on a fourth event. For two of these events, the temperatures found are consistent with acceleration from a coronal source plasma. For the other two, the temperatures found are higher than is typically found in the corona. In this model, this might suggest mixing with a higher temperature source, perhaps from a hot flare region. The presence of flare source material in the large gradual solar event of November 6, 1997 has been suggested by other authors (Cohen *et al.*, 1999; Mazur *et al.*, 1999; Möbius *et al.*, 1999).

A charge state for a given ion species at one particular energy is not enough to tell the whole story, however. In order to differentiate between the different ideas of the origins of solar particles, it is necessary to look at how the charge states evolve with energy. When looking at charge state data assembled from a number of sources in the November 6, 1997 event, it becomes apparent that the temperature fitted to this event in Section 4.3 cannot represent the temperature of a single source plasma: otherwise, one would find the same charge states at low energies as one finds at higher energies. Instead, most of the elements seem to show increasing charge state with increasing energy. These data would still be consistent with the suggestion of mixing between a low energy gradual source population and a high energy impulsive source population (Cohen *et al.*, 1999), although no theoretical model has yet been developed to account for how such mixing would occur in this event. One model by Tylka *et al.* (2001) can describe mixing with remnant flare material in the Bastille Day, 2000, event, but cannot describe the observed charge state spectra in the November 6, 1997, event.

The recent work done in modelling charge equilibration from stripping in shock acceleration in a dense plasma may be giving results that compare favorably with the data for the November 6, 1997 event. In comparing the model calculations of Barghouty & Mewaldt

(2000) with iron and silicon data, and the calculations of Kovaltsov *et al.* (2001) with iron, it is seen that for appropriately chosen parameters, the observed charge state spectra of these elements can be adequately described by the models. Both of these models show that the acceleration in this event is taking place in a plasma at coronal temperatures, and at locations consistent with the lower corona. It would seem that one need not invoke a source of hot impulsive flare material to explain the charge states inferred here.

There is still a mystery in the November 6, 1997 event: if the charge states of solar energetic particles in this event are not indicative of a source plasma temperature, then why are they all consistent with a single temperature? It may prove useful to extend the calculations of Kovaltsov *et al.* (2001) to other elements in order to see if a consistent set of parameters may be chosen that describe all of these charge spectra. Doing these calculations for other elements could also provide insight into the charge states inferred for different elements at high energies in an event. It could well be that the high temperature inferred for the April 21, 2002 event may be, as in the November 6, 1997 event, an artifact of the shock acceleration process. Extending the calculations to different elements could allow measurements of the sort done here to shed new light on the physics of shock acceleration even when measurements of charge states are not available at lower energies.

In the early seventeenth century, a renowned natural philosopher by the name of Galileo Galilei became the first person to observe that the Sun was a dynamic body, instead of a static, unchanging sphere. In the intervening four centuries, natural philosophers and space physicists have been attempting to refine Galileo's early observation. All of what has been presented here is but a very small part of the vast panoply of ongoing work to seek out and discover why the Sun is so dynamic.

Bibliography

Anders, E. and Grevesse, N. 1989, Geochimica et Cosmochimica Acta, 53, 197.

Andersen, H. H. and Ziegler, J. F. 1977, Hydrogen Stopping Powers and Ranges in All Elements, (New York: Pergamon Press).

Arnaud, M. and Raymond, J. 1992, Astrophys. J., 398, 394.

Arnaud, M. and Rothenflug, R. 1985, Astron. & Astrophys., 60, 425.

Barghouty, A. F. and Mewaldt, R. A. 2000, in AIP Conf. Proc. 528: Acceleration and Transport of Energetic Particles Observed in the Heliosphere, 71.

Beeck, J., Mason, G. M., Hamilton, D. C., Wibberenz, G., Kunow, H., Hovestadt, D., and Klecker, B. 1987, Astrophys. J., 322, 1052.

Bevington, P. 1969, Data Reduction and Error Analysis for the Physical Sciences, (New York: McGraw-Hill Book Company).

Biermann, L. 1951, Zeitschrift fur Astrophysics, 29, 274.

Bochsler, P. 2000, Reviews of Geophysics, 38, 247.

Breneman, H. H. and Stone, E. C. 1985, Astrophys. J., 299, L57.

Burlaga, L. F. 1967, Journal of Geophysical Research, 72, 4449.

Cohen, C. M. S. *et al.* 1999, Geophys. Res. Lett., 26, 149.

Compton, A. H. and Getting, I. A. 1935, Physical Review, 47, 817.

Cook, W. R., Stone, E. C., and Vogt, R. E. 1984, Astrophys. J., 279, 827.

Dalla, S., Balogh, A., Heber, B., Lopate, C., and McKibben, R. B. 2002, in Journal of Geophysical Research (Space Physics), Volume 107, Issue A11, pp. SSH 12-1, CiteID 1370, DOI 10.1029/2001JA009155, 12.

Dietrich, W. and Lopate, C. 1999, in Proceedings of the 26th International Cosmic Ray Conference 6, 91.

Dietrich, W. and Tylka, A. 2001, in Proceedings of the 27th International Cosmic Ray Conference, 3173.

Dröge, W. 2000a, Space Science Reviews, 93, 121.

Dröge, W. 2000b, Astrophys. J., 537, 1073.

Dröge, W. 1994, Astrophys. J. Suppl., 90, 567.

Earl, J. A. 1976, Astrophys. J., 205, 900.

Fisk, L. A., Gloeckler, G., Zurbuchen, T. H., and Schwadron, N. A. 2000, in AIP Conf. Proc. 528: Acceleration and Transport of Energetic Particles Observed in the Heliosphere, 229.

Forman, M. A. 1970, Planet. Space Sci., 18, 25.

Forman, M. A. 1971, Journal of Geophysical Research, 76, 759.

Garcia, H. A., Greer, S., and Viereck, R. 1999, in ESA SP-448: Magnetic Fields and Solar Processes, 983.

Gleeson, L. J. and Axford, W. I. 1968, Astrophys. Space Sci., 2, 431.

Grevesse, N., Noels, A., and Sauval, A. J. 1996, in ASP Conf. Ser. 99: Cosmic Abundances, 117.

Guhathakurta, M., Holzer, T. E., and MacQueen, R. M. 1996, Astrophys. J., 458, 817.

Jokipii, J. R. 1966, Astrophys. J., 146, 480.

Jokipii, J. R. 1971, Reviews of Geophysics and Space Physics, 9, 27.

Klecker, B. *et al.* 2000, in AIP Conf. Proc. 528: Acceleration and Transport of Energetic Particles Observed in the Heliosphere, 135.

Kovaltsov, G. A., Barghouty, A. F., Kocharov, L., Ostryakov, V. M., and Torsti, J. 2001, Astron. & Astrophys., 375, 1075.

Labrador, A., Leske, R., Mewaldt, R., Stone, E., and von Rosenvinge, T. 2003, in Proceedings of the 28th International Cosmic Ray Conference.

Lee, M. A. 2000, in AIP Conf. Proc. 528: Acceleration and Transport of Energetic Particles Observed in the Heliosphere, 3.

Leske, R. A., Mewaldt, R. A., Cummings, A. C., Stone, E. C., and von Rosenvinge, T. T. 2001, in AIP Conf. Proc. 598: Joint SOHO/ACE workshop "Solar and Galactic Composition", 171.

Lupton, J. E. 1973. PhD thesis, California Institute of Technology.

Lupton, J. E. and Stone, E. 1973, J. Geophys. Res., 78, 1007.

Möbius, E. *et al.* 2000, in AIP Conf. Proc. 528: Acceleration and Transport of Energetic Particles Observed in the Heliosphere, 131.

Möbius, E. *et al.* 1999, Geophys. Res. Lett., 26, 145.

Mason, G. M. *et al.* 1998, Space Science Reviews, 86, 409.

Mason, G. M., Mazur, J. E., and Dwyer, J. R. 1999, Astrophys. J., 525, L133.

Mazur, J. E., Mason, G. M., Looper, M. D., Leske, R. A., and Mewaldt, R. A. 1999, Geophys. Res. Lett., 26, 173.

McComas, D. J., Bame, S. J., Barker, P., Feldman, W. C., Phillips, J. L., Riley, P., and Griffee, J. W. 1998, Space Science Reviews, 86, 563.

McKibben, R. B. 1972, Journal of Geophysical Research, 77, 3957.

Meyer, P., Parker, E. N., and Simpson, J. A. 1956, Physical Review, 104, 768.

Ostryakov, V. M. and Stovpyuk, M. F. 1999, Solar Physics, 189, 357.

Palmer, I. D. 1982, Reviews of Geophysics and Space Physics, 20, 335.

Parker, E. N. 1958a, Physical Review, 110, 1445.

Parker, E. N. 1958b, Astrophys. J., 128, 664.

Parker, E. N. 1963, Interplanetary Dynamical Processes, (New York: Interscience Publishers).

Parks, G. K. 1991, Physics of Space Plasmas, (Reading, Massachusetts: Perseus Books).

Popecki, M., Möbius, E., Klecker, B., Galvin, A. B., Kistler, L. M., and Bogdanov, A. T. 2000a, in AIP Conf. Proc. 528: Acceleration and Transport of Energetic Particles Observed in the Heliosphere, 63.

Popecki, M. A. *et al.* 2000b, in AIP Conf. Proc. 528: Acceleration and Transport of Energetic Particles Observed in the Heliosphere, 139.

Press, W. H., Teukolsky, S. A., Vetterling, W. T., and Flannery, B. P. 1992, Numerical Recipes in C, 2nd ed., (Cambridge, UK: Cambridge University Press).

Reames, D. V. 1999, Space Science Reviews, 90, 413.

Reames, D. V., Barbier, L. M., and Ng, C. K. 1996, Astrophys. J., 466, 473.

Reames, D. V., Kahler, S. W., and Ng, C. K. 1997, Astrophys. J., 491, 414.

Simnett, G. M. 1996, Advances in Space Research, 17, 75.

Smith, C. W., L'Heureux, J., Ness, N. F., Acuña, M. H., Burlaga, L. F., and Scheifele, J. 1998, Space Science Reviews, 86, 613.

Smith, C. W. *et al.* 2001, Solar Physics, 204, 227.

Stoker, P. H. and Makgamathe, S. 1990, Astrophys. J. Suppl., 73, 263.

Stone, E. 1974, Proceedings of the ESRO Workshop, Frascati, Italy, 1.

Stone, E. C. *et al.* 1998b, Space Science Reviews, 86, 285.

Stone, E. C. *et al.* 1998a, Space Science Reviews, 86, 357.

Stone, E. C., Frandsen, A. M., Mewaldt, R. A., Christian, E. R., Margolies, D., Ormes, J. F., and Snow, F. 1998c, Space Science Reviews, 86, 1.

Tylka, A. J., Cohen, C. M. S., Dietrich, W. F., Maclennan, C. G., McGuire, R. E., Ng, C. K., and Reames, D. V. 2001, Astrophys. J., 558, L59.

Williams, D. L. 1998. PhD thesis, California Institute of Technology.

Zank, G. P., Matthaeus, W. H., Bieber, J. W., and Moraal, H. 1998, J. Geophys. Res., 103, 2085.

Appendix A

Events and Ranges Selected

Section 3.5.2 discussed finding a period of exponential decay in an otherwise very complicated event, and the various ways in which a particular energy range of a particular element might or might not be acceptable for inclusion into the fit of decay timescale versus energy. In this appendix, all of the energy ranges used in SIS and ULEIS are documented, as well as the periods chosen. The latter are documented in a series of synopsis plots similar to Figure 3.11 in Chapter 3.

Recall from Chapter 3 that SIS has eight ranges that are normally analyzed, denoted ranges 0 through 7. Range 0 particles stop in the second matrix detector, M2. Range 1 particles stop in the first stack detector, T1; range 2 particles stop in T2, and so forth through range 7 particles that stop in stack detector T7. Table A.1 shows the energy ranges for all of the ranges in SIS of all of the elements used in the analysis. Table A.2 is a complete listing of all of the ranges used for each element in each event analyzed. Those ranges not listed in Table A.2 did not meet the criteria of Chapter 3 for inclusion in the fit.

ULEIS data were included in three of the events analyzed. In the November 6, 1997 event, carbon was included at 1.81-2.56 MeV/nuc, and oxygen was included in the energy ranges 1.28-1.81 MeV/nuc, 1.81-2.56 MeV/nuc, and 3.62-5.12 MeV/nuc. In the November 4, 2001 event, oxygen was included at 2.56-5.12 MeV/nuc (which would be a combination

Range	Carbon	Nitrogen	Oxygen	Neon
0	6.12 – 8.62	6.61 – 9.33	7.05 – 9.99	7.82 – 11.15
1	8.62 – 11.23	9.33 – 12.18	9.99 – 13.07	11.15 – 14.64
2	11.23 – 13.40	12.18 – 14.56	13.07 – 15.63	14.64 – 17.56
3	13.40 – 17.94	14.56 – 19.51	15.63 – 20.97	17.56 – 23.62
4	17.94 – 25.12	19.51 – 27.34	20.97 – 29.42	23.62 – 33.22
5	25.12 – 33.21	27.34 – 36.17	29.42 – 38.94	33.22 – 44.02
6	33.21 – 54.30	36.17 – 59.19	38.94 – 63.77	44.02 – 72.24
7	54.30 – 76.34	59.19 – 83.26	63.77 – 89.78	72.24 – 101.83
Range	Sodium	Magnesium	Silicon	Sulfur
0	7.91 – 11.34	8.47 – 12.16	9.03 – 13.04	9.51 – 13.83
1	11.34 – 14.94	12.16 – 16.03	13.04 – 17.26	13.83 – 18.37
2	14.94 – 17.94	16.03 – 19.26	17.26 – 20.79	18.37 – 22.17
3	17.94 – 24.19	19.26 – 25.99	20.79 – 28.13	22.17 – 30.10
4	24.19 – 34.08	25.99 – 36.64	28.13 – 39.76	30.10 – 42.66
5	34.08 – 45.21	36.64 – 48.63	39.76 – 52.87	42.66 – 56.81
6	45.21 – 74.28	48.63 – 79.97	52.87 – 87.14	56.81 – 93.85
7	74.28 – 104.77	79.97 – 112.9	87.14 – 123.2	93.85 – 132.9
Range	Calcium	Iron	Nickel	
0	10.28 – 15.16	10.47 – 15.83	11.01 – 16.71	
1	15.16 – 20.30	15.83 – 21.53	16.71 – 22.76	
2	20.30 – 24.61	21.53 – 26.30	22.76 – 27.85	
3	24.61 – 33.60	26.30 – 36.31	27.85 – 38.50	
4	33.60 – 47.87	36.31 – 52.22	38.50 – 55.47	
5	47.87 – 63.99	52.22 – 70.23	55.47 – 74.69	
6	63.99 – 106.22	70.23 – 117.53	74.69 – 125.24	
7	106.22 – 150.87	117.53 – 167.66	125.24 – 178.96	

Table A.1: Energy ranges in SIS for all of the elements in the analysis.

in the Level 2 data of the 2.56-3.62 and 3.62-5.12 MeV/nuc energy ranges). In the April 21, 2002 event, oxygen was used at the same energy range.

Four solar particle events were analyzed in this work: events on November 6, 1997, November 26, 2000, November 4, 2001, and April 21, 2002. The time periods used are summarized in Table A.3. Recall that the data are 10,752-second averages, being about three hours. In Table A.3, the times listed denote the start times of the periods used.

In the following pages, synopsis plots of the sort described in section 3.5.2 are presented

Element	97 – 311	00 – 331	01 – 310	02 – 112
Carbon	1 – 7	1 – 6	1 – 5	2 – 6
Nitrogen	1 – 6	1 – 5	1 – 5	2 – 6
Oxygen	1 – 7	1 – 7	1 – 5	2 – 6
Neon	1 – 6	1 – 6	1 – 5	1 – 5
Sodium	1 – 4	––	––	––
Magnesium	1 – 6	1 – 4	1 – 4	1 – 5
Silicon	1 – 6	1 – 4	1 – 4	1 – 4
Sulfur	1 – 6	––	1	1 – 3
Calcium	2 – 4	––	––	––
Iron	1 – 7	––	1	1 – 2
Nickel	1 – 4	––	––	––

Table A.2: Ranges in SIS of elements used in the various events in the analysis.

Event	Period of Interest
November 6, 1997	310.994 – 311.990
November 26, 2000	332.114 – 333.843
November 4, 2001	311.358 – 311.980
April 21, 2002	111.990 – 113.484

Table A.3: Time periods used in the analysis for each event. The times are given in day of the year in which the event took place; they are the start times of the 10,752-second (∼3-hour) averages. So the end time given for each event is actually the start time of the last 3-hour average used in the event.

for the four events analyzed. These plots include five panels, for intensity profiles, intensity ratios, direction of the interplanetary magnetic field, other parameters of the magnetic field, including magnitude, and the solar wind speed. The dashed vertical lines in each plot correspond to the period of interest.

The top plot in each of the synopsis plots is a set of time intensity profiles for the eight ranges in SIS during this event. What is plotted is intensity in particles per cm^2 sec ster MeV/nuc. The top curve is for range 0 (see Table A.1) carbon; lower curves are for ranges 1 through 7. The time on the x-axis is in day of whatever year the event happened (in UTC). November 6 corresponds to day 310.

The second plot is for intensity ratios. This plot is a mostly a device for looking at when decay timescales might depend on rigidity. Looking at the top plot, it might not be obvious that the decay timescales are at all different from one another in the various ranges. In the second plot, the ratios are taken of the intensities in the top plot with respect to range 2 carbon. One can see the ratios diverging over the course of the periods of interest in these events. By itself, this is not a diagnostic of rigidity-dependent decay timescales: such a divergence can be seen when the intensities are not exponentially decaying.

The third plot is for the magnetic field direction. In this plot, the magnetic field direction is presented graphically. Each line is an arrow that starts at the $y = 0$ line in the plot at the time on the x-axis, and extends into the direction of the field. In effect, one is seeing a set of sketches of the field set next to each other. Sometimes they overlap. In this plot, the Sun would be straight up for each of the sketches. The nominal Parker field would be on a line inclined 45 degrees clockwise from the Sun's direction; the field would either point up and to the right or down and to the left depending on the magnetic polarity.

The fourth plot is of magnetic field strength (solid line), variance (dashed line) and RMS variation of the high time resolution measurements from the MAG instrument. These are all plotted in units of nT.

The last plot is for the solar wind speed as measured by SWEPAM.

The figure opposite is the synopsis plot for the November 6, 1997 event. The intensities in this event peaked at about day 311.0 (midnight UTC on November 7), and proceeded to decay exponentially for the following few days. At times after the period of interest, although intensities in the lower energy ranges of carbon still are exponential, intensities at high energies (range 7 carbon, for instance) seem to be deviating from an exponential decay. Other elements at higher energies also exhibit this phenomenon. There is a small transient at about day 311.7; in range 2 carbon, this transient appear as a dip. This exaggerates the the transient in the flux ratios. There appears to be a reversal of the field direction during the period of interest, but it does not appear to have affected the equilibrium decay. There seems to be some variability in the other parameters of the magnetic field in the period of interest, but it does not appear to have affected the equilibrium decay. There was not a great deal of activity in the solar wind speed, which decreased from $\sim$450 km/sec to $\sim$400 km/sec in that time.

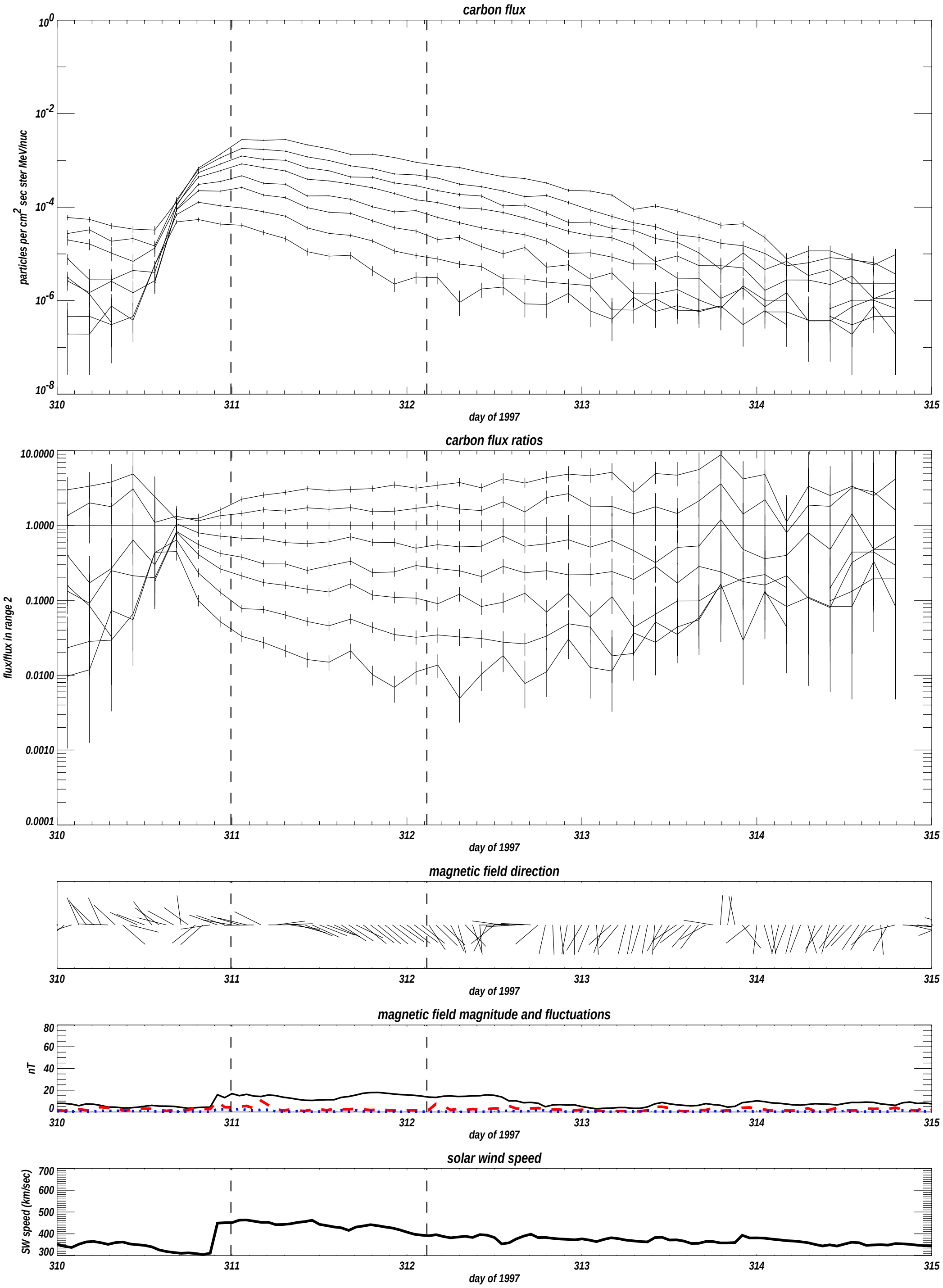

Figure A.1: Synopsis plot for the November 6, 1997 solar event.

The plots opposite are for the November 26, 2000 event. The onset for this event was rather gradual, unlike in the November 6, 1997 event. That event occurred on the western limb of the Sun, at a place that was well connected to the ACE spacecraft along the Parker field. The November 26, 2000 event, however, may have occurred either on the eastern side of the sun or in the center of the solar disk and may not have been well connected magnetically to the spacecraft. In the case of a poorly connected event, solar particles must diffuse azimuthally in order to reach ACE. Note that during the onset period of an event, such things as the location of the event on the Sun can be important: propagation effects inside of 1 AU are the dominant influences on the behavior of the intensity profiles. In the equilibrium decay phase of an event, it is the propagation effects beyond 1 AU that become the dominant influences.

Although the intensity level of range 0 carbon was comparable to that event, higher energy ranges of carbon appear at lower intensity levels: this event had a much softer spectrum than the 1997 event. One can see that the intensities are already decaying prior to the period of interest. However, they were decaying with different timescales than in the period of interest which likely involved other factors than equilibrium decay. One can see that in the period of interest, the intensity ratios are diverging, as one would expect. At the time of the peak of the intensity profiles in this event, the magnetic field was changing rapidly in direction, magnitude and variance. During the period of interest, there is still some activity, though at lower levels than just after the intensity peaks. The solar wind speed seems to be varying between $\sim$500 km/sec and $\sim$ 600 km/sec during the period of interest.

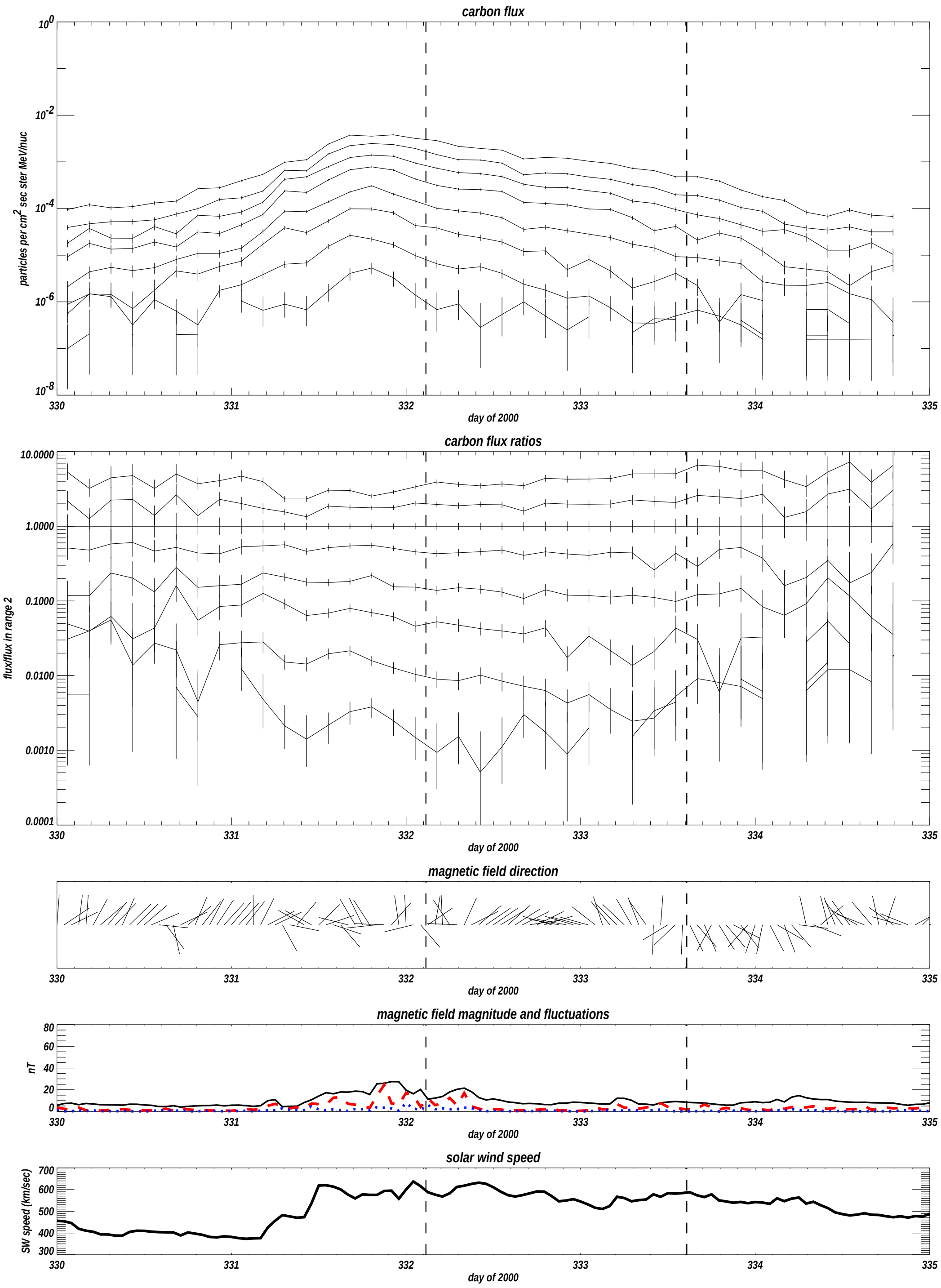

Figure A.2: Synopsis plot for the November 26, 2000 event.

The plots opposite are for the November 4, 2001 event. These are the plots that are discussed at length in Section 3.5.2. Prior to the period of interest in this event, the time intensity profiles are undergoing changes unrelated to equilibrium decay. The magnetic field is seen to have large variations in direction and magnitude. There were no SWEPAM data prior to ~ 311.1 due to the effects of the high particle intensities unrelated to the solar wind on the instrument. During the period of interest, one can see the intensity ratios diverging as the magnetic field becomes steady. The solar wind speed is decreasing from ~650 km/sec to ~550 km/sec.

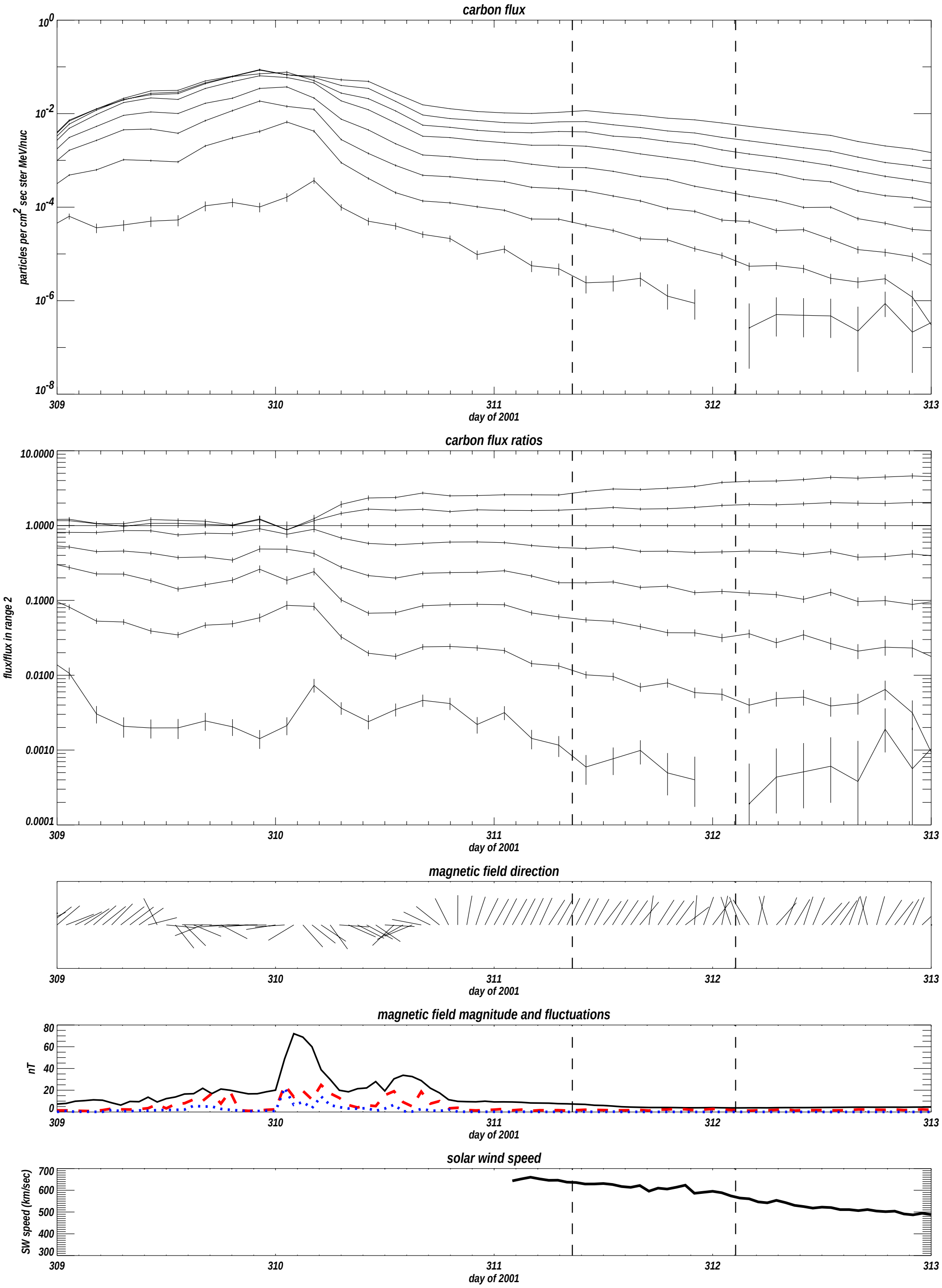

Figure A.3: Synopsis plot for the November 4, 2001 event.

The plots opposite are for the April 21, 2002 event. In the period of interest, there is a transient in the solar wind speed and in the magnetic field parameters on day 113. This does not seem to have affected equilibrium decay at that time. It can be seen that the range 0 carbon is decaying more rapidly than the other species. This is an instrumental effect involving the livetime in high intensity periods. After the period of interest, there appears to be a fresh injection of material: intensities at the lower energies actually rise after the period of interest. Careful examination of the carbon intensities will show that at early times in the period of interest, there are devations in some of the ranges from an exponential decay. However, in this event, these deviations did not affect the exponential fits.

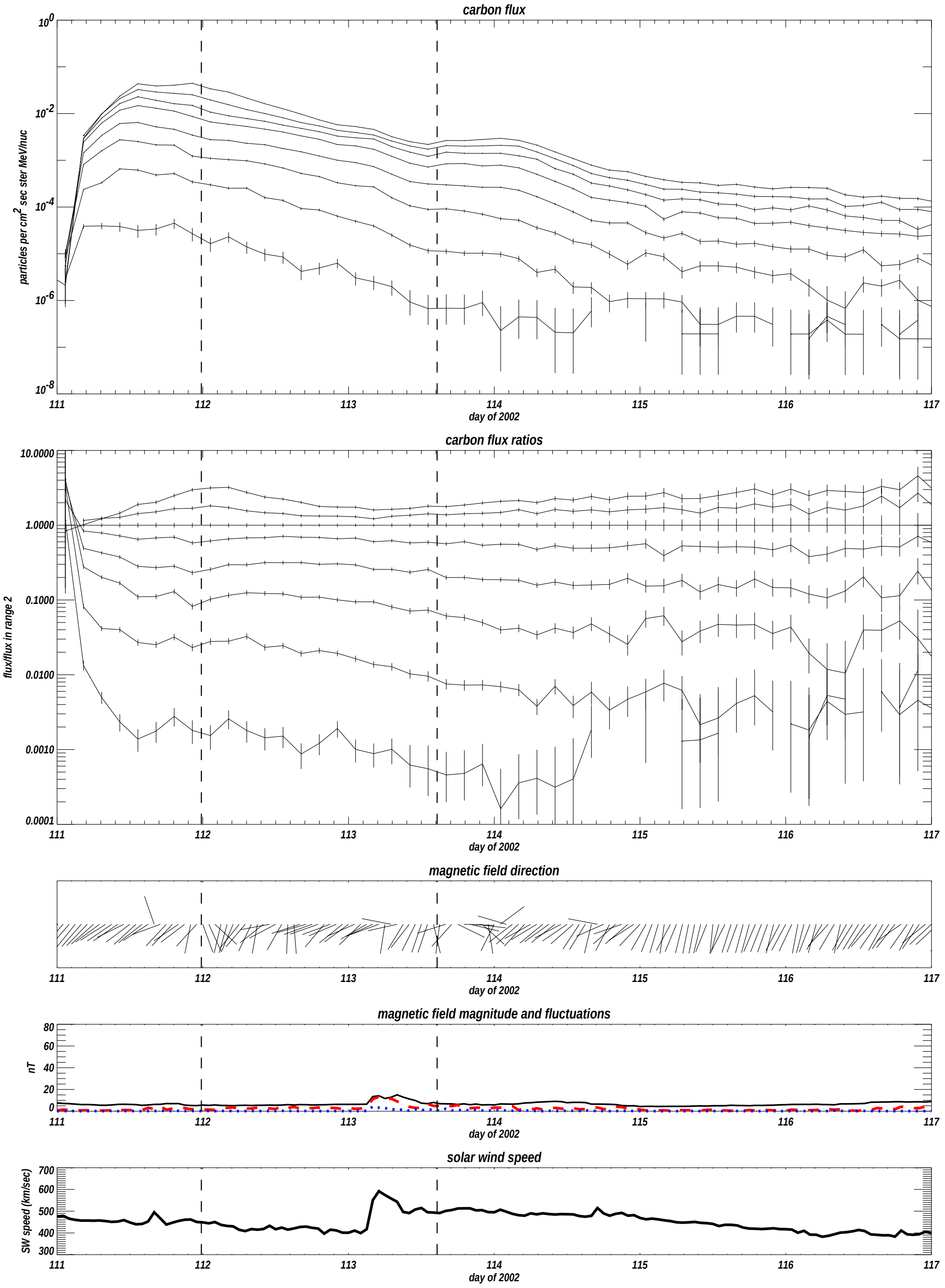

Figure A.4: Synopsis plot for the April 21, 2002 solar event.

The plots on the opposite page are for a solar particle event that occurred on August 15, 2001. This event was not used in the analysis. Examination of the top two plots will show why: the intensity ratios are flat with time, indicating that the decay timescales were independent of energy. Note also that after about day 230, intensities are almost flat with time: the decay timescale for this event is very long. This will occur when the quantity L^2/κ is very large: that is, when the boundary distance L is very large or the diffusion coefficient κ is very small. In this regime, the constant convective timescale τ_C term in the parameterization dominates over the rigidity dependent diffusive timescale τ_D term.

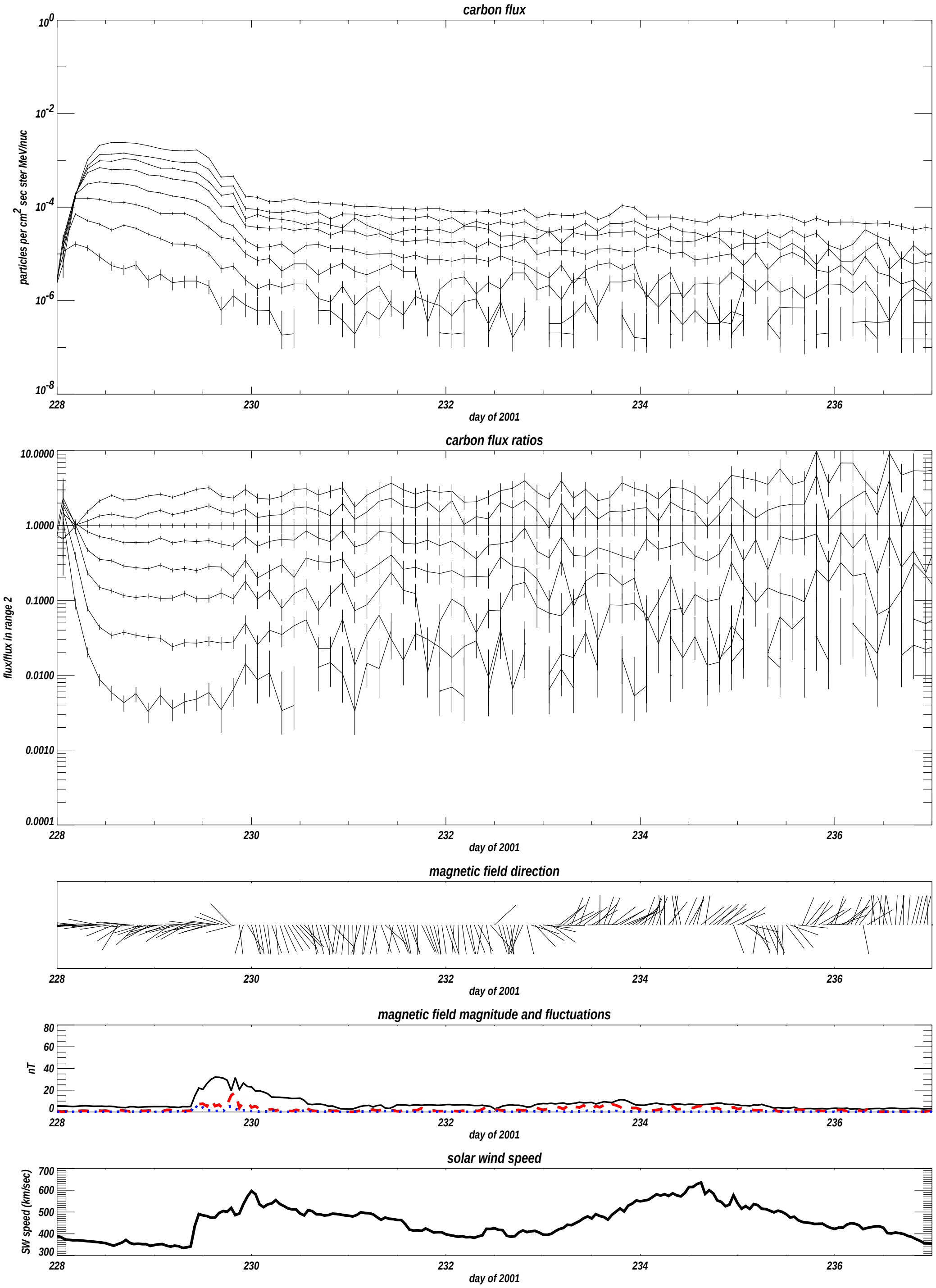

Figure A.5: Synopsis plot for the August 15, 2001 event.

ad astra per aspera